STAGGERED PATTERN ENERGY HARVESTING AND RETRO-DIRECTIVE BACKSCATTER COMMUNICATIONS FOR PASSIVE RFID TAGS AND SENSORS

A Thesis
Presented to
The Academic Faculty

by

Blake R. Marshall

In Partial Fulfillment
of the Requirements for the Degree
Doctor of Philosophy in the
School of Electrical and Computer Engineering

Georgia Institute of Technology
May 2018

STAGGERED PATTERN ENERGY HARVESTING AND RETRO-DIRECTIVE BACKSCATTER COMMUNICATIONS FOR PASSIVE RFID TAGS AND SENSORS

Approved by:

Professor Gregory D. Durgin,
Committee Chair
School of Electrical and Computer Engineering
Georgia Institute of Technology

Professor Manos M. Tentzeris
School of Electrical and Computer Engineering
Georgia Institute of Technology

Professor Andrew F. Peterson
School of Electrical and Computer Engineering
Georgia Institute of Technology

Dr. Shawn Rogers
Staff Antenna Engineer
Honeywell International Inc.

Professor Paul G. Steffes
School of Electrical and Computer Engineering
Georgia Institute of Technology

Professor Hoseon Lee
Assistant Professor of Electrical Engineering
Kennesaw State University

Date Approved: December 21, 2017

To my parents

who always supported my never-ending

but necessary

education

ACKNOWLEDGEMENTS

Firstly, I want to thank Greg Durgin for his countless hours spent advising and improving my work throughout my graduate career. Without his development of the Propagation Group at Georgia Tech, none of this work would be possible. Secondly, I want to thank every current and past member of the Propagation Group. Their constant technical and personal support is instrumental in where I am today. I really had fun taking courses and researching with all of you. Thirdly, I want to thank the committee and my professors for taking their invaluable time to review this work and to teach me throughout my academic career. Lastly, I want to thank my parents, the rest of my family, and my friends for their constant support of my choice to pursue higher education.

TABLE OF CONTENTS

SUMMARY

This work introduces an optimal backscatter and energy harvesting solution using N antennas with N ports for radio frequency identification (RFID) systems called a staggered pattern and retro-directive (SPAR) tag. By using multiple ports on the SPAR tag, the structure is able to passively steer its main beam by using multiple radiation patterns. From mathematical analysis, the optimal SPAR structure is required to have spatially orthogonal radiation patterns which are created by feeding an antenna array with a unitary scattering matrix such as a Butler matrix. SPAR tags are most effective by using higher frequency RFID systems where the antenna array uses the same amount of physical space as a lower frequency system.

In addition to theoretical analysis and simulation, a 2-by-2 SPAR tag at 5.8 GHz implemented with two patch antennas and a microstrip 90° hybrid is measured in an anechoic chamber to show retro-directive properties with various loading on each port to show orthogonality of the patterns. The same implementation is designed into a semi-active RFID tag to show backscatter retro-directivity and into a staggered pattern energy harvester. Both are shown to have improvements over the control tags with a single antenna at 5.8 GHz.

In addition to canonical designs, new SPAR structures are hypothesized with optimized size, bandwidth, etc. A co-simulator is developed capable of searching a vast space of possible feed networks with N ports that meet the requirements of a unitary scattering matrix. By using Matlab and Agilent ADS, structures can be analyzed for their scattering matrix properties and adjusted to meet the scattering, physical size, and bandwidth requirements. A new structure that meets the 2-by-2 SPAR scattering matrix requirements is presented to demonstrate the capabilities of

the software. The software can also be generalized to discover new physical structures of larger $N-by-N$ SPAR tags or other microwave devices such as circulators, power splitters, etc.

CHAPTER I

INTRODUCTION

The objectives of this chapter are:

- To introduce costs and benefits of using directive RFID tags at higher frequencies.
- To provide literature survey of various retro-directive devices and a history and future of improvements to RFID systems.

The objective of this research is to develop passive radio frequency identification (RFID) tag capable of harvesting radio frequency (RF) energy with a passively steerable beam to create a staggered pattern and retro-directively (SPAR) backscatter communications to a reader. The structure must be able to connect to a single multi-port radio frequency integrated circuit and maintain a reasonable size compared to low frequency tags. This work is the first to discuss SPAR tags and their benefits, implement a SPAR tag on a 5.8 GHz RFID system using a microstrip 90° hybrid and two patch antennas, show the theoretical analysis of using orthogonal radiation patterns for passive multi-port RFID tags using the Stein limit, and presents a new optimizer to find new SPAR structures.

Current RFID systems mainly use near field coupling (NFC) or ultra-high frequencies (UHF) for powering and communicating with RFID tags [16]. But, by using higher frequencies, smaller antenna sizes allow for more advanced RF techniques such as SPAR devices to be applied to RFID tags. With the same effective area of a 915 MHz isotropic radiator, a 5.8 GHz steerable reader and a passively steerable tag, can increase the ideal power-up range while maintaining larger bandwidth and wide effective beamwidth.

1.1 History of Passive Backscatter Technology

Backscatter technology was first used in the 1940s during World War II for aircraft identification in radar systems based on discoveries from Sir Robert Alexander Watson-Watt in 1935 [52]. Allied planes would roll when returning to base altering the reflected energy in order to reveal that they were friendly aircrafts. Later, this became "Identification, Friend or Foe" (IFF) which was able to identify friendly planes from enemy planes by interrogating a beacon on each aircraft [9]. The beacons did not radiate until they were interrogated at which point they would return a coded response. The coded response informed other allied aircrafts and ground radars that the aircraft was friendly and greatly reduced friendly fire throughout the rest of World War II. This was the earliest form of RF backscatter by using simple (mechanical) modulation but, at the time, some suggested the possibilities of using backscatter for communication of voice or other data [31] [59].

One of the first publications discussing backscatter technology was *Communication by Means of Reflected Power* written by Harry Stockman in 1948. Stockman discussed the plausibility of communicating wirelessly without using a transmitter by reflecting an incident wave [59]. Figure 1 shows a traditional communication system with a transmitter that sends data and a carrier signal for wireless propagation of the signal compared to the backscatter technique of modulating the data into an incident carrier wave. By using the incident carrier wave, the wireless communications range is reduced, but there is also a reduction in complexity by using a single oscillator and removing a transmitter [59]. Stockman summarizes the benefits of backscatter radio over traditional radio:

1. Frequency drift-free communications
2. Fading free communications by frequency shifting
3. Elimination of hardware such as a local oscillator

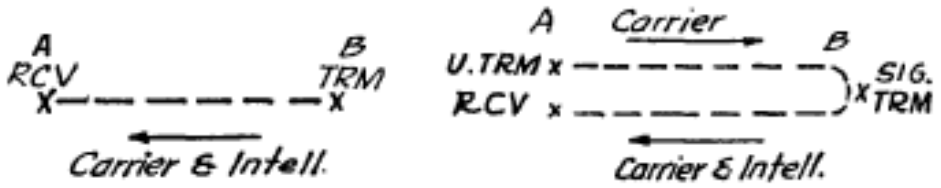

Figure 1: One of the first diagrams to suggest using backscatter for wireless communications from [59]

After interest in backscatter during the war, developments in the area slowed until the 1960s. In 1960, D. B. Harris patented a passive responder in a radio transmission system [27]. Harris' inspiration for the patent was to avoid replacing batteries in "Walkie Talkie" radio transmission [27]. The patent discussed multiple ways to backscatter data to a remotely located transmitter and a rectifier to harvest the energy from the wireless signal [27].

R. F. Harrington continued progress on backscatter communications in 1964 with his paper on loaded scatterers in which he developed the theory behind loaded antenna scattering [26]. Much of Harrington's theory allowed for Koelle, Depp, and Freyman to create an electronic identification system using RF backscatter in 1975 [29]. Other backscatter inventions were also devised during the 1960s such as Vogelman's system that used radar to backscatter information from the plane during radio silence [65].

By the late 1960s, many companies such as Knogo had initiated a backscatter system to eliminate theft called electronic article system (EAS) [31]. EAS simply used microwave or inductive readers to sense if a tag is present or not, effectively being a rudimentary RFID system. Since tags could be manufactured cheaply, this system spread quickly throughout retail stores as a method of theft prevention [31].

The 1970s was a time of rapid development for RFID over a variety of applications. In 1973, the first patent was awarded to Mario Cardullo for modern RFID

which included a rewritable active RFID tag that was "interrogated" and would "answerback" with data [52] [13]. Later in 1973, Charles Walton, often referred to as the father of RFID, received the patent for the first passive RFID tag [52]. Walton's patent outlined how to passively backscatter digital data which he licensed to many companies for developments in electronic locking systems [66]. The 1970s continued with Walton's patent paving a way into new applications such as animal tracking, toll collection, door security, vehicle tracking, and factory automation [31].

The 1980s and 1990s were focused on improving RFID technology and further shaping its current applications. For example, the size of RFID tags for a given size of memory had reduced by implementing circuitry on CMOS integrated circuits as shown in Figure 2 [31]. Modern day RFID tags such as Monza 5 made by Impinj have passive read sensitivities as low as -20 dBm with dipole antennas and 128 bits of memory over a die area of 0.2 μm^2 [1].

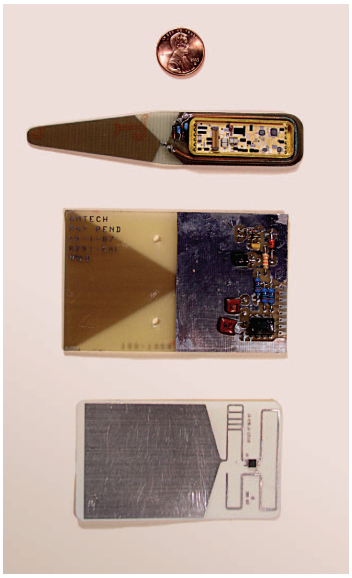

Figure 2: (a) 12 bit tag with circuitry over half of the tag - 1976 (b) 128 bit tag with custom CMOS IC over a quarter of the tag - 1987 (c) 1024 bit tag with custom CMOS IC over less than 1% of the tag -1999 Image and information from [31]

The history of passive backscatter devices has lasted over 50 years and continues to change. The capabilities and applications run the gamut from inventory management

and security access to animal tracking in remote areas [19]. The types of RFID tags and readers are equally as vast with various frequencies and protocols.

1.2 Long Range Passive Backscatter RFID

Modern day RFID systems have different readers, antennas, shapes, and sizes, but they can be broadly categorized by two properties: the frequency of operation and the tag's power supply [19]. The different types of power supplies are dissected into three varieties of RFID tags called active, semi-active, and passive. Active RFID tags use a battery and an on-board transmitter to communicate with a remotely located reader. Semi-active tags use a small battery to power a switch that reflects the incident waveform from the reader back with modulated data. Passive tags use the same backscatter communication technique as semi-active tags, but instead of a battery, they harvest the energy from the incident radio frequency wave [19]. Each of these power supply types can be used at any frequency, but the frequency selection determines the antenna size, path loss, and bandwidth [16].

1.2.1 Long Range RFID Frequencies

In the early 1980s and 1990s, the Federal Communications Commission (FCC) allocated three bands: 902-928 MHZ, 2.4-2.4835 GHz, and 5.725-5.875 GHz [22]. These are called the industrial, scientific, and medical (ISM) bands and allow for unlicensed transmission provided that the power levels remain under strict limits. These levels are defined by the maximum effective isotropic radiated power (EIRP) at 36 dBm (4 Watts) [22]. The rules set by the FCC prevent operators from overpowering the spectrum and blocking others from communicating over this shared radio resource.

Since these bands are open for communications, they are commonly used for long range RFID [50]. Each band has inherent trade-offs between bandwidth, range, and circuitry size that determines which frequency is best for a specific RFID application [16]. Table 1 depicts the differences between the frequency bands for passive RFID

Table 1: Summary of various frequencies for long range RFID showing the trade-off between range and antennas size assuming isotropic-to-isotropic line of sight link

Frequency	**915 MHz**	**2.45 MHz**	**5.8 GHz**
Bandwidth	26 MHz	83.5 MHz	150 MHz
Max Transmit Power	1 W	1 W	1 W
Max EIRP	4 W	4 W	4 W
-20 dBm Range	16.5 m	6.5 m	2.5 m
Antenna Size ($\lambda/2$)	0.164 m	0.063 m	0.026 m

applications.

The table shows 915 MHz has the farthest range for a given radiation power, but it also has the largest antenna and smallest bandwidth. At 5.8 GHz, the reverse is true; the bandwidth is wide and the antenna size is small, but the range is very limited. This comparison reveals a trade-off as frequency increases, the path loss increases, but the antenna footprint decreases. Higher frequencies also benefit from larger bandwidth which can increase bit rate for wireless communications [49]. This thesis focuses on antenna system designs at 5.8 GHz to mitigate the higher path loss and maintain the advantages of larger bandwidth and small antenna sizes.

1.2.2 System Diagram of RFID Backscatter

RFID systems have two main components: a reader and a tag (or multiple tags). The core of each component is shown as a block diagram in Figure 3. The reader has all high power electronics and produces a continuous wave (CW) transmitter by amplifying a local oscillator (LO) with a power amplifier (PA). The CW waveform propagates through the air and is reflected by the tag. After the waveform is backscattered by the tag, the reader receives the modulated wave and passes the signal through a low noise amplifier (LNA) to a demodulator (Demod) [16]. Then, the baseband signal is sampled by an analog-to-digital converter (ADC) such as the universal software radio peripheral (USRP) for a computer to extract the data.

Since 5.8 GHz RFID tags are not available off-the-shelf in IC form, microwave

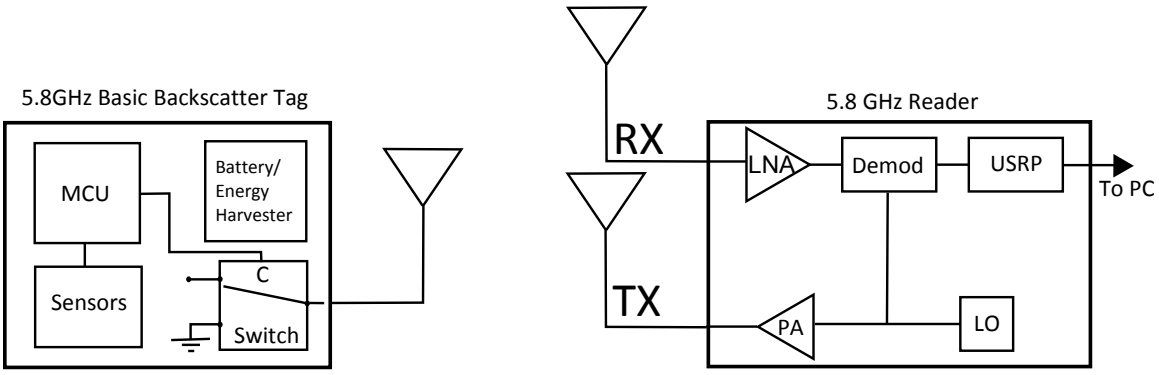

Figure 3: Backscatter block diagram showing the components of the tag and a bistatic reader

tags are custom made with discrete components. The tag is composed of an antenna, RF switch, a microcontroller, and an energy harvester or small battery. Some tags also include sensors to collect various information about the environment or the tag itself. If there are sensors, the microcontroller reads the sensors and has the switch alternate between two loads such as open and short to modulate the data with a 1 or -1 respectively as shown in Figure 4. The reflected wave is either the same as the incident or inverted which the reader deciphers as described earlier.

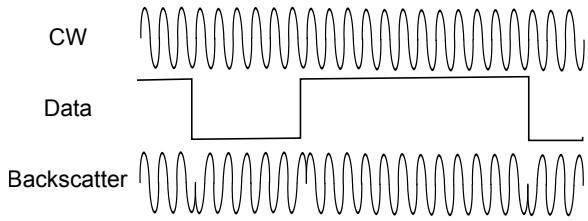

Figure 4: Time domain graphs of incident continuous wave (CW) signal from the reader and the backscattered signal from the tag

The block diagram shows that using backscatter radio focuses the cost and complexity on the reader side [19]. The tag is simple and very low cost so large quantities of tags can be produced easily and efficiently [19]. In addition, passive tags use energy harvesting circuitry instead of batteries to eliminate battery life limitations. RFID backscatter systems are governered by two link budgets called the backscatter link for communications and the power up link for passive tags to turn on.

1.2.3 Backscatter Link Budget

The backscatter link budget predicts the amount of power that is present back at the reader given the frequency, antennas, and modulation factor. Effectively, the backscatter link budget accounts for the limitation of the wireless communications between the reader and the tag. Similar to the Friis' equation, the backscatter link budget depends on power, gain, and path loss with a different order, because the signal must travel twice the distance for a given range of a transmit/receive system [23]. For a bistatic reader (similar to the one in Figure 3), the link budget equation is shown in (1) where P_R is received power at the reader, P_T is the transmitted power for the reader, G_T is the gain of the transmit antenna at the reader, G_R is the gain of the receive antenna at the reader, G_t is the gain of the tag antenna, λ is wavelength, r is the distance between the tag and reader, M is the modulation factor, and F_α is the fade margin [23].

$$P_R = \frac{P_T G_T G_R G_t^2 \lambda^4 M}{(4\pi r)^4 F_\alpha} \tag{1}$$

Since the backscatter link budget travels twice the distance of the one-way link budget, the power is spread to the fourth power of the distance. Given the reader's sensitivity, a minimum power requirement of a receiver, the range can be calculated for a given system. Although the backscatter link budget limits the range for semi-passive RFID, the power-up link budget limits the range of passive RFID tags.

1.2.4 Power-Up Link Budget

Passive RFID tags harvest energy from the reader's incident continuous wave signal by rectifying the RF signal via energy harvesting circuitry into direct current (DC) power. There are many topologies for energy harvesting circuitry with each composed of a combination of diodes and capacitors. The diodes limit current to flowing in a single direction while the capacitors act as low pass filters to smooth the output

voltage. Figure 5 shows the simplest RF-to-DC energy harvester that uses only one diode and one capacitor. The output capacitor holds a DC voltage with a slight ripple due to leftover RF on the node.

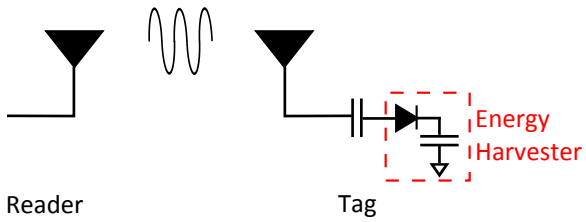

Figure 5: Simplest schematic of an energy harvesting system in RFID

The amount of power harvested by an RFID passive tag is characterized by the power-up link budget. The power-up link budget is shown for the line of sight case in (2) with the variables defined as: P_R is received power at the reader, P_T is the transmitted power for the reader, G_T is the gain of the transmit antenna at the reader, G_R is the gain of the receive antenna at the reader, G_t is the gain of the tag antenna, λ is wavelength, and r is the distance between the tag and reader [23].

$$P_{DC} = \eta_{EH}(1 - |\Gamma|^2)\frac{P_T G_T G_t \lambda^2}{(4\pi r)^2} \tag{2}$$

RF-to-DC conversion efficiency is given as η_{EH} and the reflection coefficient between the antenna impedance and energy harvesting impedance is given as Γ. Minimizing the reflections and maximizing the efficiency of the harvester is a difficult problem due to the inherent non-linearity of the diodes. The diodes cause reflections, a dependency between efficiency and input power, and generate harmonics of the incident frequency [10]. Although both the power-up link budget and the backscatter link budget are valid for passive RFID, for most cases, the power-up link budget is the equation that limits the range of a passive tag.

1.3 Problem Statement

Passive RFID tags are simple and inexpensive wireless communicators. Unfortunately, in order to replace a transmitter and batteries, tags must use backscatter radio and energy harvesting circuitry to power up and communicate which greatly reduce the range of RFID tags [59]. These range limitations can be shown through the link budgets for currently off-the-shelf RFID systems.

1.3.1 Link Budget Limitations

The power-up and backscatter link budget are shown in Figure 6 for a 5.8 GHz RFID system with the tag's gain of 0 dBi and a monostatic reader with a gain of 6 dBi. In addition, an off-the-shelf RFID reader's sensitivity is -70 dBm and an off-the-shelf RFID passive tag's sensitivity is -20 dBm are shown [1]. The intersection of the backscatter link budget and the reader's sensitivity represents the range limitation of the backscatter link budget with a semi-passive tag which occurs around 10 meters [1]. The intersection of the power-up link budget and the tag's power-up sensitivity represents the power-up link budget range limitation for passive tag at 3 meters.

If a 915 MHz system is used with the same antenna gains, the range dramatically improves due to the longer wavelength. This is not necessarily a fair comparison since the antenna sizes vary between 915 MHz and 5.8 GHz.

Since the antennas are different sizes, another comparison can be made by using the same effective area for each frequency instead of the equal tag gains. In (3), the effective area, A_{eff} of an antenna structure is approximated by the physical area, A_{phys}, and an efficiency term, e_a.

$$A_{eff} \approx e_a A_{phys} \tag{3}$$

The effective area is not only related to the physical area of the device but also to the gain, G, (4) in terms of wavelength, λ. If effective area is kept constant, as

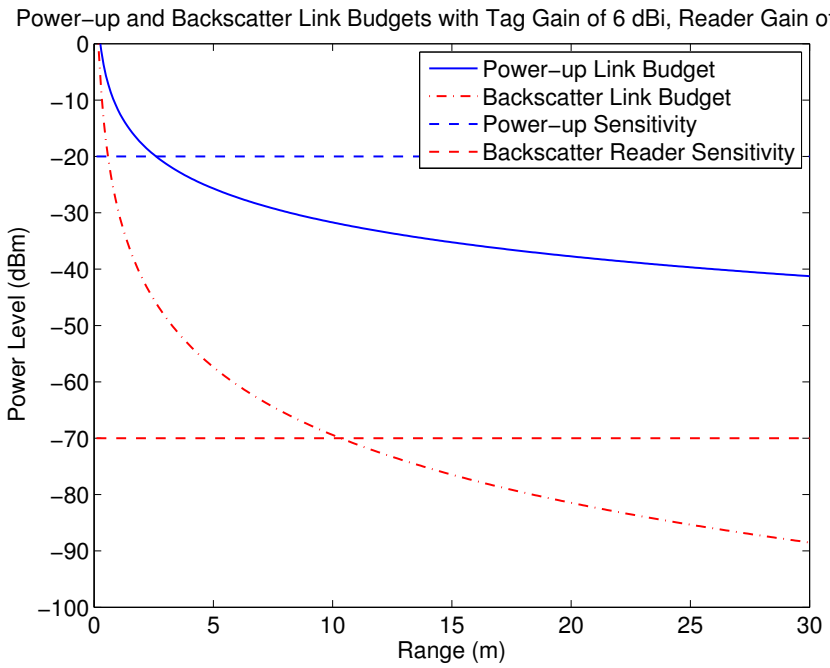

Figure 6: Power level over various ranges for the power-up and backscatter link budgets at 5.8 GHz with approximations of limiting ranges for both with a tag gain of 0 dBi and a reader gain of 6 dBi

frequency increases, the peak gain increases at a quadratic rate.

$$A_{eff} = \frac{G\lambda^2}{4\pi} \tag{4}$$

Replacing the gain of the tag in the power-up link budget with effective area of the tag, A_t, results in (5).

$$P_{DC} = \eta_{EH}(1 - |\Gamma|^2)\frac{P_T G_T A_t}{4\pi r^2} \tag{5}$$

The power-up link budget with effective area substituted for the tag's gain eliminates the dependence on frequency. Therefore, a given effective area every frequency has the same power-up range irrelevant of frequency, but at higher frequencies a passively steerable beam is required on the tag side. If the same substitution is made on the reader side as well, which means both the reader and the tag steer directional beams toward one another, the increase in frequency actually improves the received

DC power as shown in (6).

$$P_{DC} = \eta_{EH}(1 - |\Gamma|^2)\frac{P_T A_T A_t}{\lambda^2 r^2} \tag{6}$$

To graphically show these results, a 5.8 GHz 0 dBi tag, 915 MHz dBi tag, and a 5.8 GHz tag with the same effective area as the 915 MHz tag have been plotted versus range in Figure 7.

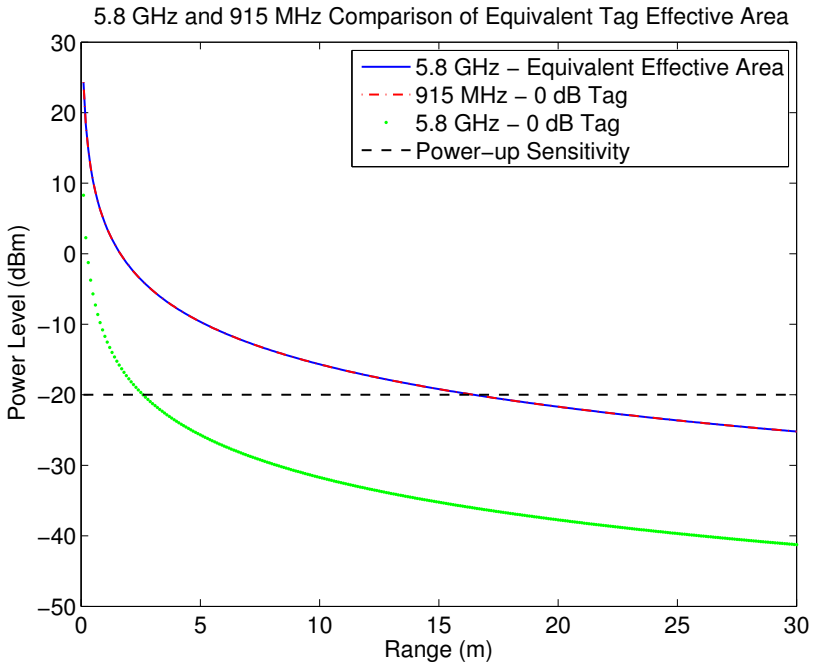

Figure 7: Power level over various ranges for the power-up link budget for 915 MHz and 5.8 GHz with a tag gain of 0 dBi and a reader gain of 6 dBi and 5.8 GHz using the equivalent effective area to 915 MHz with 0 dBi tag gain

The 5.8 GHz power-up range is dramatically less than the 915 MHz range when a single 0 dBi antenna is used for both systems. But, if the 5.8 GHz uses the same effective area as the 915 MHz 0 dBi (0.084 m^2) antenna and can passively steer the main beam, the power-up range is the exact same for both 915 MHz and 5.8 GHz increasing the 5.8 GHz range by over 600%.

1.4 Proposed Technique To Increase Range Limits

1.4.1 Factors to Increase Tag Range

There are many ways to improve the power-up range or the backscatter range individually but the following are the only parameters that improve both:

1. Increased transmitter power
2. Lower frequencies
3. Higher gain antennas

Firstly, increased transmitter power is not plausible in unlicensed bands due to FCC regulations as previously mentioned. Secondly, if a lower frequency is chosen, range can be increased but the benefits of larger bandwidth and smaller antennas are nullified. Thirdly, if high gain antennas are used, the beam of these antennas are narrowed which may disable or reduce operation at certain orientations [6]. These constraints indicate that the only potential for improvement is to use higher gain antennas, but the narrower beam and orientation dependence must be mitigated by passive beam steering.

The increase in gain of the antennas can be performed on two sides: the reader and the tag. The reader is powered by a large battery or power supply and can use a highly directive antenna with a very narrow beam that is actively steered towards the tag (pattern strobing) [17]. The directive array or antenna has a high gain that increases the range of both link budgets. This problem has been thoroughly investigated and many radar phased arrays have been used [18]. On the tag side, the antenna arrays must be steered without any initial power and all must be harvested.

1.4.2 Proposed Tag Antenna Requirements

The ideal tag antenna has a high gain without reducing the beamwidth which is not possible unless passive beam steering is used. Since the antenna has no power initially,

the beam steering must be capable of a *cold start*. With a cold start, the tag does not require any particular orientation to begin harvesting RF energy.

One method called *staggered pattern charge collecting (SPCC)* can be used to passively steer a beam by using multiple ports loaded with multiple RF-to-DC energy harvester. Staggered patterns take advantage of high gain arrays and negate the disadvantage of narrowed beamwidth by using multiple array patterns. For a 2-by-2 SPCC, there are two antennas in an array and two separate ports where one covers half-space and the other covers the other half-space.

In addition to harvesting, the tag must also communicate by backscattering the incident signal. To improve the backscatter range, the reflected signal should return in the same direction of the incident electromagnetic wave and called *retro-directivity*[17]. By returning the wave in the same direction, less energy is backscattered to angles not towards the reader. With more energy reflected back to the read with data, the signal-to-noise ratio at the reader is improved.

Finally, the simplicity and low cost of RFID tags cannot be lost when implementing a multi-beam structure. Therefore, it is imperative that the antenna device have a single point of connectivity and not require multiple chips for backscatter communications. In typical RFID and passive sensor design, the operations of RF energy harvesting and modulation are performed on a single radio frequency integrated circuit (RFIC) to limit costs. Thus, it is highly desirable to construct an antenna structure that performs staggered pattern energy harvesting and retro-directive modulation while maintaining a single point connectivity. All interfaces on the antenna structure must converge to a single region for a multi-port chip to be connected.

In summary, this thesis investigates developing a passive RFID tag for an RFID system by developing an antenna structure that has all of the following properties:

1. Cold power up

2. Retro-directive backscattering

3. Staggered pattern energy harvesting

4. Single point connectivity

1.5 Literature Survey

This literature review highlights techniques that could improve the range of passive RFID systems by increasing the power-up or backscatter link limitations. The review is divided into three sections: a superficial overview of non-tag antenna improvements, possible retro-directive devices for passive tags, and possible staggered pattern energy harvesters for passive tags.

1.5.1 RFID System Improvements

This section summarizes various improvements to passive RFID by optimizing the reader, signal, and energy harvesting circuitry.

Reader Pattern Strobing

For increasing range on the reader side, as previously discussed, pattern strobing uses a large reader array and steers the beam to the location of the tag. In order to obtain effective pattern strobing, large arrays use processing units to steer the beam accurately and follow the location of the tag. For example, Shinohara presents a 256 element array that implements a technique called position and angle correction (PAC) to steer a beam towards a RF-to-DC harvester [57]. A similar array implementing a four element Butler matrix has been adapted to RFID readers at 915 MHz to increase the range of the tags [35]. The steerable reader uses a high gain array to improve the power-up and backscatter link budget by focusing the main beam on the tag. In summary, there are phased array solutions to pattern strobe beams to improve power-up link budget limitations, but strobing requires intelligence and power which is not available on passive RFID tags.

Power Optimized Waveforms

Another technique to improve range of passive RFID is by changing the generated signal from continuous wave (CW) carrier to *power optimized waveforms* (POWs) or *multi-sine waveforms* (MSWs). POWs use multiple sub-carriers instead of a single carrier to increase the peak-to-average power ratio (PAPR) for increasing the efficiency of RF-to-DC conversion circuits. Trotter has shown that POWs increase range of off-the-shelf RFID tags due to their PAPR [60]. Similarly, Boaventura presents a paper of the energy harvesting improvement of radio frequency to direct current power conversion using MSW [7]. POWs have been shown increase the power-up link range, but there has not been publications on the effect of the backscatter link budget. Since a multiple sine waves are being used, modulation and demodulation is not trivial due to multiple copies of the reflected data on each sine wave.

RF-to-DC Circuitry Efficacy

In addition to POWs, many publications discuss increasing the efficiency of rectennas by improving matching between the antenna and energy harvesting circuitry. Nonlinearities in the diodes make the input impedance dependent on the input power, which makes matching at all power levels impossible. McSpadden shows a solution to this problem in [41] by matching transmission lines and improves the efficiency of rectification at 5.8 GHz to 83%, but the solution is limited to low power levels. Valenta summarizes energy harvester efficiencies with various frequencies from a multitude of previous papers [63]. The paper continues by showing how optimizing energy harvesting circuitry for POWs instead of CW can further improve the power-up range [63].

There are many other papers discussing similar techniques as summarized and shown in Figure 8 to improve RFID range, but this thesis focuses on how to create a tag with a retro-directive and staggered pattern antenna. The following sections

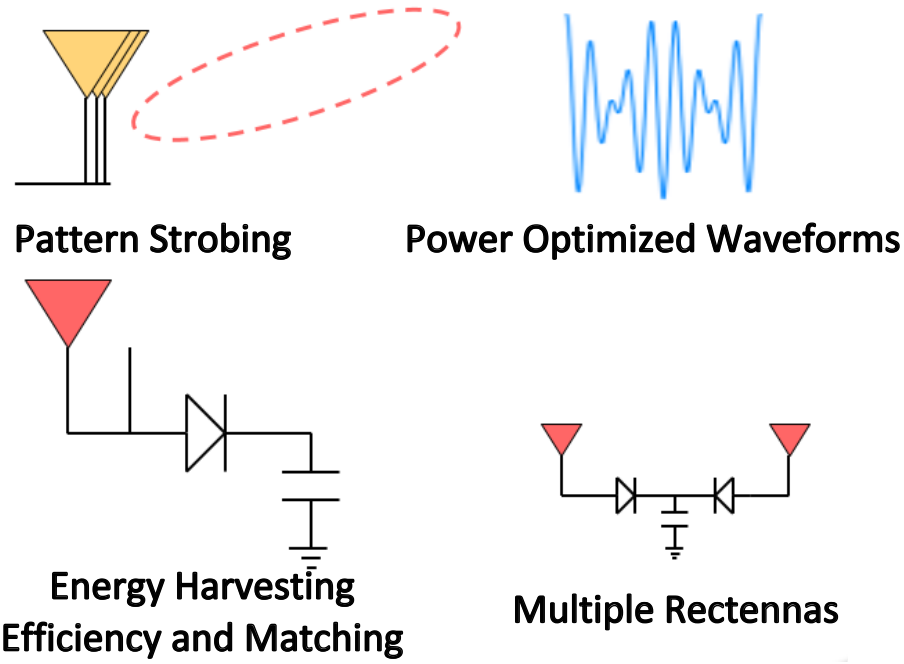

Figure 8: Passive RFID systems can be improve the power-up range through reader pattern strobing, power optimized waveforms, RF-to-DC efficiency and matching improvements, and multiple rectennas.

summarize possible retro-directive and staggered pattern structures in the literature that could be implemented on an RFID tag.

1.5.2 Retro-directivity Literature

Retro-directivity is defined as reflecting a wave in the direction of original incidence [20]. Unlike a traditional reflector where waves re-radiate at the opposite angle of incidence as shown in Figure 9, a retro-directive mirror re-radiates with the conjugate of the phase (negative phase). The conjugate phase causes the structure to re-radiate in the direction of incidence [20]. For a passive RFID, retro-directivity is useful for the backscatter link budget since it re-radiates energy only (ignoring side or grating lobes lobes) in the direction of the reader. Therefore, retro-directivity improves the backscatter link budget by increasing the gain of the tag in the reader's direction and improves the links ability to penetrate blockage in the wireless channel [30] [11].

There are a multitude of retro-directive devices but only a few would be able to

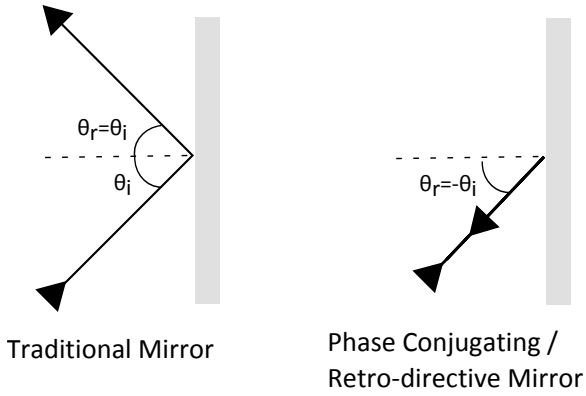

Figure 9: Reflection difference between traditional mirror and a phase conjugating mirror by ray tracing

be implemented on an RFID tag due to cost, complexity, power requirements, or size.

Corner Reflector

The earliest retro-directive device is the corner reflector which uses two orthogonal conductive sheets to reflect the incident wave back in the same direction as shown in Figure 10 [68]. The structure adds an additional reflection with the orthogonal conductive sheet to create phase conjugation. Although simple and easy to fabricate, the corner reflector is unable to modulate data into the incident wave easily making for difficult application to RFID [68].

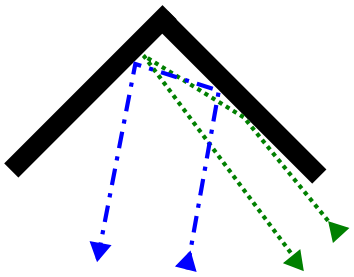

Figure 10: Corner reflector showing how incident waves from various angles results with reflections in the same direction

Van Atta Array

In 1958, Van Atta developed an electromagnetic reflector now called the *Van Atta array* which has the same properties as the corner reflector but makes modulation

of data simpler [64] [15]. Figure 11 shows how a four element Van Atta array works by creating the conjugate phase shift using transmisison lines [56]. d is the distance between the inner antennas and $d+n\lambda$ is the distance between the outer antennas. The incident wave induces phases on each element which are passed through transmission lines to invert the phases upon re-radiation.

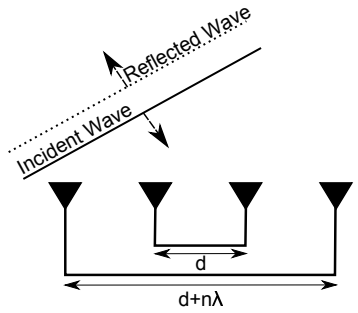

Figure 11: 4-element Van Atta array showing reflection in the same direction as incidence due to designed phase lengths between antennas

In literature, Buchanan and Fusco show that the retro-directivity of the Van Atta array dramatically reduced the bit error rates (BER) by orders of magnitude in wireless communications systems [11]. In addition to the linear array, Van Atta discusses the possibility of two dimensional retro-directive arrays [64]. Furthermore, Tseng, Chung, and Chang show that retro-directivity in both the E-plane and H-plane is possible with a simple microstrip design [62]. Finally, Koo applies the structure to RFID and shows that the Van Atta array can be implemented with backscatter modulation for binary phase shift keying (BPSK) and quadrature phase shift keying (QPSK) [30].

In summary, the Van Atta array can modulate an incident plane wave retro-directively [44]. Van Atta arrays use a limited amount of additional board space and do not require DC power or local oscillator making them an excellent choice for RFID tags.

Pon Array

The Pon array, shown in Figure 12, is similar to the Van Atta array but uses heterodyne mixing to create the proper phases for retro-directivity [68]. The incident wave form is given with an amplitude, A, frequency, ω, and phase, ϕ_k (7). By mixing the incident with a local oscillator with twice its frequency, the reflection results with two waveformss at the carrier frequency and triple the carrier frequency as shown in (8) and (9). The triple frequency term is filtered by the antenna resulting in a single waveform reflected from the array at the carrier frequency with a conjugate phase as shown in (10).

$$V_i = Acos(\omega t + \phi_k) \tag{7}$$

$$V_r = V_i V_{LO} = Acos(\omega t + \phi_k)cos(2\omega) \tag{8}$$

$$V_r = \frac{A}{2}[cos(\omega t - \phi_k) - cos(3\omega t + \phi_k)] \tag{9}$$

$$V_r = \frac{A}{2}cos(\omega t - \phi_k) \tag{10}$$

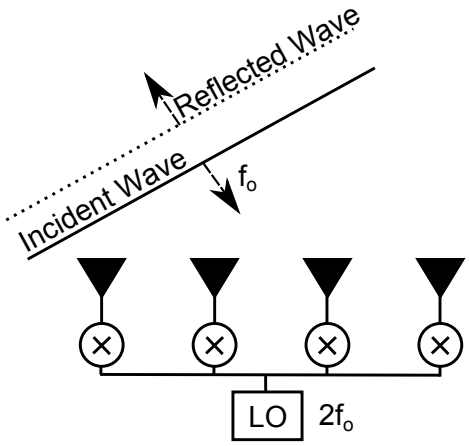

Figure 12: 4-element Pon Array with mixers for each element of the array and a local oscillator at twice the carrier frequency of the wireless communication channel

The Pon array has been used in many fields of study such as radar, space communications, and RFID. Fusco uses the Pon array to increase the radar cross section

(RCS) as a radar target [21]. Brown and Sinclair continue by using the Pon array for tracking in radar systems [10]. Miyamoto uses the Pon array to improve network security and increase communications efficiency for satellite communications [43]. In RFID, Zidek et al implements the Pon array on an RFID tag antenna to improve backscatter range [71].

Although the Pon array requires oscillators to be added to the array, the Pon array is not limited to planar orientations as with the Van Atta array [47] [43]. On the other hand, the Pon array does require mixers for each antenna element and a local oscillator (LO) twice the carrier frequency. Another issue occurs if the local oscillator frequency is not exactly twice the incident frequency because, the re-radiated frequency is shifted from the incident carrier frequency.

Rotman Lens

In 1963, Rotman and Turner wrote a paper about a wide angle microwave lens that is capable of creating M main beams from an array of N elements [54]. The paper outlined a design for a structure shown in Figure 13 that passively steers an array's main beam by using different feed points. The antenna array is shown on the right with for the $N = 4$ case and the feed points are on the left with $M = 6$. By feeding the lens from different ports, different phases occur on each antenna steering the main beam to 6 unique angles.

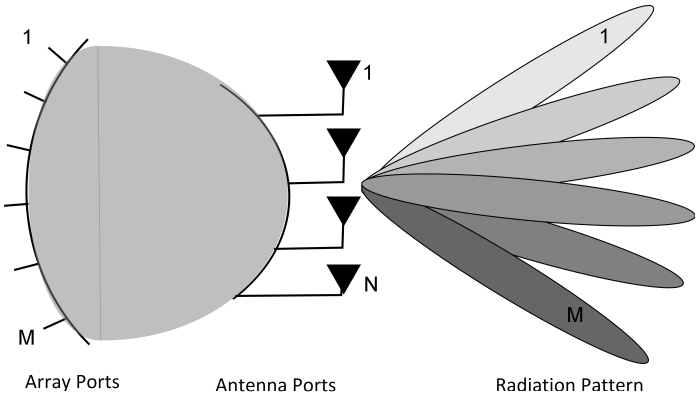

Figure 13: Rotman lens structure showing M=6 array ports and N=4 antenna ports

The Rotman lens has retro-directive properties as shown in multiple sources. Lee et al design and fabricate a Rotman lens without ports on the focal arc making them effectively open circuits and show measurements with retro-directivity between -12 degrees and +12 degrees [34]. Zhang et al develop theoretical models to predict the retro-directivity of Rotman lenses and simulate the results from -50 degrees to +50 degrees [69]. Christie et al use Vivaldi antennas to create a wideband retro-directive Rotman lens and compare actual measurements in an anechoic chamber to CST simulations [14]. Zhang et al use the retro-directive property of a Rotman lens for spatially secure QPSK modulation [70].

The Rotman lens has repeatedly been used for retro-directive applications and could be implemented on a passive RFID tag. Unfortunately, the design is complex and has a large footprint making it difficult to implement on a smaller form factor such as an RFID tag.

Butler Matrix

The Butler matrix is an S-parameter matrix that introduces phases from M ports to steer N antennas by using microwave circuits [12]. Butler and Rowe published the matrix in 1961 for simplifying designs in beam steering systems [12]. An example 4-by-4 microstrip Butler matrix is shown in Figure 14 with 5.8 GHz patch antennas. Butler matrices have been shown to have very wide scanning ranges from $-60\,\text{deg}$ to $60\,\text{deg}$ [24]. The scan angle enables a high gain beam to have wide coverage which is optimal for energy harvesting and retro-directive communications.

Butler matrices have been applied to RFID systems previously but as readers instead of tags [35]. For implementation on the tag side, Butler matrices must be reduced in physical size. Researchers have shown that it is possible to reduce the footprint of the Butler matrix by using artificial transmission lines and multiple layers [67] [8]. Like the Rotman lens, the Butler matrix also has passive beam steering

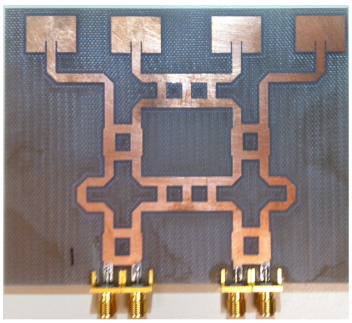

Figure 14: Fabricated 4-by-4 Butler matrix with 5.8 GHz patch antennas

that could be used for staggered pattern harvesting in addition to the retro-directive properties [72].

1.5.3 Staggered Pattern Charge Collection Literature

Staggered pattern charge collection uses multiple sub-arrays or switched beam antenna systems with multiple radiation patterns for improved RF-to-DC energy harvesting. The multiple main beams enables energy harvesting circuitry to be excited from a farther range over a wider area of coverage. In RFID, passive tags can use staggered pattern energy harvesting to improve the power-up range. An example staggered pattern switched beam structure with a four-element array with four excitation ports for energy harvesters is shown in Figure 15. Each port has a different radiation pattern as given by the various colors that provides a high gain antenna array in multiple direction for maximum energy harvesting. This section discusses different RF structures to phase the antennas properly for staggered pattern harvesting.

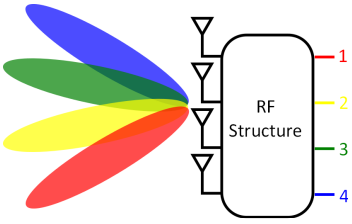

Figure 15: Generalized switched beam block diagram for four antennas and four excitation ports

Staggered Pattern Charge Collector

The staggered pattern charge collector (SPCC) is a set of N energy harvesting sub-arrays of N elements as shown in Figure 16. Each sub-array is aimed in a different direction to receive an incident wave with a high gain from various angles. By using multiple sub-arrays connected through energy harvesting circuitry to a common load, the gain can be increased without limiting beamwidth.

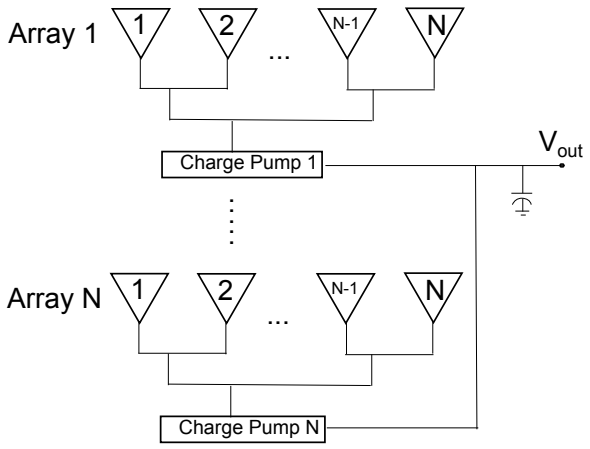

Figure 16: Staggered pattern charge collector schematic for N-by-N SPCC showing how each sub-array is only connected on a common DC capacitor adapted from [38]

The theory for N-by-N SPCCs uses classical array theory applied to each individual sub-array as developed in [38]. The author develops a metric for optimization of the SPCC by combining a traditional array trade-off between beamwidth and gain into a single quantity called integrated power conversion gain [38]. In addition, experimental verification was shown with a 2-by-2 SPCC to form two beams in the DC power pattern [39]. The 4-by-4 SPCC has been compared to a similar footprint of 16 rectennas and shown dramatic improvements in both beamwidth and peak gain [40]. The SPCC harvests better than 16 rectennas because energy harvesting circuitry has a minimum turn on power. With no arrays, the 16 rectennas cannot harvest any power at a far range in RFID systems.

Multiple Rectennas

Other researchers have experimented with using many rectennas in close proximity instead of using arrays to improve energy harvesting. For example, by using only 83% more area with three more rectennas, researchers were able to increase the DC power by 284% [42]. In another publication, Sakamoto implements two sub-arrays as a differential rectenna unit and connects multiple energy harvesters in various combinations of series and parallel [55]. The results show that given 0.03 W/m^2 incident on the rectenna array, the RF-to-DC efficiency was measured up to 38% were obtained [55]. These techniques are unlikely to improve RFID passive tag ranges since there is no increase in the voltage incident on the diodes. Without a sufficient voltage, the diodes are unable to turn-on and rectify the RF to DC power.

Staggered Pattern Properties of the Butler Matrix and Rotman Lens

The Butler matrix and Rotman lens were previously discussed in the retro-directivity section, but these two devices can also be used for staggered pattern energy harvesting. If energy harvesting circuitry is placed on each port, the structure becomes a staggered pattern charge collector. The lens uses a 1-by-N array instead of the N-by-N sub-arrays but effectively performs the same passive beam steering. These lenses and matrices could reduce the physical space required without reducing the effective area for each angle of incidence. No literature about loading a Rotman lens or Butler matrix with energy harvesting circuitry or other non-linear loads was found.

1.5.4 Summary of Possible RFID Tag Improvement Techniques

In summary, of the various devices discussed earlier, only the Rotman lens and Butler matrix have both properties of switched beams and retro-directivity as shown in Table 2. Both rely on multiple ports to achieve switched beams which must be modified to have a single point of connectivity for a single multi-port chip.

There have only been a few publications that have attempted to improve both

Table 2: Summary various techniques to improve power-up and backscatter link budget range

Technique	Single Connection	Staggered Pattern	Retro-Directive
Corner Reflector			✓
Van Atta Array	✓		✓
Pon Array	✓		✓
Large Array	✓		
Multi-Rectennas	✓		
SPCC	✓	✓	
Butler Matrix		✓	✓
Rotman Lens		✓	✓

the power-up link budget and the backscatter link budget. In one paper, the authors combined multiple techniques to create the ultimate RFID tag by using a Van Atta array for communications and an SPCC for energy harvesting [61]. The SPCC increased the power-up range and the Van Atta array increased the backscatter range. Unfortunately, this requires a larger footprint than a single integrated technique.

Others have attempted a Butler matrix to perform both switched beam and retro-directive communications but not for RFID applications [72]. The authors created a dual band Butler matrix using the lower band for switched beam operation of duplex communications and the upper band as a retro-directive array [72]. Neither band implemented communications but demonstrated the possibility of using one structure for both switched beam and retro-directive operation [72].

Unlike these other solutions, the proposed research uses a single structure to implement retro-directive backscatter communications and staggered pattern energy harvesting for passive RFID tags and sensors.

CHAPTER II

THEORY OF STAGGERED PATTERN AND RETRO-DIRECTIVE (SPAR) DEVICES

The objectives of this chapter are:

- To introduce staggered pattern and retro-directive (SPAR) RFID tags
- To show that larger effective areas of SPAR devices at multiple angles of incidence improve power-up and backscatter range, but larger effective areas result in larger physical size.
- To demonstrate that maximizing retro-directive backscatter and scattered pattern energy harvesting requires orthogonal radiation patterns from each port by using the Stein limit

A SPAR device is a structure that has a staggered and retro-directive radiation pattern by using multiple input ports to create multiple beams for energy harvesting or backscatter communications. SPAR devices can be composed of canonical designs such as a Butler matrices and Rotman lenses or they can be custom-designed for various form factors. SPAR devices achieve staggered pattern and retro-directive properties by having a large effective area in multiple directions of incidence. Upon initial investigation, this may seem impossible since the device is completely passive, but SPAR devices set up electrical currents differently from each input forming many radiation patterns peaking in different directions. SPAR arrays can be implemented in a passive backscatter device to dramatically increase the range.

2.1 Benefits of SPAR Tags on Backscatter and Power Up Link Budgets

During a typical query of an RFID tag, the RFID reader transmits an incident transverse electromagnetic (TEM) wave given in (11) and (12). The electric field is given in a direction orthogonal to the magnetic field with dependence on the magnitude of the electric field, E_o, impedance of the medium, η, frequency in radians per second, ω, time, t, k, wave number, and r, position vector.

$$\widetilde{E} = E_o e^{j(k \cdot r - \omega t)} \hat{\imath} \tag{11}$$

$$\widetilde{H} = \frac{E_o}{\eta} e^{j(k \cdot r - \omega t)} \hat{\jmath} \tag{12}$$

The time-averaged Poynting vector, $\langle S \rangle$, is the amount of power per area that is incident on an RFID tag from the reader's electromagnetic wave shown in (13). The total amount of power that can be harvested or reflected is computed by multiplying the effective area of the RFID tag at the given angle of incidence, $A_{eff}(\theta_i, \phi_i)$ by the time-average power density and is referenced by P_{inc} in (14). The generated DC power is the product of energy harvesting efficiency, η_{EH}, and transmission coefficient which is a function of the reflection coefficient, Γ, of the antenna with the energy harvesting circuitry shown in (15).

$$\langle S \rangle = \frac{1}{2} Re\{E \times H^*\} = \frac{E_o^2}{\eta} \hat{k} \tag{13}$$

$$P_{inc} = \frac{E_o^2}{\eta} A_{eff}(\theta_i, \phi_i) \tag{14}$$

$$P_{DC} = \eta_{EH} \left(1 - |\Gamma|^2\right) \frac{E_o^2}{\eta} A_{eff}(\theta_i, \phi_i) \tag{15}$$

The resulting equation for DC power shows a linear dependence on the effective area of the harvesting device from the wave's angle on incidence. If the effective area is increased for all θ_i and ϕ_i, the DC power harvested is higher and the range of a passive device or, in this case, RFID tag is increased. For the retro-directive backscatter link budget, the power density incident on the tag is not absorbed for DC power but reflected. The power incident excites the tag with an effective area of $A_{eff}(\theta_i, \phi_i)$ and is re-radiated at the same angle with the same effective area resulting in a square dependence on the tag's effective area.

By optimizing the effective area of SPAR tags over all angles of incidence, the DC power harvested can be maximized without knowledge of the reader's location. SPAR tags use multiple ports to phase an array of antennas to generate the orthogonal beams.

2.2 Phased Array Antennas

Phased arrays are a critical component to SPAR devices, but they have previously been used to improve communications signal-to-noise ratio in backscatter communications [72]. Most phased arrays are arranged in a planar structure in either one or two dimensions depending on the directions of scanning. Two dimensional arrays allow the beam to be aimed in both of the vertical and horizontal directions while a one dimensional array can only aim in the dimension that the antennas are spread. For both two and one-dimensional arrays, the beam forming occurs in the far-field region.

2.2.1 Far Field Assumption Limitations

As with any array or antenna, phased arrays have two regions of radiation: the near-field and the far-field. The near field contains high order decaying electric and magnetic fields that do not propagate through space efficiently. The far field is the region where the propagating wave exists and the near field as decayed sufficiently.

The minimum distance, R, where only the far field exists is approximately given in (16) where L is the array's largest dimension and λ is wavelength [25].

$$R = \frac{2L^2}{\lambda} \tag{16}$$

SPAR devices must operated farther than the far-field limit as given in (16) to ensure the proper patterns. Patterns are approximated by using array factors to transform current distributions into radiation patterns.

2.2.2 Array Factor and Radiation Pattern

In the far-field, one-dimensional arrays with identical antenna elements have radiation patterns that can be approximated by array factors. Radiation patterns are predicted by taking the product of the antenna's element factor, $f(\theta, \phi)$, by the array factor. (17) shows the radiation pattern of an array with antenna distributions on the x-axis, y-axis, or z-axis as given by (18a), (18b), and (18c). The axis of distribution determines the angle that the steerable beam spans. For example, if elements are spread over the z-axis, the main beam can be steered over the θ-axis while elements spread over the x or y-axis result in a beam angle in the ϕ direction. The array factor is a function of the amplitude on each antenna element, A_r, wave number, k, antenna separation, d, and phase shift, β_r. From the array's radiation pattern, the radiation intensity, U_m, in Watts per steradian is calculated based on by the impedance of air, Z_ω, 377 Ohms.

$$E(\theta, \phi) = f(\theta, \phi) \sum_{r=1}^{N} |A_r| e^{jr\angle A_r} e^{jr\omega_r} \tag{17}$$

$$\omega_r = kd \sin(\theta) \cos(\phi) \tag{18a}$$

$$\omega_r = kd \sin(\theta) sin(\phi) \tag{18b}$$

$$\omega_r = kd \cos(\theta) \tag{18c}$$

$$U_{\theta,\phi} = \frac{|E(\theta,\phi)|^2}{2Z_\omega} \tag{19}$$

An example of a one-dimensional, four element array is shown in Figure 17 with antennas distributed evenly along the y-axis. The example shows the coordinate system used with the ϕ-plane lying in the x-y plane and the θ-plane lying in the x-z plane. Since the 4-element array is linearly distributed over the y-axis, phasing of the elements cause the beam to the move in the ϕ direction [6].

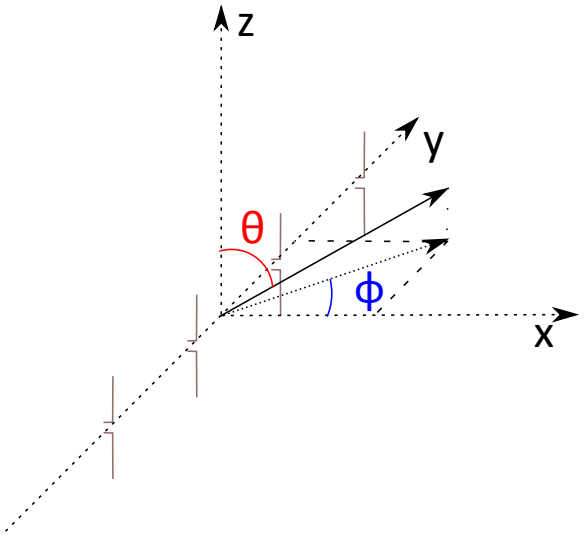

Figure 17: Coordinate system used throughout this thesis with an example 4-element array distributed on the y-axis enabling the beam to steer in the ϕ direction.

The array factor can be affected by element spacing, element phasing, and element amplitude. By assuming certain values for these properties, further simplifications and rules of thumb can be made.

2.2.3 Uniform Excitation of Arrays

Uniform excitation of linear planar arrays assumes that elements are identical, equally spaced, and have equal magnitudes of excitation. By using the assumption that each element has an identical radiation pattern, the array factor distributed along the y-axis can be written in the sine space. The sine space simplifies analysis of the

array factor making a substitution of u for $sin(\phi)$ and u_o for $sin(\phi_o)$ where ϕ_o is the direction of the main beam as shown in (20) .

$$AF(\theta, \phi) = \sum |A_r| e^{jrkdn(u-u_o)} \tag{20}$$

By using the sine space substitution, the array factor is shown to only be shifted by u_o given various phases of the elements. This result shows that the shape of the radiation pattern does not change with different phases on the elements. *With uniform excitation, a pattern is only shifted in sine space but the shape of the pattern is not altered by differently phased elements.*

Beamwidth

The beamwidth is critical to predict the overall coverage for a large phased array especially because as more elements are added the beamwidth shrinks proportionally. When an array uses three or more elements, the beamwidth is approximated within 5% by (21) [25].

$$\phi_{HPBW} \approx \frac{0.8858\lambda}{Nd\cos\phi_o} \tag{21}$$

(21) reveals that steering to small angles off broadside and keeping elements close together helps maintain a larger beamwidth. With the beamwidth is inversely proportional to the number of elements, are spaced In addition, the less elements used results in a wider the beamwidth, but the peak gain of the array decreases. For SPAR devices, a combination of high beamwidth and peak gain is the optimal configuration.

Sidelobes

Sidelobes occur with any uniformly excited array with nulls at $u = \frac{n}{N}$ and peaks at $N\tan\pi u = \tan N\pi u$. The side lobe ratio (SLR) is the ratio of peak to side lobe magnitudes of the pattern. If the array is more than 8 elements, the SLR

is approximately 13.26 dB and is not affected by the steered angle. With smaller arrays, the sidelobes reduce as $\frac{1}{\pi u}$ [25]. Sidelobes can be ignored for SPAR devices since they cannot be reduced for uniform excitation.

Grating Lobes

If spacings larger than $\lambda/2$ are used, grating lobes are created in the pattern. Grating lobes are extra main beams created by constructive interference at undesired angles, θ_{gl} as determined by (22) [25].

$$\frac{d}{\lambda} = \frac{n}{\sin\theta_o - \sin\theta_{gl}} \tag{22}$$

Since grating lobes are unwanted in SPAR devices, it is ideal to keep each element near ± 90 deg by varying the element separation if the steered angle cannot be changed. In factor, the limit to prevent grating lobes is given as (23).

$$\frac{d}{\lambda} \leq \frac{1}{1 + \sin\theta_{max}} \tag{23}$$

Keeping the element spacing below a half wavelength is critical to eliminate grating lobes. Without grating lobes, all the wireless power is directed to a single energy harvester versus allowing power to be split to multiple harvesters and dramatically reducing the efficiency of low-power rectennas. Grating lobes should be avoided for all optimal SPAR devices.

2.3 Switched Beam Structures

Switched beam structures are effectively feeding structures with multiple input ports for antenna arrays to phase the antenna arrays to a desired angle of radiation. For example, if one port is excited, the structure radiates in one direction and if a different port is excited, the structure radiates in a different direction. There are number of switched beam devices such as the Butler matrix, Rotman lens, Blatt matrix,

etc. [25]. These devices have traditionally been used in radar systems and wireless communication systems but have not been implemented for a passive RFID tag [2] [25] [33] .

2.3.1 Generic Switched Beam Setup

A generic switched beam structure is discussed as being M-by-N which means that there are M excitation ports and N antenna ports. A generic M-by-N switched beam structure is drawn in Figure 18 with each excitation port related to a radiation pattern by the color and labeled as the m^{th} port up to M. The blue pattern is produced by the M^{th} port while the red pattern is produced by the 1^{st} port.

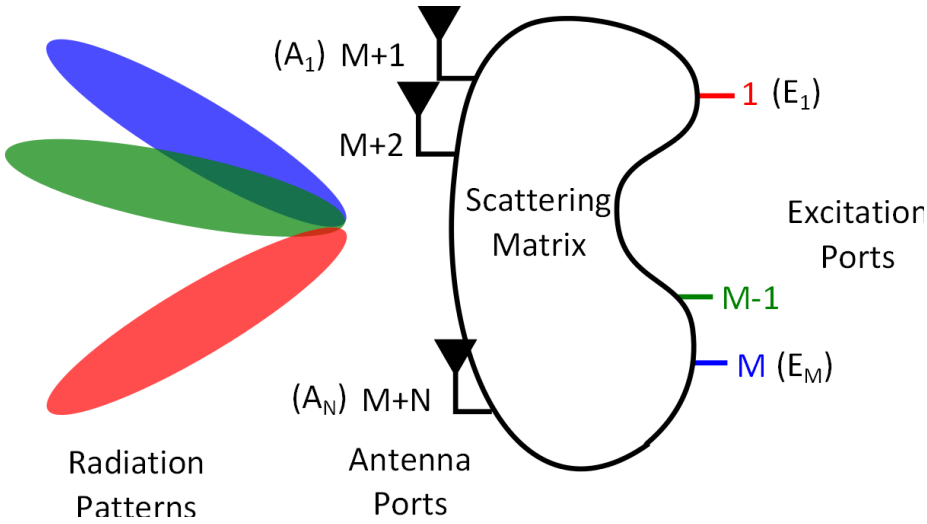

Figure 18: Generic multi-beam scattering structure showing the labeling of ports from 1 to M for excitation ports and M to $M+N$ for antenna ports as well as the alternate labeling using A for antennas and E for excitation when the forward-scattering or backward-scattering matrices are used

The antenna ports are labeled from $M+1$ up to $M+N$ to identify which amplitude and phases are received on which port to generate the array factor. There is also an alternative labeling when excitation ports have perfect isolation by using an E for excitation ports and an A for antenna ports. By using a scattering matrix. the relationship between the excitation ports and antenna ports is modeled to predict the radiation patterns.

2.3.2 Scattering Matrix Model

The S-parameter matrix models the relationship between the M input ports and the N antenna ports. Using the S-matrix, the amplitude and phase delivered to each port can be treated as a traditional scattering object with $M + N$ ports as shown in (24).

$$\begin{bmatrix} \tilde{P}_{1,o} \\ \tilde{P}_{2,o} \\ \vdots \\ \vdots \\ \vdots \\ \tilde{P}_{M+N,o} \end{bmatrix} = \begin{bmatrix} 0 & \dots & 0 & \tilde{S}_{1,M+1} & \dots & \tilde{S}_{1,M+N} \\ \vdots & \ddots & \vdots & \vdots & \ddots & \vdots \\ 0 & \dots & 0 & \tilde{S}_{M,M+1} & \dots & \tilde{S}_{M,M+N} \\ \tilde{S}_{M+1,1} & \dots & \tilde{S}_{M+1,M} & 0 & \dots & 0 \\ \vdots & \ddots & \vdots & \vdots & \ddots & \vdots \\ \tilde{S}_{M+N,1} & \dots & \tilde{S}_{M+N,M} & 0 & \dots & 0 \end{bmatrix} \begin{bmatrix} \tilde{P}_{1,i} \\ \tilde{P}_{2,i} \\ \vdots \\ \vdots \\ \vdots \\ \tilde{P}_{M+N,i} \end{bmatrix} \tag{24}$$

For the general structure, the excitation ports are defined as 1 through M and the antenna ports are defined as $M+1$ through $M+N$. If the lens is ideal, the excitation ports are completely isolated from each other resulting in $M + N$-by-$M + N$ square matrix of zeros in the top left. The same should be true for the antenna ports, so the bottom right contains a N-by-N matrix of zeros. If either of these are non-zero, there is not isolation between antenna-antenna or excitation-excitation ports.

The coupling from excitation to antenna ports matrix is given in the bottom left matrix beginning with $S_{M+1,1}$ and ending with $S_{M+N,M}$. The coupling from the antenna ports to the excitation ports or forward-scattering matrix is given in the top right matrix. The scattering matrix for SPAR devices have unique qualities to be optimal.

Reciprocal

For a reciprocal structure, the S-parameter matrix is equivalent to the transpose of the S-parameter matrix. The relationship is expressed mathematically in (25) [48].

$$S = S^T \tag{25}$$

Reciprocity is a requirement because SPAR tags are retro-directive. The link between retro-directivity and reciprocity is demonstrated by analyzing a wave incident on a SPAR tag using a switched beam structure. After the wave phases the elements of the array, the power is received and reflected off an excitation port which is re-radiates with conjugate phasing on the antenna array. Retro-directivity is defined as conjugate re-radiation as previously explained in Section 1.5.2.

Lossless and Passive

For a lossless structure, the S-parameter matrix must be unitary [48]. A unitary matrix must be a matrix with a set of ortho-normal basis vectors that span the space of $\mathbb{C}^N$ [32]. This property limits lossless switched beam structures to be N-by-N and states that the property in (26) is true [32].

$$\left[S^T\right]^{-1} S = I \tag{26}$$

Without the property of being lossless, the switched beam structure is inefficient because it would dissipate power. In addition to losslessness, no power is added to the system making it completely passive.

Uniform Excitation of Antenna Array

For uniform excitation of the antenna array, all elements in the forward-scatting matrix and the backward-scattering matrix must have magnitudes of $1/\sqrt{N}$. By selecting the magnitudes to be equal, the power is evenly divided to each antenna port. The lossless and passive conditions force the value to be exactly $1/\sqrt{N}$, but the phases of each element can vary.

2.3.3 Alternative Form for Scattering Matrix Model

Since (24) is, ideally, mostly zeros and the forward scattering matrix and the backward scattering matrices are transposes of each other, the equation can be expressed as a single M-by-N matrix by using the bottom left matrix. The antenna ports vector is replaced with A and the excitation port vector is replaced with E. Both are still complex vectors, but perfect isolation is assumed between each antenna and excitation port. If the amplitude and phase at the excitation port is desired from an incident electromagnetic wave, an inverse of the S-parameter matrix can be taken.

$$\begin{bmatrix} \tilde{A}_1 \\ \tilde{A}_2 \\ \vdots \\ \tilde{A}_N \end{bmatrix} = \begin{bmatrix} \tilde{S}_{M+1,1} & \tilde{S}_{M+1,2} & \dots & \tilde{S}_{M+1,M} \\ \tilde{S}_{M+2,1} & \tilde{S}_{M+2,2} & \dots & \tilde{S}_{M+2,M} \\ \vdots & \vdots & \vdots & \vdots \\ \tilde{S}_{M+N,1} & \tilde{S}_{M+N,2} & \dots & \tilde{S}_{M+N,M} \end{bmatrix} \begin{bmatrix} \tilde{E}_1 \\ \tilde{E}_2 \\ \vdots \\ \tilde{E}_M \end{bmatrix} \tag{27}$$

2.3.4 Single Port Excitation Gain Pattern

Combining the S-matrix model of beam formers with the phased array mathematics results in patterns for switched beam devices. By replacing the series form of the array factor by a vector form, as shown in (28), the S-parameter of the beam switching matrix can be combined into the gain pattern in (17). Let A be the antenna vector shown in (27) and $v(k)$ be the steering vector in (29) with k as the wave vector [6].

$$AF = A^T v\left(k\right) \tag{28}$$

$$v\left(k\right) = \begin{bmatrix} e^{-jk\cdot r_1} \\ e^{-jk\cdot r_2} \\ \vdots \\ e^{-jk\cdot r_N} \end{bmatrix} \tag{29}$$

By inputting the excitation vector, E, and the S-parameter matrix, S, into (28), (19), and (30), the gain, $G(\theta, \phi)$, is generated. If a single port is excited with the vector E of all zeros except a single one in the m^{th} element, the m^{th} gain pattern (G_m) is calculated. The gain pattern shows where energy is being radiated minus ohmic losses included in the efficiency term, η.

$$G_m(\theta, \phi) = \frac{\eta 4\pi \left| f(\theta, \phi) (SE)^T v(k) \right|^2}{\int_0^{2\pi} \int_0^{\pi} \left| f(\theta, \phi) (SE)^T v(k) \right|^2 \sin\theta d\theta d\phi} \tag{30}$$

In summary, given a single excitation from port m, the gain radiation pattern is given by G_m. Each port has a different gain pattern, but they share the same peak gain since each pattern uses N antennas with uniform excitation.

2.3.5 Multiple Beam Excitation

A major benefit of using beamforming structures is their ability to have two separate ports transmit simultaneously with two different radiation patterns. Multiple beam excitation is the superposition of multiple single beam excitations, and, ideally, has exactly the same two radiation patterns that they would during individual excitation. Although it may seem that each port can have any radiation pattern depending on the phasing structure, this is not the case as cross-coupling between excitation ports can cause a significant reduction in performance [58]. In order to have maximum efficiency for each pattern of the beam forming structure, the radiation patterns must be *orthogonal* spatially. If the patterns are not orthogonal, even a single port excitation could result in energy radiating in an unintended pattern.

Orthogonality of Patterns

Orthogonality of switched-beam structures is defined by only one radiation pattern being activated when a single feed line port is excited [25]. Therefore, if the m^{th} port is excited, only the m^{th} pattern has radiation. Mathematically, the definition of

orthogonality is shown in (31) while $i \neq j$ or, in other words, the inner product is zero [25].

$$\int E_i(\theta, \phi) E_j^*(\theta, \phi) d\Omega = 0 \tag{31}$$

Orthogonal patterns have nulls where the other patterns have peaks to minimize coupling between any two. This is demonstrated in Figure 19 where a 4-element Woodward-Lawson array has multiple beams plotted with phase progression of π/N.

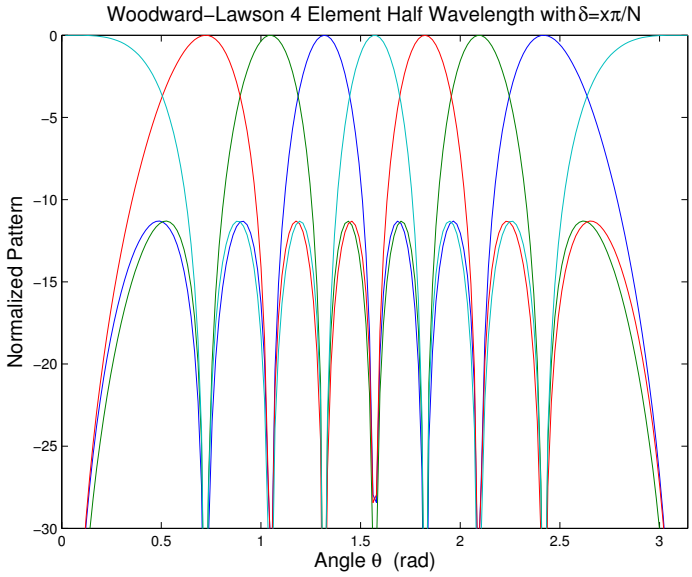

Figure 19: Multiple orthogonal patterns are shown where the adjacent patterns have nulls at the main lobe points and the crossover level is approximately 4 dB lower than the peak [25]

The nulls of the adjacent beams align with the peak of the main beam for each possible radiation pattern. Also, Woodward-Lawson beams have a *crossover level* of 4 dB for each pattern. The crossover level is the point when the adjacent main beam intersects with the primary main beam of excitation. For SPAR tags, a high crossover level is desired but without high cross-coupling between the patterns. The optimal performance of multiple excitation switched-beam structures is set by the Stein limit.

The Stein Limit

In 1962, Seymour Stein wrote a paper entitled *On Cross Coupling in Multiple-Beam Antennas* which related cross-coupling of feed ports with efficiency of radiation for switched beam structures [58]. In this paper, Stein showed the maximum possible efficiency of the structure is limited by cross-coupling [58]. Stein sets up the problem as shown in Figure 20 where x is the forward going wave into the feed ports and y is the reflected wave.

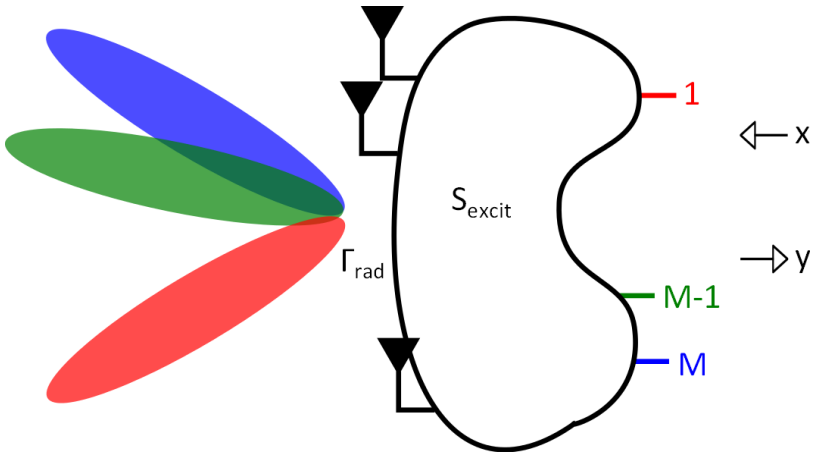

Figure 20: Stein's problem setup with S_{excit} as an M-by-M matrix for the excitation ports and the antenna ports loaded with radiators

To begin, a coupling coefficient (β_{lk}) is defined between the l^{th} and k^{th} patterns with a maximum of 1 if the beams completely overlap or 0 if the beams are orthogonal to each other. Stein's analysis continues by implementing conservation of energy to show that reflected power and radiated power must be less than incident power (32).

$$P_{tot} \geq P_{ref} + P_{rad} \tag{32}$$

By using the incident and reflected signals, conservation of energy can be written as follows in (33) with Γ_{rad} a function of the radiation efficiency of each pattern (q_k) and cross coupling (β_{lk}) with elements given in (34).

$$x^+x \geq x^+S_{excit}^+S_{excit}x + x^+\Gamma_{rad}x \tag{33}$$

$$\Gamma_{rad,lk} = q_l^*\beta_{lk}q_k \tag{34}$$

$$\beta_{lk} = \beta_{kl}^* \tag{35}$$

Γ_{rad} must be a Hermitian matrix because coupling between patterns must be complex conjugates of eachother as shown in (35). Since it is Hermitian, Γ_{rad} is a diagnolizable matrix. Let U be composed of ortho-normal complex eigenvectors of Γ_{rad} such that the diagnolization of Γ_{rad} results in a matrix containing the eigenvalues (γ) as shown in (36).

$$U^+\Gamma_{rad}U = \gamma \tag{36}$$

If U is used as a coordinate transformation from the original coordinates of x to an ortho-normal coordinate system, the conservation of power can be re-written in (37).

$$x^+U^+Ux \geq x^+U^+S_{excit}^+S_{excit}Ux + x^+U^+\Gamma_{rad}Ux \tag{37}$$

(37) can be simplified to (38) by substituting in γ and using the fact that U must be a unitary matrix.

$$x^+\{I-\gamma\}x \geq x^+U^+S_{excit}^+S_{excit}Ux \tag{38}$$

Since γ is a diagonal matrix and the right side of the equation is positive or zero, the equation can be simplified to (39) and (40).

$$\{I-\gamma\}_{lk} = \lambda_l^2\delta_{lk} \tag{39}$$

$$\lambda_l^2 = 1 - \gamma_l^2 \geq 0 \tag{40}$$

Therefore, each diagonal of γ must be less than or equal to 1, therefore the largest eigenvalue of Γ may not exceed 1. *In addition, there is a dependence between cross coupling between patterns, β_{lk}, and pattern efficiency, q_l^2.* For more details on this proof, examine Stein's original paper [58].

If equal efficiency for each beam is assumed, the efficiency is limited in (41) and called the Stein limit:

$$|q|^2 \leq \frac{1}{\{\beta_l\}_{max}} \tag{41}$$

Therefore, maximum efficiency of 1 is only possible if $\beta_{ll} = 1$ which means all off diagonals must be zero and there can be no cross-coupling between patterns. *For maximum efficiency of a uniformly excited array, each pattern must be mutually orthogonal to every other pattern.* This fact is even more critical to finding the optimal SPAR structure because the non-linear energy harvesting circuitry rectifies more efficiently at higher power levels.

Others have also contributed to orthogonal beam theory for multiple beam structures. Kahn and Kurss demonstrate that given uniform excitation and uniform phase progression the feed structure is unique [28]. Allen shows that for lossless, independent beams, the space factors for each pattern must be orthogonal [4]. Some experimental work of these results were published and supports that limiting cross-coupling is directly linked to orthogonal beams [5].

Ortho-normal S-matrix Columns

Since the radiation patterns must be orthogonal, the columns of the S-parameter matrix must be orthogonal as well. The switched beam matrix must also be lossless and passive, the columns of the matrix add to a magnitude of one. Therefore, each

column must be ortho-normal which follows the requirement of being a unity matrix. For any switched beam structure, the columns of the S-matrix have to be ortho-normal basis of $\mathbb{C}^N$.

2.3.6 Butler Matrix: An Orthogonal Beam Example

The Butler matrix is one of the first multiple beam structures to steer a beam passively by using different ports of excitation and to leverage Stein's orthogonality result for maximum efficiency. The Butler matrix is a commonly used switched-beam structure due to its simplicity of implementation; since it can be made with microstrip hybrid junctions and fixed phase delays for easy fabrication [25].

A Butler matrix connects 2^N array elements and 2^N excitation ports with a combination of hybrid junctions and fixed phase delays [12] as shown in Figure 21 for the 4-by-4 case. The Butler matrix is composed of three microwave components: 90 deg hybrid, crossover, and 45 deg phase shift [3]. $P1$ through $P4$ are excitation ports and $P5$ through $P9$ are antenna ports. For each excitation port, power is evenly distributed to all four antenna ports but no power is coupled to the other excitation ports. For example, if $P1$ is excited, the power is evenly distributed through to each port 6 through 9 with various phases resulting in a radiation pattern. In fact, each port will excite an orthogonal radiation pattern to any other port.

$$\begin{bmatrix} P6 \\ P7 \\ P8 \\ P9 \end{bmatrix} = \frac{1}{2} \begin{bmatrix} e^{-j\frac{\pi}{4}} & e^{-j\frac{3\pi}{4}} & e^{-j\frac{\pi}{2}} & e^{-j\pi} \\ e^{-j\frac{\pi}{2}} & 1 & e^{-j\frac{5\pi}{4}} & e^{-j\frac{3\pi}{4}} \\ e^{-j\frac{3\pi}{4}} & e^{-j\frac{5\pi}{4}} & 1 & e^{-j\frac{\pi}{2}} \\ e^{-j\pi} & e^{-j\frac{\pi}{2}} & e^{-j\frac{3\pi}{4}} & e^{-j\frac{\pi}{4}} \end{bmatrix} \begin{bmatrix} P1 \\ P2 \\ P3 \\ P4 \end{bmatrix} \tag{42}$$

This fact can be shown from the S-parameter matrix from the Butler matrix. Using the scattering matrix for each block, the Butler matrix can be calculated and is shown in (42). This linear transformation maps the excitation ports' magnitude and phases to the antenna ports' magnitudes and phases. If the inner product of

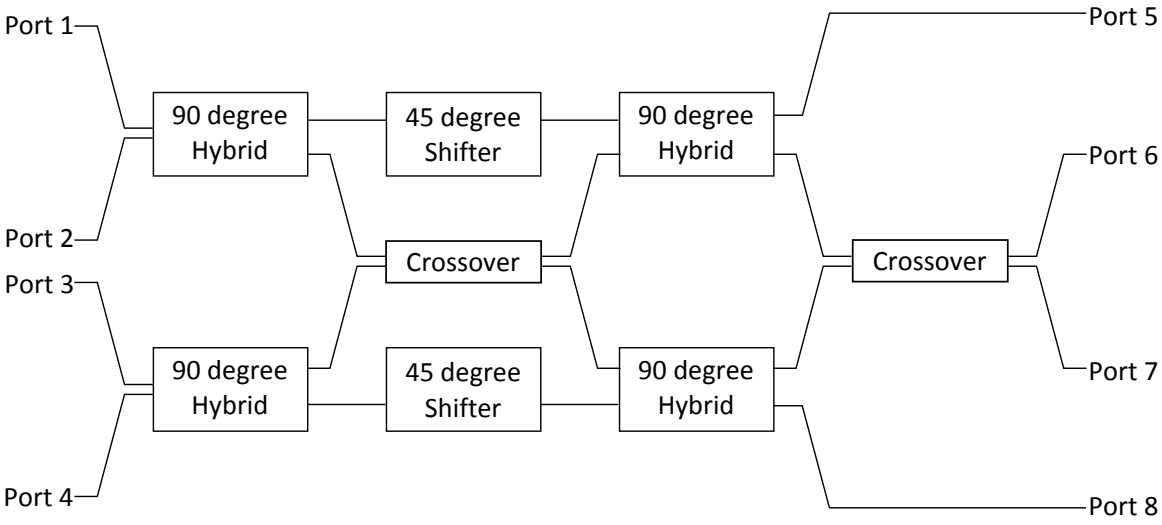

Figure 21: Block diagram of microwave devices used for a Butler matrix

each column is taken with each other, the result is always zero or in other words the matrix has orthogonal columns. In addition, each column has a magnitude of one making each a normal vector. Ortho-normal columns of a scattering matrix places the Butler matrix at the Stein limit for switched-beam efficiency.

2.4 Staggered Patterns with Switched Beam Structures

When using switched-beam structures such as the Butler matrix for receiving instead of transmitting, the same properties hold due to reciprocity. For receiving, the switched beam structure is excited with an incident wave entering the antenna ports propagating through to the excitation ports. By reciprocity, the S-parameter matrix is inverted to calculate the resulting magnitudes and phases. Given an incident wave, the antenna ports collect energy from the wave front with various phases, ϕ_n as shown in Figure 22. If the wave is incident on a main lobe peak, all of the power will propagate to a single port, but if the angle of incidence between two main beams, the power is split between two or more ports. Although the RF power may exist at multiple ports, only the port with the highest power level is of interest because RF-to-DC converters only work efficiently at high power levels. To approximate the

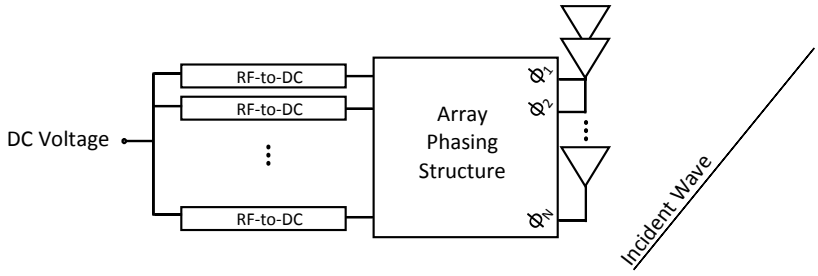

Figure 22: Staggered pattern energy harvesting lens with an incident wave creating various phases on the antenna ports that turn on energy harvesting circuits connected to each excitation port

amount of DC power for all the possible radiation patterns of the switched-beam structure, an upper and lower bound are defined for SPAR structures: summation gain and aggregate gain.

2.4.1 Aggregate Gain

The aggregate gain is defined as the maximum gain of all gain patterns for each angle of incidence as expressed in (43).

$$AG(\theta, \phi) = max[G_m(\theta_o, \phi_o)] \tag{43}$$

Effectively, the aggregate gain assumes only one port is harvesting energy at any given moment or angle of incidence. For the majority of angles of incidence, this is an accurate estimate of the gain of the structure and can be applied to a link budget and RF-to-DC model to estimate the DC power harvested.

2.4.2 Summation Gain

The summation gain is the upper bound for the gain pattern of a SPAR device. In this case, it is assumed that all the patterns of the device contribute to the DC voltage harvested. The summation gain is defined as the sum of all gain patterns as given in (44).

$$SG(\theta, \phi) = \sum_{i=1}^{M} G_i(\theta, \phi) \tag{44}$$

To compare with the aggregate gain, both are depicted in Figure 23. The aggregate gain is less than or equal to the summation gain for all angles on incidence, while the actual gain lies somewhere in between the two. The actual gain pattern for each port is shown by the four different colors for perspective relative to the aggregate and summation gain patterns.

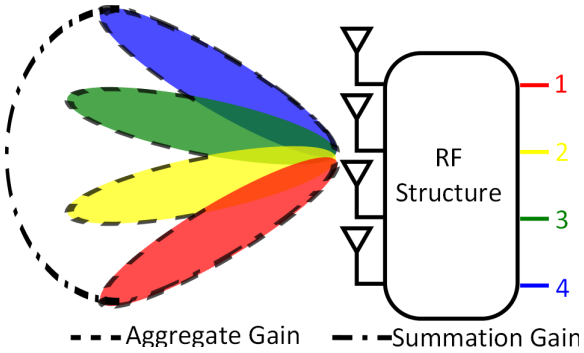

Figure 23: Approximated aggregate gain, worst case, and summation gain, best case, for a four port and four element lens

2.4.3 Energy Harvesting Circuitry

RF-to-DC energy harvesting circuits are composed of series diodes with shunt capacitors to create a one-way low pass filter. The diodes rectify by only allowing DC current to move towards the load, while the capacitors allow the RF signal to pump the DC voltage higher. In Figure 24, an N stage Dickson charge pump modified for RF-to-DC conversion is shown. When the RF input is negative, the vertical diodes are biased and DC current flows up through the vertical diodes building up charge on every other node. When the RF input is positive, the horizontal diodes are biased and DC charge is pumped towards the top right node to a DC output voltage.

The Dickson charge pump is composed on stages of diodes and capacitors where a stage is considered two series diodes and two capacitors. As more stages are added,

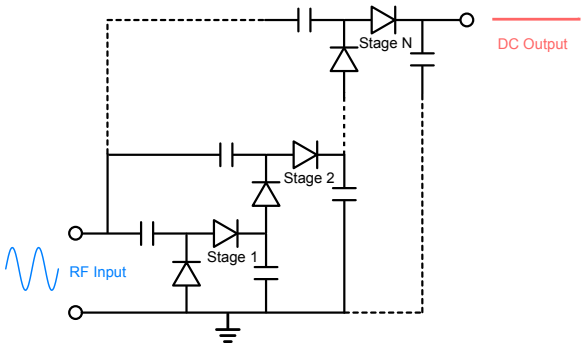

Figure 24: N stage Dickson charge pump schematic showing series diodes with shunt capacitors to isolate the RF input signal

efficiency decreases for low power levels [46] [37]. The diodes are necessary for rectification of the RF power, but they are very difficult to match due to their non-linear impedance especially at microwave frequencies.

Non-Linear Impedance

A non-linear device has an impedance that depends on input power in addition to frequency. This fact can be seen by analyzing the current-voltage (I-V) curve of a diode. Figure 25 shows the I-V curve of a typical Schottky diode with an arbitrary turn-on voltage and an arbitrary break-down voltage.

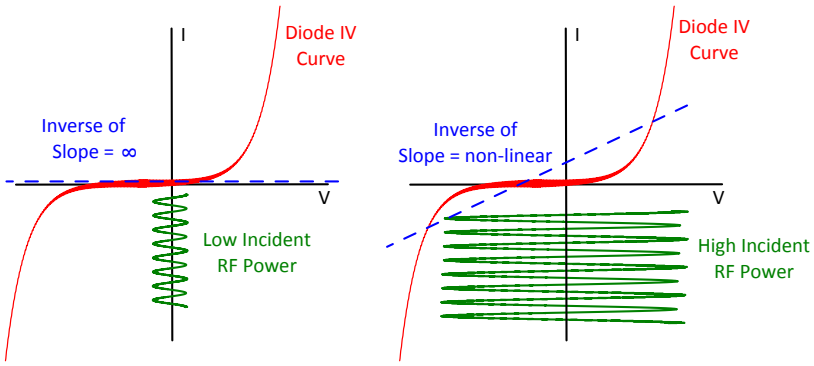

Figure 25: Diode impedance approximation for low RF input power and high RF input power to energy harvesting circuits

At low input power levels (on the left), the slope of a secant line is approximately flat which results in a very high impedance. As the input power increases (on the

right), the RF signal ranges over more of the I-V curve without a straight secant line. Due to this variable impedance with power level, it is very difficult to match RF signals to diodes. The non-linear impedance causes losses due to mismatch as well as harmonic generation from the RF signal fundamental [36].

Efficiency

In addition to impedance mismatch, RF-to-DC energy harvesting efficiency depends heavily on the input power and the diodes selection. In general, RF-to-DC circuits perform more efficiently at higher power levels primarily due to the turn-on voltage of the diodes [46]. In fact, if the power level drops below the turn-on voltage, there is nearly no RF power rectified to DC. As the input power increases, the efficiency increases until the breakdown voltage is exceeded. For passive RFID, this breakdown voltage effect is rarely observed since these devices harvest on the power level of 10s of micro-Watts.

2.4.4 SPAR Pattern Metric

The ideal SPAR tag should have a high gain in all direction to maximize the amount of energy harvested. The coverage of all the beams and the gain pattern of each port is integrated into a single metric called *average aggregate gain*. The average aggregate gain is calculated by summing over the aggregate gain pattern as shown in (45) and dividing by 4π steradians.

$$AG_{avg}(\theta,\phi) = \frac{\int_0^{2\pi}\int_0^{\pi} AG(\theta,\phi)\sin\theta d\theta d\phi}{4\pi} \tag{45}$$

The metric is effective because a single element or large array results in the same average aggregate gain of one as shown in Figure 26. But when a switched-beam structure is implemented, the result ranges from 1 to the ideal Stein limit. The Stein limit is optimal for staggered pattern energy harvesting and shows the orthogonal pattern structure lying on the limit.

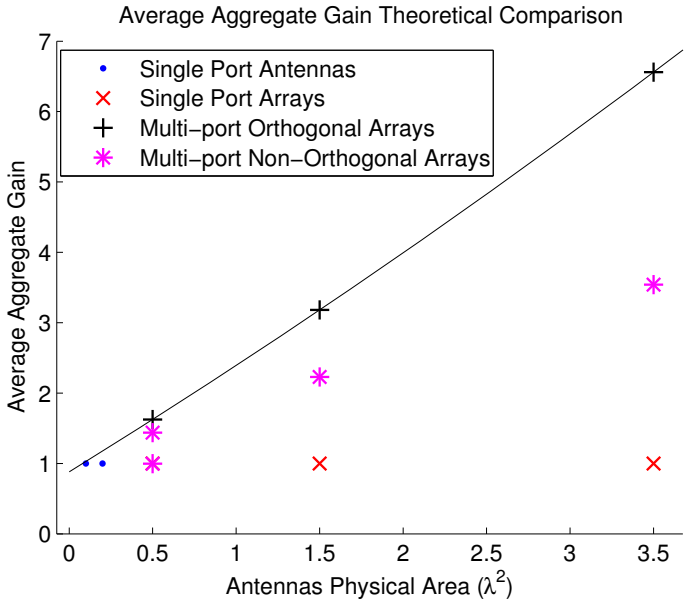

Figure 26: Average aggregate gain versus antenna physical area to demonstrate the benefits of using multiple ports of excitation which is optimal when the ports create orthogonal patterns as stated by the Stein limit

As more physical area is allotted for the antenna structure, the average aggregate gain is increased linearly for orthogonal multi-port structures such as the Butler matrix, but larger arrays with a single port remain at unity due to the narrowing beamwidth as shown by the red 'x'. The black '+' represent a 2-by-2, 4-by-4, and 8-by-8 Butler matrices while the blue '.' represent a dipole and a patch antenna. Finally, the pink '*' are non-orthogonal multi-beam structure that can range from 0 to the Stein limit in average aggregate gain. Therefore, orthogonal multi-beam structures maximize the average aggregate gain for a given physical area.

2.5 Retro-directive Backscatter from Switched Beam Structures

A similar analysis shows that an optimal retro-directive structures also uses orthogonal beams to only re-radiate the energy in the direction of incidence. The only difference is the reflection coefficient from the load is used instead of the transmission

coefficient and the gain patterns are squared due to the pattern affecting both incidence and reflection of the wave in (46) where θ_i and ϕ_i are the angles of incidence while the re-radiated angles are θ_r and ϕ_r.

$$P_R = \frac{P_T G_T G_R G_t(\theta_r, \phi_r, \theta_i, \phi_i)^2 \lambda^4 M}{(4\pi r)^4 F_\alpha} \tag{46}$$

For the optimal structure, the angles of incidence and angles are re-radiation should be identical. To force the angles of incidence and re-radiation to match, the patterns must be orthogonal otherwise energy is radiated in directions other than the angle of incidence [25]. Following the Stein argument, the scattering matrix must also be made of ortho-normal columns to preserve retro-directivity.

CHAPTER III

2-BY-2 SPAR STRUCTURE USING A 90° HYBRID

The objectives of this chapter are:

- To demonstrate how to design a 2-by-2 SPAR tag using a microstrip 90° hybrid.
- To show simulations of the staggered pattern energy harvesting and retro-directivity benefits of the SPAR tag.
- To display a retro-directivity measurement of a 2-by-2 SPAR tag in an anechoic chamber using a monostatic measurement technique

The 2-by-2 Butler matrix is the simplest SPAR tag composed of a 90° hybrid and two antennas. The hybrid has four ports: two ports for antennas and two ports for energy harvesting circuitry and RF switches for backscatter. Ideally, each excitation port delivers equal power to each antenna port with a 90^o phase shift between them as shown in Figure 27. The blue pattern is excited by Port 1 while the red pattern is excited by Port 2. The peak gain and pattern of each is identical but they are aimed on opposite sides of boresight. Since the excitation vectors are orthogonal and the scattering matrix has ortho-normal columns, the patterns are spatially orthogonal.

The benefits of spatially orthogonal patterns have been shown in the previous chapter, but how to create structures to generate orthogonal patterns has not been shown. This chapter introduces the most basic SPAR tag and shows its effects on the tag's radar cross section (RCS).

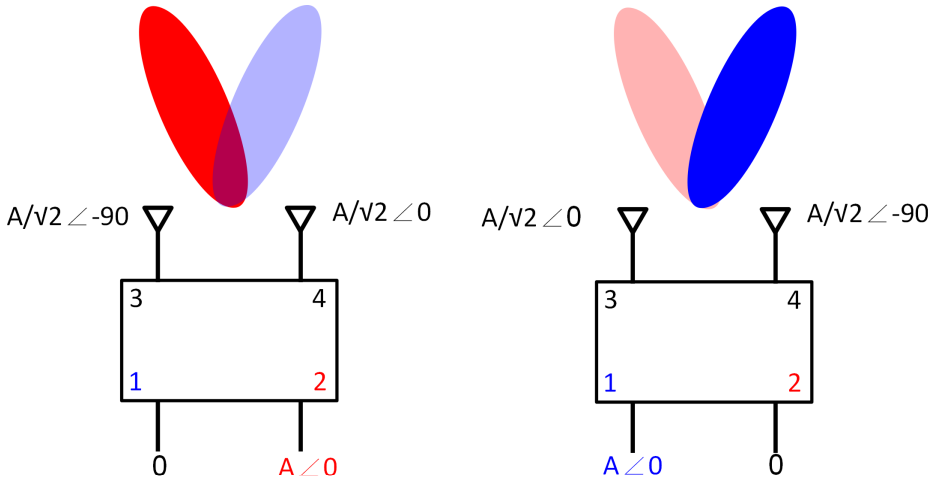

Figure 27: Hybrid block diagram when exciting Port 2 (left) and Port 1 (right) and how the phases of the antennas change as well as how the radiation pattern is altered

3.1 Design of 2-by-2 Butler Matrix

The 2-by-2 Butler matrix or a 90° hybrid has a straight-forward and simple design. The device uses transmission lines with quarter wavelengths to create the desired phase shift and power-splitting effects as shown in Figure 28 [48]. Since the hybrid is symmetric, even and odd mode analysis can be applied to calculate the S-parameter matrix as given in (47) [48].

$$S = \begin{bmatrix} 0 & 0 & \frac{-j}{\sqrt{2}} & \frac{-1}{\sqrt{2}} \\ 0 & 0 & \frac{-1}{\sqrt{2}} & \frac{-j}{\sqrt{2}} \\ \frac{-j}{\sqrt{2}} & \frac{-1}{\sqrt{2}} & 0 & 0 \\ \frac{-1}{\sqrt{2}} & \frac{-j}{\sqrt{2}} & 0 & 0 \end{bmatrix} \tag{47}$$

3.1.1 PCB Material Properties

The design was implemented on a FR-4 62 mil 2-layer board for low cost and ease of production. FR-4 is not the ideal material to implement radio frequency circuitry since it is lossy and tends to be less homogeneous than other substrates such as Rogers [53], but it was chosen since it is low cost and ease to production. Table 3

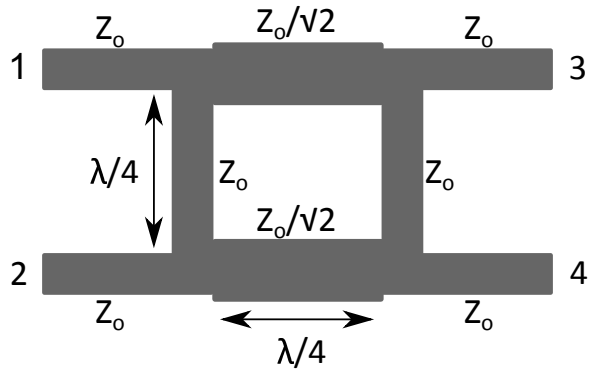

Figure 28: 90^o hybrid design using quarter wavelength microstrip transmission lines

Table 3: FR-4 2-layer printed circuit board characteristics

Characteristic	Value
Relative Permittivity (estimate at 5.8 GHz)	4.3
Loss Tangent (estimate at 5.8 GHz)	0.019
Thickness	62 mil
Copper Thickness	1 oz

shows substrate properties of the circuit board used to design the hybrid [45]. The microstrip lengths and widths are summarized in the Table 4. Using the traditional design for a hybrid at 5.8 GHz and the material properties shown above, the design was simulated to predict the performance.

3.1.2 Hybrid Simulation in ADS

The simulation was performed in Agilent Advanced Design System (ADS) 2013 with the FR-4 dielectric parameters as given earlier. The calculated geometries are used as an initial point for the optimizer then it finds the final geometry empirically. The goals used in the optimizer were to minimize return loss, split the power evenly between output ports, and produce a 90° phase shift between them. Th optimizer was able to change all copper dimensions (lengths and widths), but could not change the substrate constants.

The final optimized geometry and substrate characteristics are shown in Figure 29. All dimensions are shown in millimeters. The microstrip widths were optimized

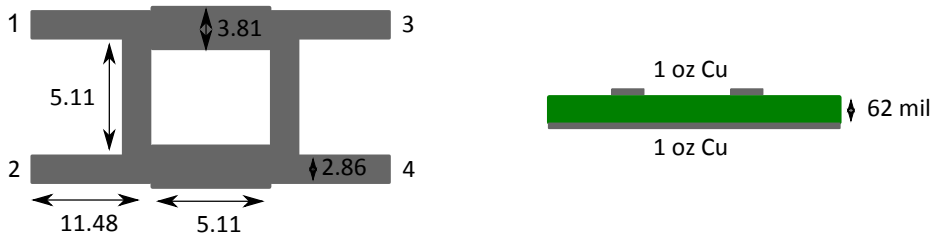

Figure 29: 5.8 GHz Optimized Geometry and FR-4 Board Geometry

Table 4: Geometry of 5.8 GHz Hybrid with effective permittivity and width to height ratio for microstrips

	Impedance	**Width (mm)**	$\lambda/4$ **(mm)**	ϵ_e	**Width-to-Height**
Z_o	50Ω	3.1	7.15	3.27	1.96
$\frac{Z_o}{\sqrt{2}}$	35.36Ω	5.24	7.00	3.42	3.33

to be thinner and quarter wavelengths reduced to 5.11 mm. The legs of each port were extended to 11.48 mm. The optimized structure resulted in the S-parameter matrix for 5.8 GHz shown in (48) as linear magnitudes and phase in degrees.

$$S = \begin{bmatrix} 0.08\angle 36.0 & 0.12\angle -27.2 & 0.67\angle -158.9 & 0.65\angle -70.3 \\ 0.12\angle -27.2 & 0.08\angle -36.0 & 0.65\angle -70.3 & 0.67\angle -158.9 \\ 0.67\angle -158.9 & 0.65\angle -70.3 & 0.08\angle -36.0 & 0.121\angle -27.2 \\ 0.65\angle -70.3 & 0.67\angle -158.9 & 0.12\angle -27.2 & 0.08\angle -36.0 \end{bmatrix} \tag{48}$$

The resulting S-parameter matrix is reciprocal as predicted by theory, but it is *not* lossless since the sum of $|S_{x1}|^2$ does not add up to one. In fact, it adds to 0.89 which means that 11% of incident energy is lost due to dielectric losses, conductor losses, and skin effect through the structure. $|S_{21}|$ should be zero for perfect isolation but actually collects about 1% of incident energy at the isolation port. Each antenna port receives approximately 43% of energy from the incident port with a phase difference between the ports of 88.6^o.

3.1.3 5.8 GHz Hybrid on 2-Layer FR-4 Hardware and Measurement

The finalized design was fabricated by a mechanical etching process from a 2-sided FR-4 circuit board. The resulting hybrid is shown in Figure 30 compared to a U.S. quarter with SMA side launch connectors added to connect a VNA and antennas.

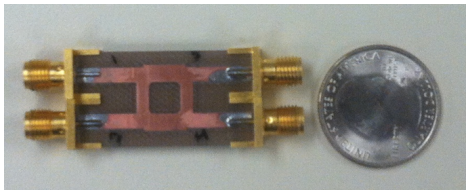

Figure 30: 90° hybrid at 5.8 GHz hardware with Port 1 (top left), Port 2 (bottom left), Port 3 (top right), and Port 4 (bottom right) connected to SMA connectors

To verify the simulation, the hybrid is connected to a 4-port vector network analyzer (VNA). Raw data from 2 to 10 GHz was measured for all ports and the complex values (dB, degrees) for 5.8 GHz are summarized in (49).

$$S = \begin{bmatrix} -21.09\angle -156.2 & -15.49\angle 168.2 & -5.05\angle 139.0 & -3.80\angle 44.1 \\ -15.41\angle 168.2 & -16.57\angle -163.0 & -3.82\angle 48.7 & -5.17\angle 137.6 \\ -5.06\angle 139.0 & -3.83\angle 48.8 & -19.46\angle 174.6 & -15.09\angle 162.1 \\ -3.80\angle 44.3 & -5.16\angle 137.6 & -15.08\angle 162.0 & -19.87\angle -158.9 \end{bmatrix} \quad (49)$$

Reciprocity is maintained throughout the measured values although the values deviate from simulation. All the ports with designed phases are shifted by about 20 degrees consistently resulting in a similar phase differences with the largest error from 90 degrees at 3% deviation. Of the total energy into Port 1, about 76% is accounted for at other ports. Only 4% of the accounted energy is reflected back into Port 1 or couples into the isolation port (Port 2) while the rest is split between the antenna ports. The split, however, is uneven with 42% and 31% of incident energy collecting at the same side port (Port 3) and opposite side port (Port 4) respectively.

The complete data measured on the VNA is displayed in Figures 31 and 32 from

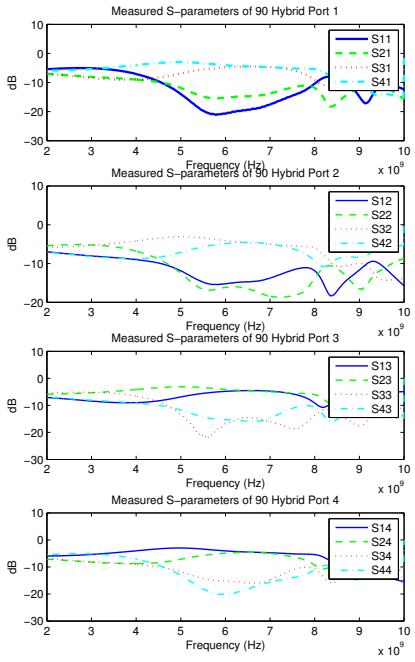

Figure 31: Measured Magnitude of S-parameters over frequency of 5.8 GHz 90^o hybrid

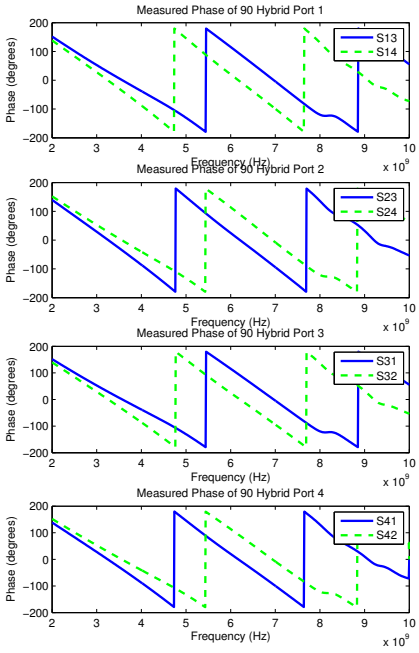

Figure 32: Measured Phase of S-parameters over frequency of 5.8 GHz 90^o hybrid

2 to 10 GHz. The return loss and isolation remains under -10 dB for all input ports while the coupled ports are from -6 to -3 dB around 5.8 GHz. In this band, the phase difference between coupled ports is approximately 90 degrees apart without much variation. The phases not shown are not significant due to the low values of the magnitudes.

By using a 90° hybrid connected to two antennas, a 2-by-2 SPAR tag is formed. The benefits of the SPAR tag are shown through simulation in terms of staggered pattern energy harvesting and a retro-directive radar cross section (RCS).

3.2 Staggered Pattern Simulation with 90° *Hybrid*

To simulate a SPAR during energy harvesting, the two antenna ports are excited with varying phase difference between them to emulate an incoming wave from various angles of incidence. When the phase difference is 0 deg, the wave is incoming at the

broadside of the antenna array. At a phase difference of $\pm 180°$, the wave either end of the array.

Three setups are compared: dual rectennas, staggered pattern 2-by-2 Butler matrix, and two element static array. Each schematic is shown in Figure 33 with rectifier circuitry attached to the receiving ports. The voltage across the load resistor is graphed as the antenna ports phase difference is varied. In addition, the power levels incident are varied from -10 dBm, 0 dBm, and 10 dBm.

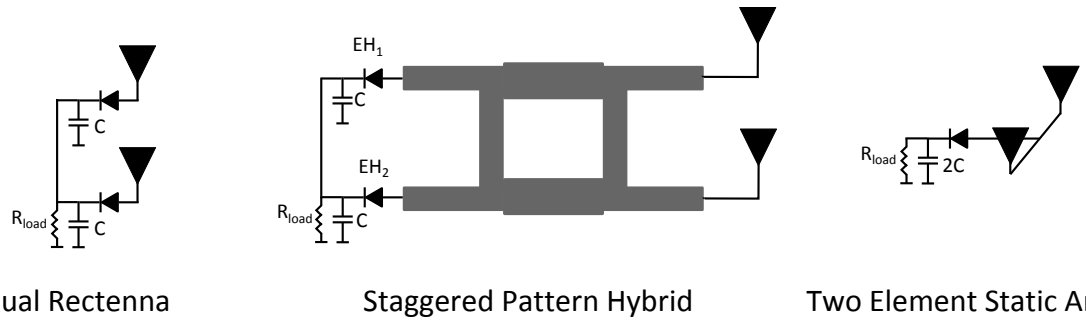

Figure 33: Simulation setups for staggered pattern energy harvesting: a single rectenna, a staggered pattern using hybrid, and a two element static array

Figure 34 shows each setup's efficiency. At the lowest power level, the dual rectennas are unable to build any significant charge due to the voltage not crossing the diode's thresholds significantly. The 2-element static array performs the best at 0 deg since the waves add coherently and excite the rectifier with the higher voltage. The staggered pattern hybrid circuit has two peaks at -90 deg and 90 deg. At these points, one of the rectifier ports has constructive interference resulting in higher efficiency of rectification.

The resulting patterns show that the staggered pattern hybrid clearly improves on dual rectennas at low power levels, but also covers more beamwidth than the 2-element array. Although the 2-element array performs better at its peak, it quickly decays and cannot harvest from other angles of incidence.

As the power levels increase, the peaks of both the hybrid and the static array widen and increase the efficiency by orders of magnitude. The large increase in

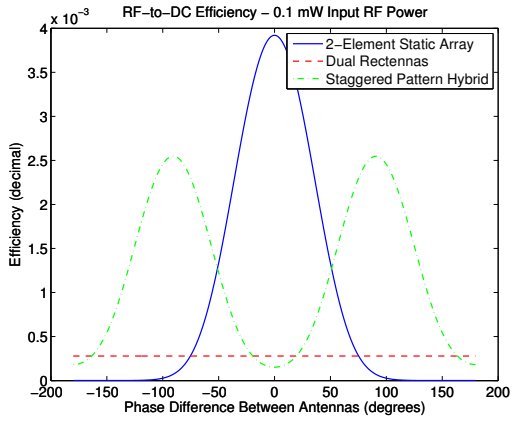

Figure 34: Simulation efficiency results for dual rectennas, staggered pattern hybrid, and two element static array at 0.1 mW input power showing the benefits of staggered pattern hybrids

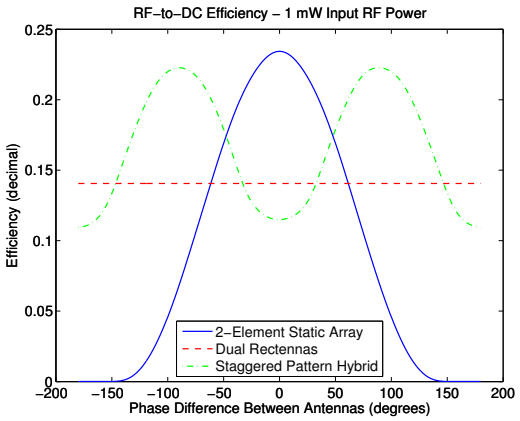

Figure 35: Simulation efficiency results for dual rectennas, staggered pattern hybrid, and two element static array at 1 mW input power showing the benefits of staggered pattern hybrids

magnitude is an inherent property of the rectifier and not caused by the different antenna techniques. The dual rectifier is able to turn on its diodes at 1 mW and converts RF-to-DC power at 15% efficiency. The static array and staggered pattern still outperform the dual rectennas at peak conditions due to coherent interference of the arrays.

At 0 dBm, the staggered pattern wider coverage is an enviable property when compared to the static array. The static array peak drops off quickly while only performing better than a rectenna over 120° while the staggered pattern array performs

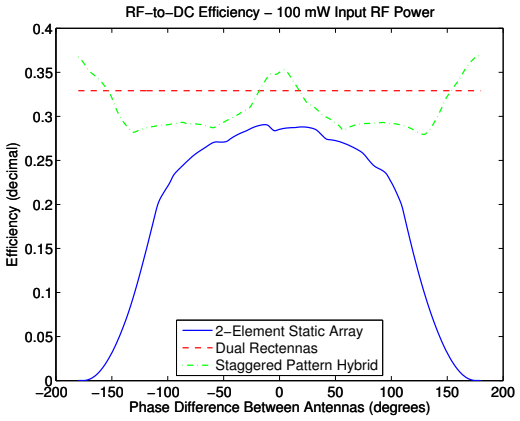

Figure 36: Simulation efficiency results for dual rectennas, staggered pattern hybrid, and two element static array at 100 mW input power showing that at high power levels, staggered pattern does not provide much benefits

better than the dual rectennas over 240°. The peak difference between the static array and staggered pattern array decrease as breakdown voltage of diode begins to affect the output voltage.

This effect is exaggerated by a higher power level at 20 dBm. When there is sufficient power to activate the dual rectennas, arrays become a detriment to efficiency. The higher gain drives the diodes non-linearly and break down effects can harm the patterns. The patterns are shown in Figure 36 with non-linear effects causing strange variation in the patterns.

3.3 Retro-directivity Simulation with 90° *Hybrid*

A similar simulation can be made in Agilent ADS to show retro-directivity of the hybrid device. In this case, the hybrid is connected to four different loads: rectifiers, opens, shorts, and matched loads while the antennas ports are connected to a circulator to measure reflected power as shown in Figure 37. Similarly to the SPCC simulation, the phase difference between the antennas is varied and the power level is set to -20 dBm.

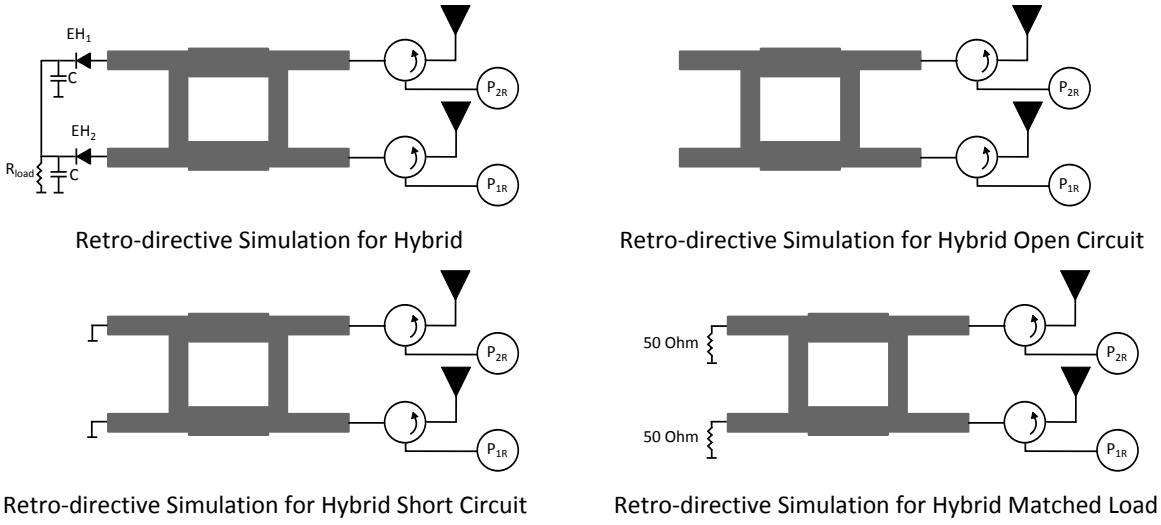

Figure 37: Diagrams of the simulation for retro-directivity using an ideal circulator with various loads including: energy harvesting circuitry, open circuit, short circuit, and matched load

For retro-directivity, the antennas should re-radiate with the opposite phase difference between the antennas of the incident wave. Figure 38 shows the re-radiated phase difference of the antennas versus the incident phase difference. For short and open loads, the re-radiated phase difference is approximately the opposite of the incident phase difference resulting in a retro-directive property.

The matched loads do not exhibit this property, because the power is absorbed instead of re-radiated. This is shown in Figure 39 with power levels 20 dB lower than incident. The short and open re-radiate the same incident magnitude of -20 dBm with dielectric and conductor losses. There is slight variation in the peaks of each port based on the staggered pattern phasing structure. Each port peaks at ± 90 deg by about 1 dB.

When the 2-by-2 Butler matrix is loaded with rectifiers, it behaves as a open at low power levels because of the inherent current-voltage curve of a diode. Therefore the hybrid is retro-directive with low incident power levels.

At high power levels, non-linear effects change the linear phase response of the system. Figure 40 shows the retro-directive simulation for the same rectifier with two

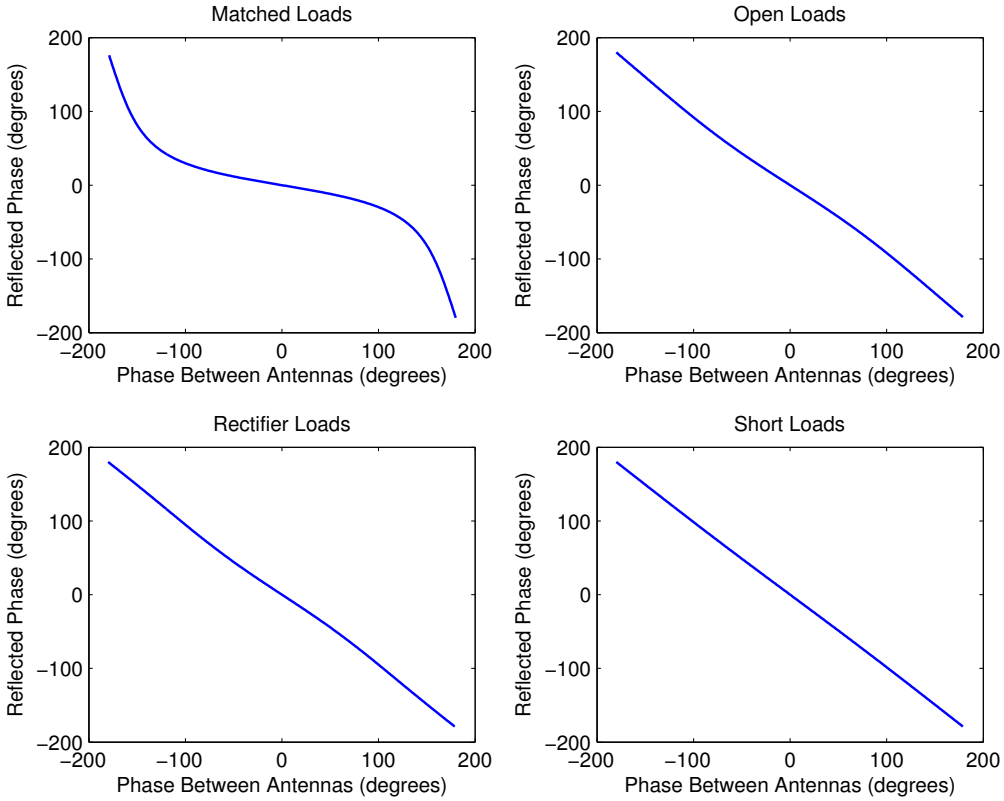

Figure 38: Phase response simulation for retro-directivity using an ideal circulator with various loads including: energy harvesting circuitry, open circuit, short circuit, and matched load

different power levels of -20 dBm and 20 dBm. At 20 dBm, the reflected phase is no longer a linear response, because the small signal assumption does not apply. The phase difference still approximately follows the expected linear response for retro-directivity, but there are added perturbations due to the non-linear diode element.

The magnitude at high power levels has large 20 dB dips at the peak locations for lower power levels. These dips are due to RF-to-DC conversions of the power. Instead of re-radiating the RF power, the rectifier is transforming the RF power to DC power. Even outside of the dips, the maximum re-radiated magnitude is 5 dB lower than the incident power.

Simulations show the 2-by-2 Butler matrix to be retro-directive and have staggered

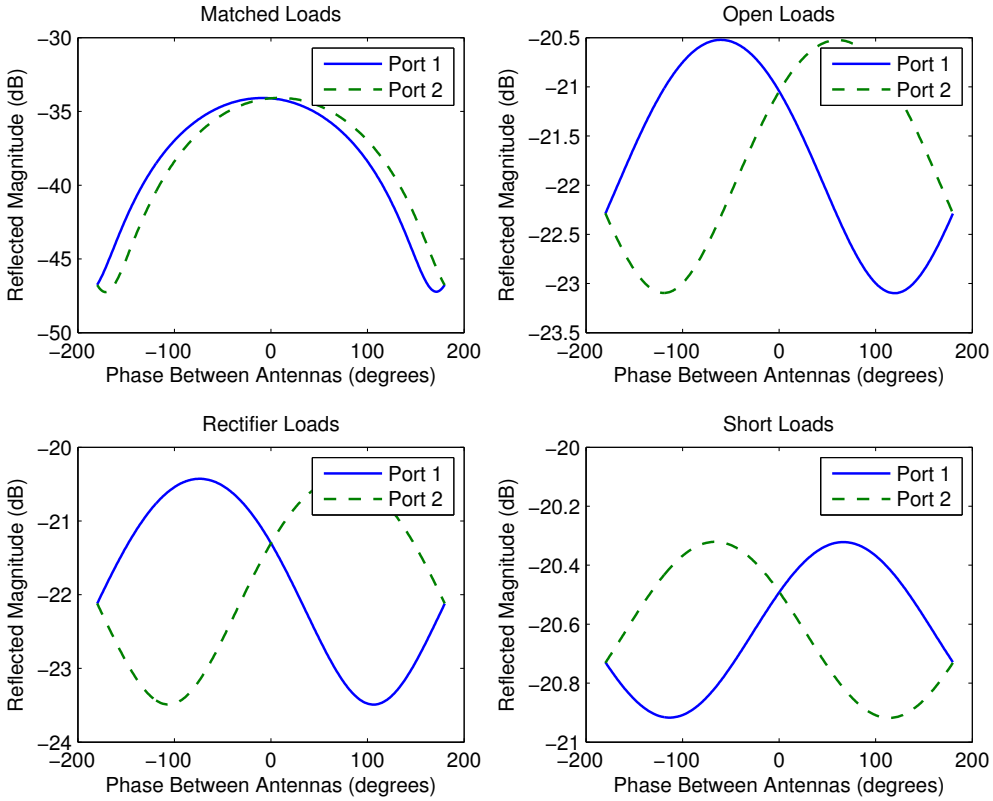

Figure 39: Magnitude response of retro-directivity simulations using an ideal circulator with various loads including: energy harvesting circuitry, open circuit, short circuit, and matched load showing equal power reflected for short and open and the matched load absorbing 99% of incident power

pattern energy harvesting qualities, this structure is capable of being used in a SPAR tag.

3.4 Implementing a 2-by-2 Butler as a SPAR Tag

To implement a SPAR tag with a 2-by-2 Butler matrix with two antennas, a 4-layer board is used to make the design more compact. The antenna ports of the Butler matrix are connected to two 5.8 GHz patch antennas separated by a half wavelength and two SMA ports are connected to the loads. The 2-by-2 Butler matrix from the Agilent ADS design is modified to conform to the location of the patch array and the 4-layer board structure shown in Figure 41.

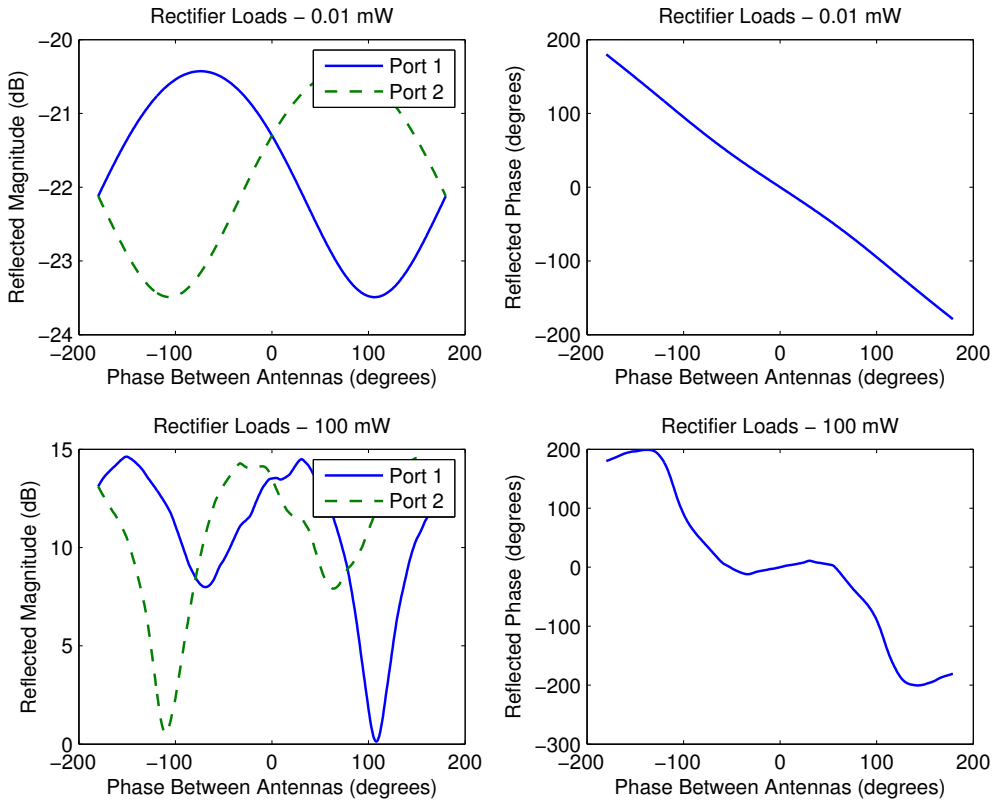

Figure 40: Magnitude and phase response of 2-by-2 Butler matrix with rectifiers loading the ports showing linear retro-directivity at low power levels but non-linearity at high power levels due to the diode response

The design is implemented on 4-layer FR-408 dielectric with a relative permittivity of 3.66 and loss tangent of 0.0127 at 5 GHz. The layer stack up for the SPAR tag is:

- Top Layer - 2-by-2 Butler matrix feed structure
- 2nd Layer - Ground Plane
- 3rd Layer - Empty
- Bottom Layer - Patch antenna array

The top layer uses microstrips to form a Butler matrix by using a 90 degree hybrid and is fed with two SMA connectors at Port 1 and Port 2. The 2nd layer is used as

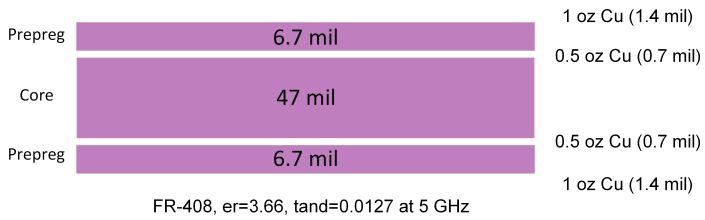

Figure 41: 4-layer board stack up for the 2-by-2 SPAR tag

the ground plane to keep 50 Ohm trace widths thin. The 3rd layer could be ground or left empty depending on the antennas used. For microstrip patch antennas, a thicker substrate improves the efficiency, therefore the 3rd layer is left empty. Using the same ground plane for both sides of the PCB may create interference, but, at 5.8 GHz the skin depth is much less than the thickness of the inner copper. The bottom layer has the patch antennas using the 2nd layer as the ground plane.

The geometry of the structure is optimized in CST Microwave Studio for minimal coupling between Port 1 and Port 2, minimal return loss on Port 1 and Port 2, and maximal peak gain. The final geometry is shown in Figure 42.

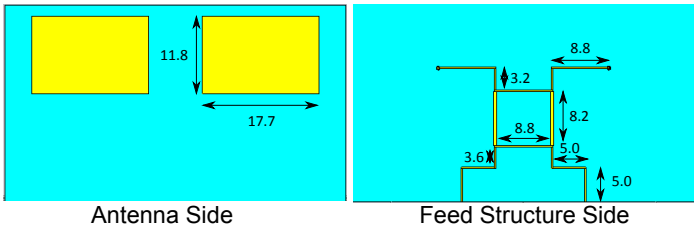

Figure 42: CST Optimized Geometry for a 2-by-2 SPAR Tag using a Butler matrix as the phasing structure (All units in millimeters)

The board is fabricated with OshPark and is shown in Figure 43. The antenna side is the shown on the left with two antennas with a through-hole feed while the 2-by-2 Butler matrix is shown on the right connected to two SMA ports.

3.4.1 VNA Measurements

Initial verification of the fabricated design is performed using a vector network analyzer (VNA). Port 1 of the VNA is connected to an excitation port through an SMA

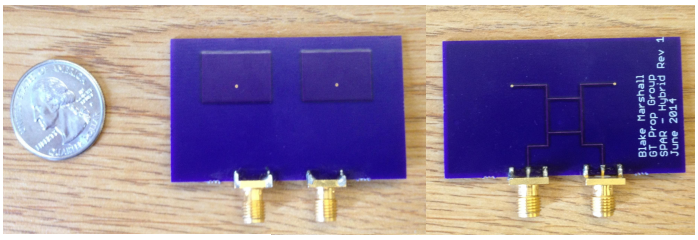

Figure 43: Fabricated SPAR tag with 2-by-2 Butler matrix on top layer and 2-element patch array on the bottom side

side mount connector and Port 2 is connected to the second SMA connector.

Since the tag is a symmetric device, S11/S22 are identical in simulation and approximately the same curve ignoring manufacturing differences in measurement. Figure 44 shows the curve from 5 to 7 GHz. In simulation, the resonance occurs almost exactly at 5.8 GHz, but after production and attaching the SMA, the resonance changes slightly and is not as deep. The amount of voltage reflected back into the VNA is approximately -16 dB or 2.5

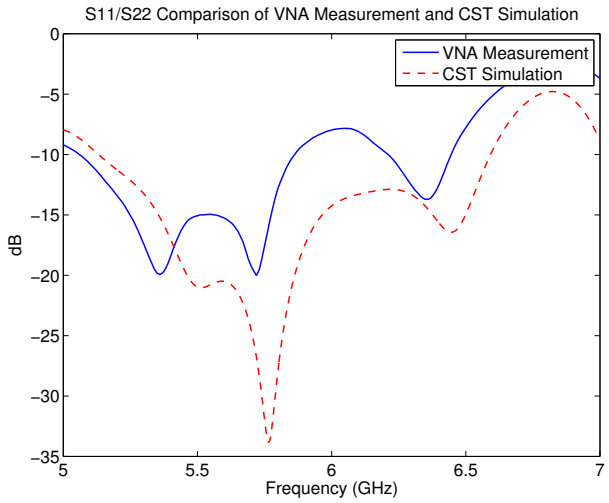

Figure 44: Return loss of each port for 2-by-2 Butler SPAR Tag showing a response under -15 dB at 5.8 GHz in both simulation and measurement

In addition to return loss, isolation is extremely important for switched beam devices, because each port must excite the antennas individually. The measured

isolation is only -10 dB so approximately 1% of power is lost exciting a non-antenna port. In simulation, the isolation is down at -18 dB with resonance exactly at 5.8 GHz. The difference in the results is due to the SMA connector that was not simulated in CST for simplicity.

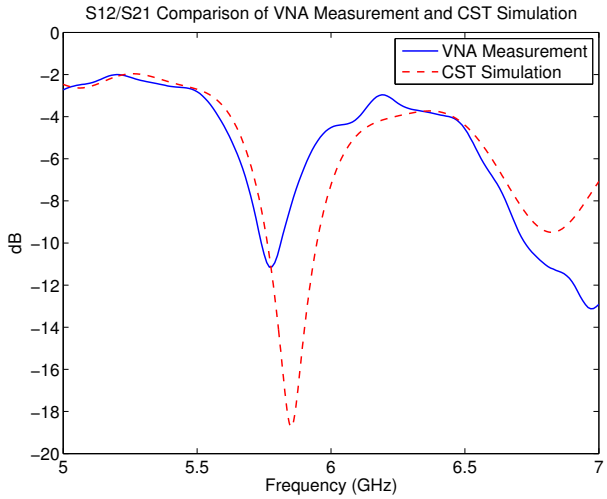

Figure 45: Isolation of Port 1 and 2 on the 2-by-2 Butler SPAR Tag around -10 dB to prevent cross-coupling between the switch beam patterns

Overall, the S-parameter curves matched simulations, but the variations were due to adding the SMA connectors to each ports. The SMA inner conductors were cut as short as possible to try to minimize their effects.

3.5 SPAR Tag Retro-directivity Measurements

The SPAR tag was confirmed to be retro-directive by measurements in an anechoic chamber at Georgia Institute of Technology Research Institute.

3.5.1 Anechoic Chamber Setup

The chamber was setup using a plane wave reflector, a VNA with two antennas, and a rotating platform for the device under test (DUT). One antenna was used for transmit on port 1 of the VNA and the other used for receive on port 2. These

ports are gated to ensure there is no direct cross-coupling between the antennas. The VNA transmits on port 1 into the large plane wave reflector which redirects the wave toward the DUT. The plane wave reflects off the DUT back to port 2 of VNA via the large reflector to measure scattering matrix parameter S_{21}. The overall setup is illustrated in Figure 46 and photographed in Figure 47.

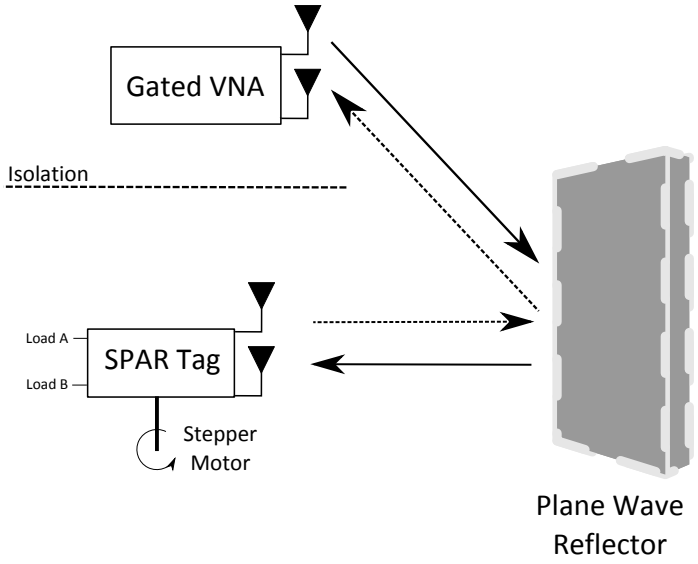

Figure 46: The chamber is setup to measure radar cross section (RCS) of an element by using a gated VNA and a large plane wave reflector. The device under test (DUT) is placed on a rotating stepper motor to collect RCS from multiple angles.

The rotation structure is a large fin with a stepper motor and a rotation platform on top. The fin has been engineered to have a very small radar cross section to minimize the effect on the DUT measurement. To mount the SPAR tag, styrofoam cups were used to support the DUT and minimize added RCS effects. Figure 48 shows a close up of the DUT in the testing setup with the top of the fin at the bottom of the photo attached to the rotating platform and SPAR tag mounted.

3.5.2 Measurement Procedure

Initially, the anecoheic chamber has to be calibrated. Despite its design to minimize RCS, the chamber has some RCS remaining. To calibrate and measure, the follow procedure was followed:

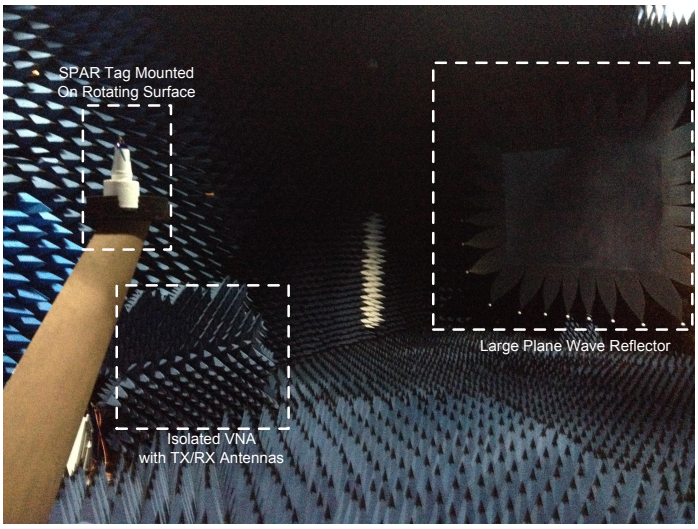

Figure 47: Anechoeic chamber setup for retro-directivity measurements showing the large plane wave reflector, TX/RX antennas and the VNA behind foam, and the rotation device for the DUT

1. Measure room with no DUTs
2. Measure with DUT of known radar cross section (RCS)
3. Measure with DUT of a different known RCS (not needed but used for verification)
4. Collect data with DUT (SPAR tag)

The room is initially measured with no DUTs to create a baseline for all measurements. Then, a DUT with a known RCS is used to calibrate the gains of the system to convert the S-parameters to RCS values. Another known RCS is then used to verify that the gain calibration is correct. After this process is complete, the chamber is ready to be used for measurements of DUTs with unknown RCS.

For this particular retro-directivity measurement, the tags response with various loads is measured by taking the difference between responses. Therefore, it is imperative that the testing setup does not change at all between measurements. After the SPAR tag was mounted, only the loads were varied and nothing else moved.

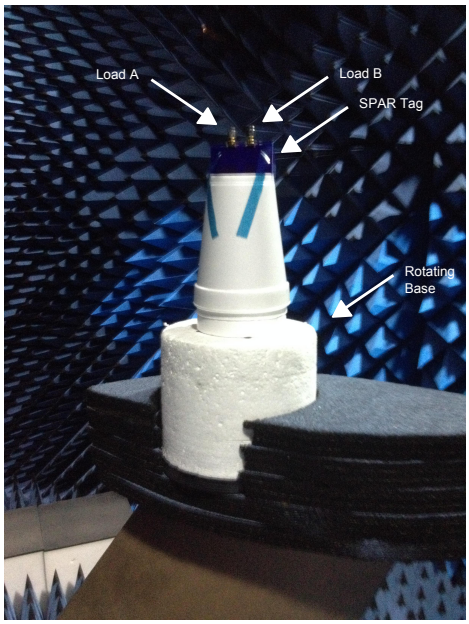

Figure 48: The SPAR tag (DUT) was placed on a calibrated rotating stand on a low profile fin

3.5.3 RCS Calculations

The SPAR tag's RCS is composed of two parts: structural scattering and antenna scattering. The structural scattering is due to actual physical size of the tag and materials it is composed of. Since there is a ground plane on one layer of the tag, the structural RCS is defined as rectangular metal shape with the RCS given in (50) [51].

$$\sigma_{struc} = \frac{4\pi b^2 h^2}{\lambda^2} \tag{50}$$

The other portions of the RCS response is due to the antenna re-radiation which can be related to gain of the antenna system through (51) with dependence on wavelength λ, tag antenna gain G_t, load impedance Z_{load}, and antenna impedance Z_{ant} [23].

$$\sigma_{rad} = \frac{\lambda^2 G_t^2}{4\pi} \left| \frac{Z_{load} - Z_{ant}^*}{Z_{load} + Z_{ant}} \right| \tag{51}$$

For SPAR tags, this equation is slightly more complex since Z_{load} varies spatially.

The angle of incidence determines which port is excited and therefore which load is seen in the RCS term.

Since the difference between two measurements is taken, it is imperative that the loads used are the same size. If they are largely different in size, the structural RCS will change in addition to the radiation RCS causing inaccuracy in the results.

3.5.4 Experiment

The experimental setup uses the 2-by-2 Butler SPAR tag that is rotated over 180 deg with various loads connected on the two ports. The two ports are changed between short, open, and load while S21 is measured. This experiment is normally called a retro-directive monostatic measurement because the measured angle is the angle of incidence. Any energy re-radiated in a different direction than incidence is not measured in this setup. Figure 46 shows the SPAR tag with Load A and Load B connections mounted on the rotating base.

When Load A and Load B are both terminated in 50 Ohm loads, only the structural RCS is measured. When terminated in open or short, the RCS response is the superposition of the structural and radiation RCS. Table 5 shows which RCSs are measured with various configuration of loads. For example, by taking the difference between a setup of Load A as an Open and Load B as 50 Ohms with a setup of Load A as 50 Ohms and Load B as 50 Ohms, the radiation RCS of an open circuit on Load A can be isolated. For RFID, this is the critical modulation RCS to communicate via backscatter.

The results become dependent on each port when both Load 1 and Load 2 are open or short since there are two different patterns that may be affecting the RCS results. If both ports are isolated, the aggregate pattern should be identical to the each pattern individually.

Table 5: Different loading configurations to measure for retro-directive measurement of SPAR tag with two loads

Load A	Load B	Measured RCS
50 Ohm	50 Ohm	σ_{struc}
Open	50 Ohm	$\sigma_{struc} + \sigma_{P1open}$
Short	50 Ohm	$\sigma_{struc} + \sigma_{P1short}$
50 Ohm	Open	$\sigma_{struc} + \sigma_{P2open}$
50 Ohm	Short	$\sigma_{struc} + \sigma_{P2short}$
Open	Open	$\sigma_{struc} + \sigma_{P1open} + \sigma_{P2open}$
Short	Short	$\sigma_{struc} + \sigma_{P1short} + \sigma_{P2short}$

3.5.5 Measurement Results

The results of the anechoeic chamber monostatic retro-directivity experiment are given as radiation RCS vs. angle as the DUT rotates. Since it is a monostatic measurement, the plots show the radiation RCS from each angle of incidence.

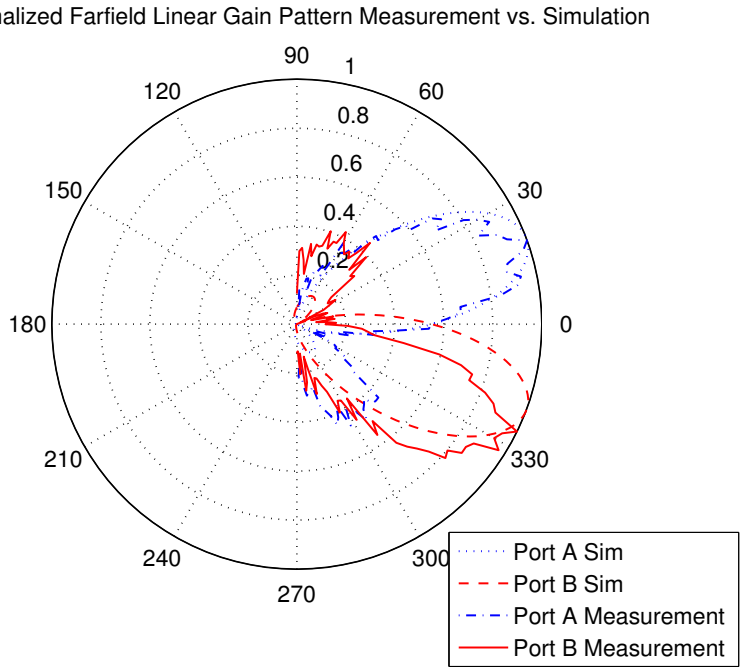

Figure 49: SPAR tag using 2-by-2 Butler matrix normalized gain pattern for each port in simulation and measurement in the chamber

Isolated measurements (non-measured port had 50Ω) of Port A and Port B are shown in Figure 49. The beamwidth of the Port A and Port B main beam are nearly

identical at 30 degrees. The Port B main beam's direction is slightly offset from simulation by 10 degrees. The overall experimental results are similar to the CST Microwave simulation.

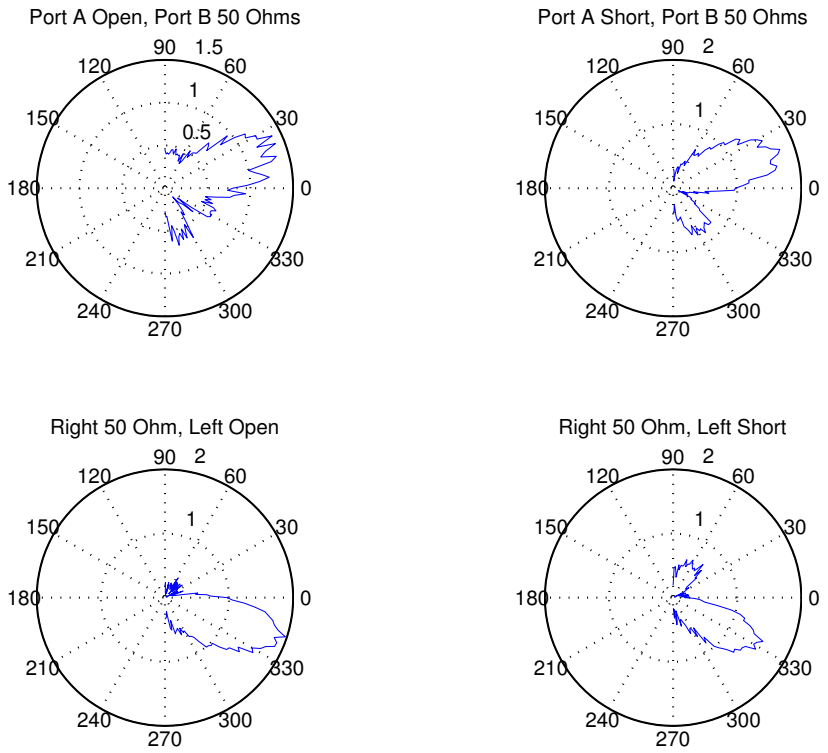

Figure 50: SPAR tag using 2-by-2 Butler matrix showing the results for *radiation RCS* only because the structural has been subtracted out for open and short on each port

The plots for isolated short and open of each Port are shown in Figure 50 with the first row showing open loading and the second row showing short loading. The first column is Port A and the second column is Port B. Each plot is calculated as the difference between the RCS of a single load as short or open and both ports loaded with 50 Ohms. For example, the top left graph is composed of two measurements. The first measurement is Port A open and Port B matched and the second measurement is Port A matched and Port B matched. The difference between these two measurements

is plotted. By subtracting, the structure scattering is removed.

The first row with Port A measurements shows retro-directivity in the +30 deg direction and the second row with Port B shows retro-directivity in the −30 deg. Both the short and open maintain retro-directive properties; therefore an RFID tag can modulate data and maintain retro-directivity.

To test isolation between the two ports, instead of loading the 2nd port with 50 Ohms, both ports were loaded with shorts or opens in Figure 51. The results show retro-directivity in both ±30∘ directions at the same time. Although the directions remain the same, the magnitude of the response diminishes due to cross-coupling between Port A and Port B. The poor isolation between the two ports results in non-orthogonal patterns which diminish the retro-directive effect. Ideally, a wave incident at ±30∘ should only excite either Port A or Port B, but the reduced magnitude shows that some energy is coupling into the isolated port. This is most likely caused due to the SMA connectors and their solder connection to the board.

The SPAR tag has retro-directive properties in simulation and experimentation. It would benefit from better isolation between Port A and Port B to improve performance when both are loaded with opens or shorts. All the results in the section for a 2-by-2 SPAR tag apply to larger N-by-N configurations.

3.5.6 Summary of 2-by-2 SPAR Tag

The 2-by-2 SPAR tag was shown to have both staggered pattern and retro-directive properties by implementing a 2-by-2 Butler matrix with two patch antennas. The simulations show the benefit of using a staggered pattern over single antennas or large arrays by balancing the tradeoffs between peak gain and beamwidth effectively. The measurements show the device's retro-directive properties and capable of modulating data on to the reflected wave.

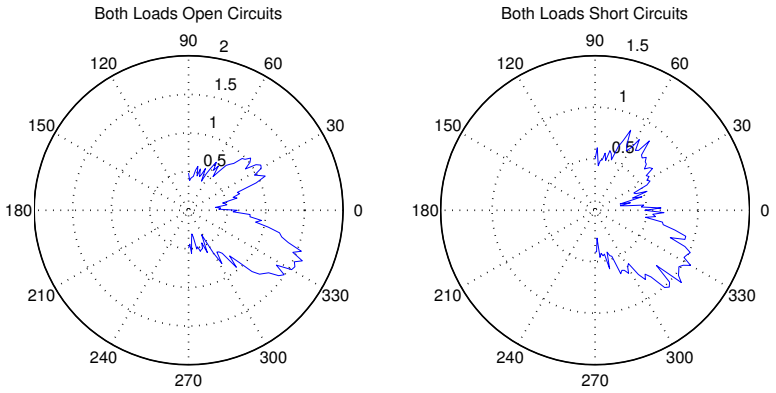

Figure 51: When both ports are loaded with open and short, the higher gain port dominates the performance and the SPAR tag is retro-directive in both ± 20 deg directions

CHAPTER IV

SPAR TAG IMPLEMENTATION IN 5.8 GHZ RFID SYSTEM

The objectives of this chapter are:

- To provide an example SPAR tag implemented in a 5.8 GHz RFID system.
- To demonstrate improved energy harvesting qualities of a SPAR tag versus a single antenna tag by increasing the peak power output in two different main beams.
- To demonstrate improved backscatter qualities of a SPAR tag versus a single antenna tag by measuring the reflected signal SNR at the reader.

This chapter demonstrates the effectiveness of SPAR tags with measurements made on a 5.8 GHz RFID system in Georgia Tech's Propagation Group lab. The experiment is composed of two tests: energy harvesting and backscattering. Each test compares two separate tags: the 90° hybrid SPAR tag and the control tag. The SPAR tag is designed based on the 90° hybrid in the previous chapters and the control tag is a traditional microwave RFID tag with a single patch antenna at 5.8 GHz.

4.1 System Overview

The RFID system is composed of a reader and a bistatic antenna unit at 5.8 GHz. The bistatic antenna unit has two antennas (top one for transmit and bottom one for receive). The transmit antenna is fed by an SMA cable from a power amplifier and the receive antenna is connected to the receive front end of the reader.

4.1.1 Antennas

Both antennas (TX and RX) are patch antennas with a directive cone covering them to slightly improve gain at the expense of beamwidth. The gain of the patch antennas is 6 dBi and have identical radiation patterns fed by an SMA connector.

4.1.2 Reader

The reader is composed of a continuous wave transmitter, custom-designed receiver RF front end, and a universal software radio peripheral (USRP) as a software defined radio (SDR) for the baseband signal.

Transmitter

The continuous wave transmitter uses a power amplifier and a 5.8 GHz oscillator to produce power levels up to 30 dBm. The CW signal is generated from the oscillator and passed through the power amplifier to the TX antenna and radiated into air.

Receiver

After reflecting off the tag, the modulated (from load and switch of the tag) waveform is collected by the RX antenna and passed through the receiving chain. The receiving chain begins with a lower noise amplifier (LNA) which is passed through the demodulation block. The RX front end uses a superheterodyne topology to demodulate the 5.8 GHz modulated waveform to baseband at an intermediate frequency (IF) before delivering the in-phase (I) and quadrature (Q) portions of the baseband signal to the USRP.

Universal Software Radio Peripheral (USRP)

The USRP can be programmed to sample up to 50 MS/s and then processed in software to decode the digitally sampled version of the analog baseband waveform. For the measurements below, binary phase shift keying (BPSK) modulation was used

with load modulation at 1 MHz due to its simplicity in comparing two pieces of hardware. Other types of encoding can be used such as Manchester or Miller to improve RFID tag range with only software changes.

4.2 Experimental and Control Tags Hardware

Two experiments are performed with the RFID system and the tags: energy harvesting and backscatter. Each experiment uses two tags: an experimental SPAR tag (90° hybrid with two patch antennas) and a control tag (patch antenna only) with either backscatter circuitry or energy harvesting circuitry. All four tags were custom designed for this experiment and manufactured by OshPark.

4.2.1 Energy Harvesting Tags

The two energy harvesting tags are designed with identical patch antennas at 5.8 GHz. The control tag has one patch antenna and a RF-to-DC Dickson charge pump energy harvester. The experimental tag is a SPAR tag implemented with a 90° hybrid, two antennas, and two energy harvesting circuits.

Control Energy Harvesting Tag

The control EH tag is a standard design for RFID tags at 5.8 GHz with one 5.8 GHz patch antenna connected through a capacitor to a 2-stage RF-to-DC Dickson charge pump. The patch antenna is connected to the energy harvesting circuitry through a single via as shown in Figure 52. The antenna is connected through C1 to a single package with two series diodes inside which finally terminate at C2 and a load resistance (RL).

SPAR Energy Harvesting Tag

The SPAR energy harvesting tag is similar to the control tag but two antennas, a feeding structure, and two charge pumps are used instead of one as shown in Figure 53.

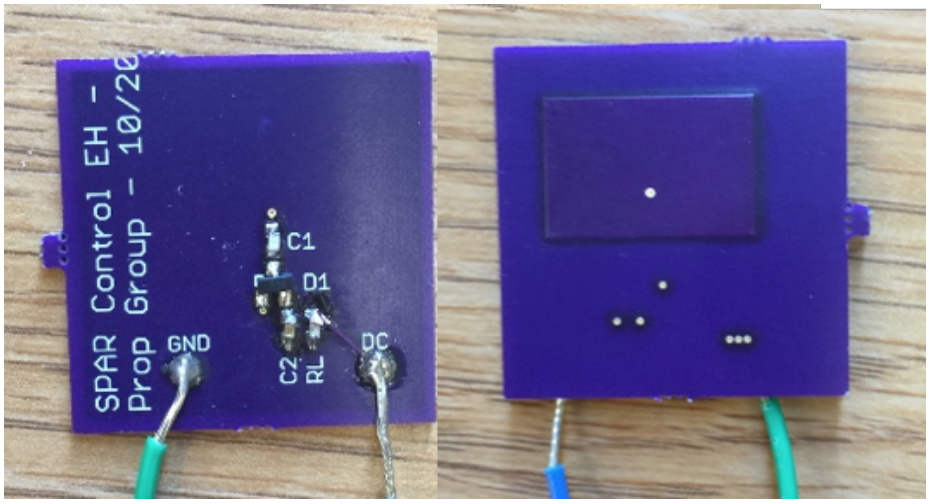

Figure 52: Control Tag for energy harvesting hardware with a single patch antenna connected to an RF-to-DC Dickson charge pump

The output of each charge pump is terminated on a single output resistance where the DC voltage to measured to calculate the received DC energy.

4.2.2 Backscatter Tags

The backscatter tags are designed to load modulate the antenna on the tag to send data back to the reader. Backscatter tags can use short and open loads for maximum SNR at the reader. While each tag uses short and open, the SPAR uses its retro-directivity to improve the SNR even farther than the signal constellation points alone can.

Control Backscatter Tag

The control backscatter tag is a basic RFID tag with a patch antenna, a RF switch for modulation, a microcontroller to control the switch, and a coin cell battery for power as shown in Figure 54. The circuitry on the tag is composed of the following:

1. MSP430F2132 - Low-power Microcontroller from Texas Instruments
2. 16MHz External Crystal
3. VSWA2-63DR+ - SPDT RF (500 to 6000 MHz) Switch from MiniCircuits

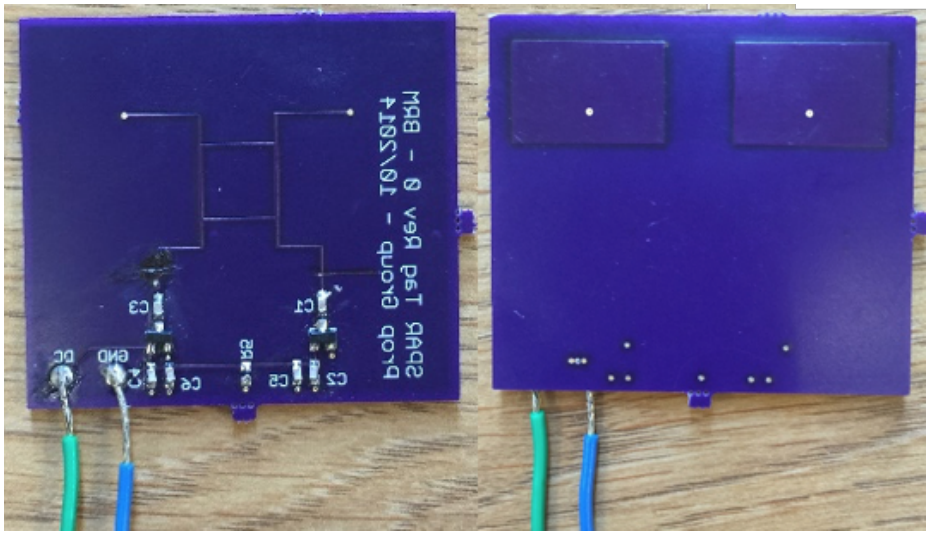

Figure 53: SPAR Tag for energy harvesting hardware with two patch antennas connected to two charge pumps via a 90° hybrid

4. 3V Coin Cell Battery

5. Programming Pins + Pull Up resistor for reset signal

The MSP430 controls the RF switch through an SPI MOSI port at the internal clock frequency (ACLK, MCLK, SMCLK, etc.) of the microcontroller. One output of the switch is connected to ground through a via while the other is left open to create reflection coefficients of -1 and +1. The changing reflection coefficient modulations the incoming RF signal at the frequency set by the microcontroller and it reflected back to the reader RX chain.

SPAR Backscatter Tag

The SPAR backscatter tag is slightly more complicated because it requires two patch antennas, 90° Hybrid feed structure, and two switches. It also uses the same microcontroller to control both of the switches at the same time from the same SPI MOSI line. The antennas are on the opposite side of the hybrid feed structure and each fed by a single via as shown in Figure 55.

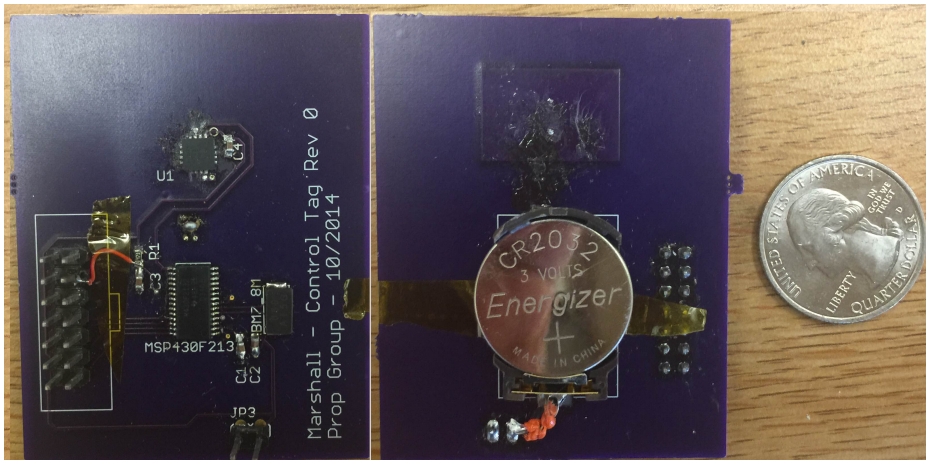

Figure 54: Control backscatter tag showing the microcontroller, RF switch, programming pins, and oscillator on the top side and the antenna and coin cell on the bottom side

Each switch is connected to one port of the hybrid, so each controls the load modulation of an orthogonal pattern of the tag.

4.3 Experimental Setup

Both experiments are setup in a similar fashion with the reader and two tags measured independently in the Propagation Group lab at Georgia Tech as shown in Figure 57. Each tag is setup on a stepper motor to rotate it and collect either the energy harvested or the reflected modulated waveform.

Each tag is rotated to get data of rotation angle versus energy harvested or SNR at the reader of the backscattered signal depending on which measurement is being performed as shown in Figure 56. Initially, the tag is lined up so the tag antenna and reader antenans are facing eachother. The tag is then rotated in 3° increments completely around back to the point where the tag and reader antennas face eachother. The stepper motor setup is two feet from the reader antenna unit with all the antennas with vertical polarization. All measurements were made with the transmitter at 30 dBm EIRP.

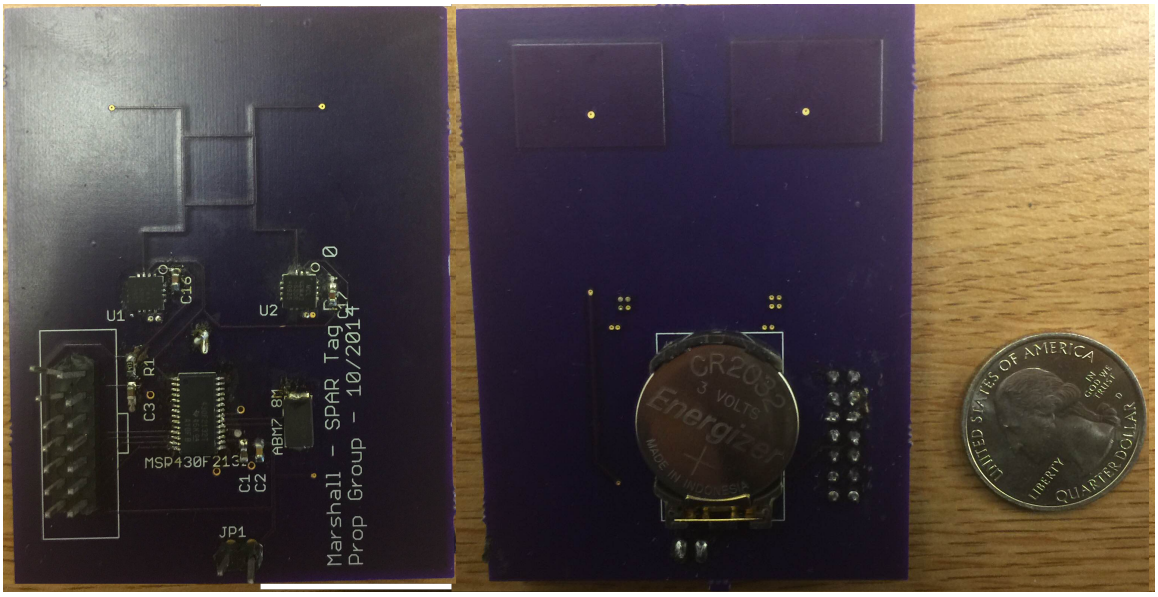

Figure 55: SPAR backscatter tag showing the microcontroller, RF switches, 90° hybrid feed structure, programming pins, and oscillator on the top side and the antenna and coin cell on the bottom side

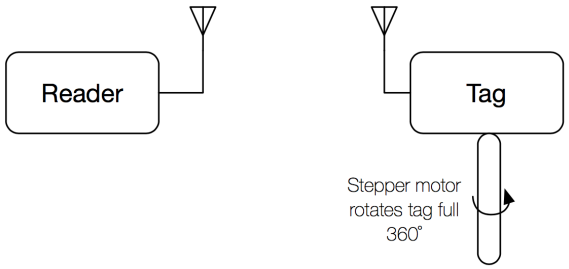

Figure 56: Tag rotates on a stepper motor over 360° while the reader remains stationary

4.3.1 Energy Harvesting Setup

The energy harvesting setup uses only the transmitter chain of the reader to output 30 dBm of power from the antenna. The transmitter uses a 5.8 GHz oscillator and a power amplifier.

To measure the pattern of energy harvesting efficiency, the SPAR tag and the control tag are connected to charge pump loaded by 3M Ohm resistor. Each energy harvesting tag uses the same energy harvesting topology as shown in Figure 58.

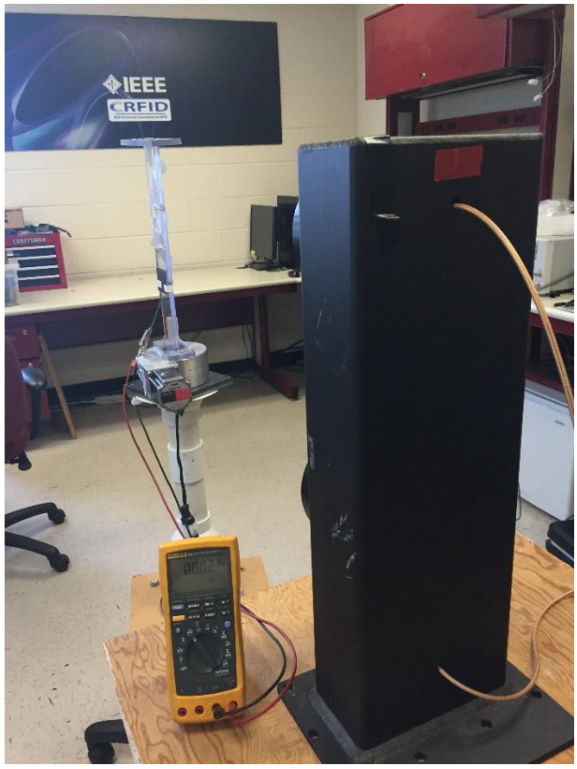

Figure 57: Propagation Group laboratory at Georgia Tech showing reader antenna unit and module to rotate tags under test

The antennas of tags receive RF power according to their radiation patterns while the charge pumps convert the RF power to a direct-current (DC) voltage over the load resistor. The received power can be calculated by the square of the DC voltage over the resistance of the load resistor. In other words, we can compare the efficiency of the energy harvesters by measuring the DC voltages.

4.3.2 Backscatter Setup

The backscatter setup uses the entire reader as well as the USRP to analyze the I and Q data at baseband from the front end of the receiver chain as shown in Figure 59. Similarly to the energy harvesting experiment, each tag is rotated on the stepper motor but data is collected from the USRP instead of the DC voltage on the tag. The reflected modulated wave from the tag is received and passed to the USRP where the symbol constellation can be mapped on the I-Q plane.

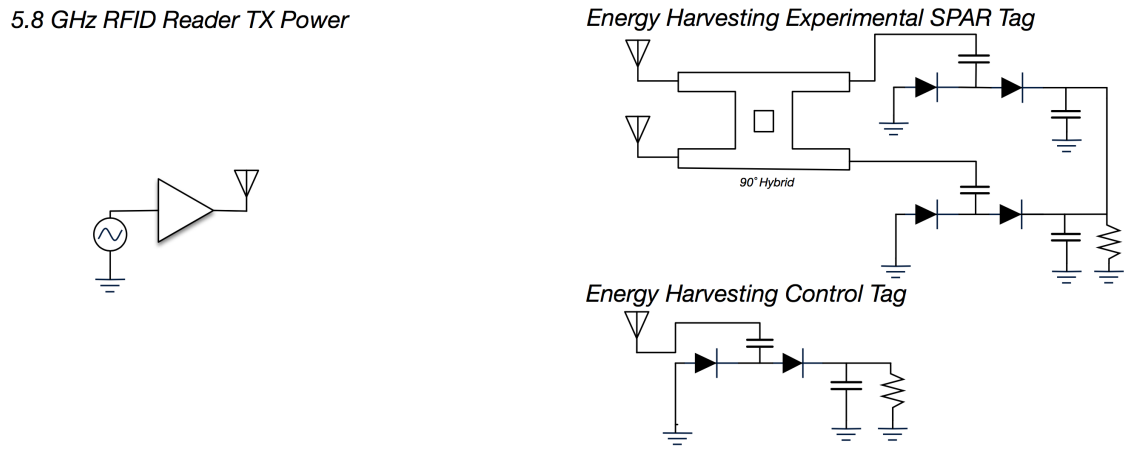

Figure 58: Experimental setup for energy harvesting measurement using the SPAR tag and the control tag to compare results

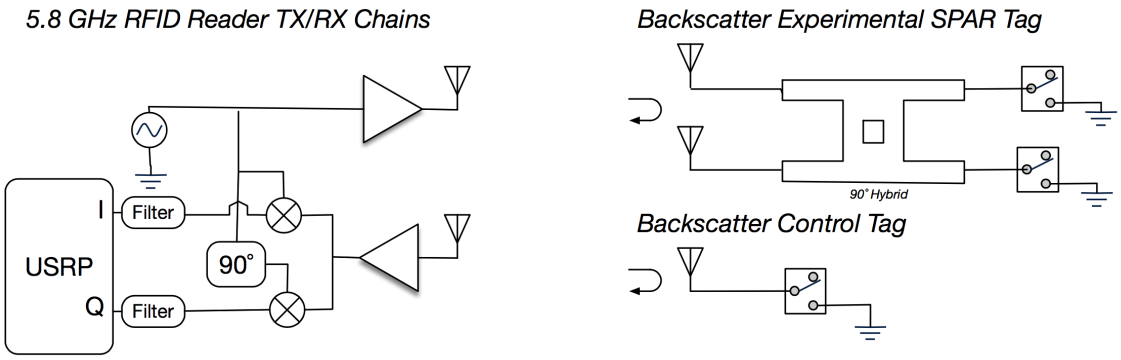

Figure 59: Experimental setup for backscatter measurement using the SPAR tag and the control tag to compare results

Since the symbols are 180° phase shift from each other (short and open), the symbols should be equidistant from the origin and on a line that runs through the origin. The line spins due to varying the propagation distance between the reader and the tag, but the distance between the two points determines the SNR as shown in (52). Probability of error (P_e) depends on the distance (d_{12}) between the two constellation points (s_1 and s_2) and the noise per bit (N_o).

$$P_e(s_1, s_2) = Q(\sqrt{\frac{d_{12}^2}{2No}}) \qquad d_{12}^2 = ||s_1 - s_2||^2 \tag{52}$$

Since the modulation values are -1 and +1 and the absolute value of a passive reflection coefficient cannot be larger than 1, there is no way to improve the modulation scheme for probability of error minimization. This leaves only the increase in signal received back to the reader due to the retro-directive nature of the SPAR tag. As the angle is varied, the distance between the symbols is captured as shown in Figure 60.

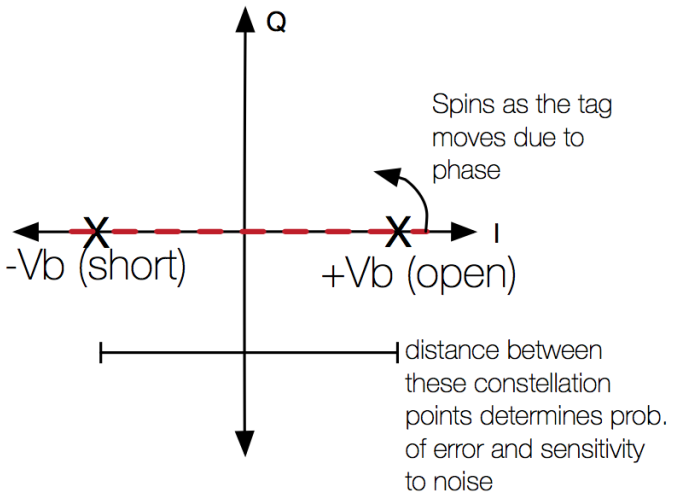

Figure 60: I and Q signal constellation diagram showing how phase may change and rotate the constellation but the signals remain the same distance apart unless the signal strength changes moving them farther apart (increasing SNR)

4.4 Results

The results of the experiment show that the SPAR tag outperforms the control tag in both energy harvesting and backscatter SNR.

4.4.1 Energy Harvesting Experiment

The results of the energy harvesting experiment shows that the SPAR tag does exhibit staggered pattern properties as expected with two clear lobes as showing in Figure 61. Unfortunately, the main lobes are not even which is created by asymmetry in the design. This could be due to the layout of the hybrid being imperfect or the wires hanging off the SPAR tag to make the measurements. In addition, the peak voltage

is only a few volts which correlates to an efficiency $< 1\%$ even at 30.5 cm foot away.

The low efficiency can be explained by a multitude of reasons mainly due to the fact that the charge pump was not matched to the antenna or optimized for performance. There are many different parameters to tweak in a charge pump for optimal performance as previously mentioned in this thesis and discussed in other papers cited.

When comparing the SPAR tag to the control tag, it becomes clear that the SPAR tag improves energy harvesting by both boosting the peak efficiency and widening the effective area of coverage in exchange for tag area. Unfortunately, the null in the middle results in a zone where the SPAR tag under performs a traditional single antenna tag as predicted from the simulations from ADS in the previous chapter.

4.4.2 Backscatter Experiment

The backscatter experiment shows similar results to the energy harvesting experiment in the sense that the SPAR tag shows two lobes of peak reflected signals, but, similarly, one of the peaks is much less than the other. The SNR shows a peak of 66 dB for the SPAR tag compared to 61 dB for the control tag which is close to the expected 6 dB different due to the gain squared term and the gain benefits of a 2-element array (3 dB). The SNR was calculated by integrating ± 1 kHz around 1 MHz of the magnitude of the I and Q signals and then doing the same thing with just noise.

The decibel calculation causes the null between the two main beams to be less intense than in the energy harvesting experiment. When the tags have been rotated to nearly $\pm 90^\circ$ to SPAR tag performs much better than the control tag, but most of the difference is probably due to multipath in the room or due to how the devices are connected to the test setup.

Overall, the backscatter experiment shows retro-directivity of the SPAR tag and outperforming the control tag everywhere except for the main null. In addition, the

main beams are not as even as expected but do clearly demonstrate two beams.

4.5 N-by-N SPAR RFID Tag

Building on the the measurement results from of a 2-by-2 SPAR tag, the results can be generalized to an N-by-N SPAR tag. In actual implementation, instead of using short and open for communications, the tag would use a short and an energy harvesting circuit as suggested in [16]. By doing this, the tags can support both retro-directive communications and staggered pattern energy harvesting (assuming the time constant of the storage capacitor and load resistance is long enough to support switching between loads). As charge builds up on the capacitors, a larger load can be engaged to drain the charge and perform some processing action such as responding with data on the switches. The charge is limited by the voltage on the output capacitor being above the brown-out of the circuitry, so a larger capacitor may need to be added on the output voltage node of the charger pumps.

When extrapolating from two to N in terms of hardware, there would be N different switches for each orthogonal pattern as shown in Figure 63. Each switch is required to have a separate energy harvesting circuit terminated on a common load and a short load which adds cost and physical area. By utilizing this area with components, a scattering structure, and an array, higher frequency passive RFID systems can achieve larger ranges than single antenna devices.

SPAR tags have major benefits over traditional tags by increasing the power-up and backscatter range of passive tags, but they require more physical area on the tag to support orthogonal patterns and circuitry.

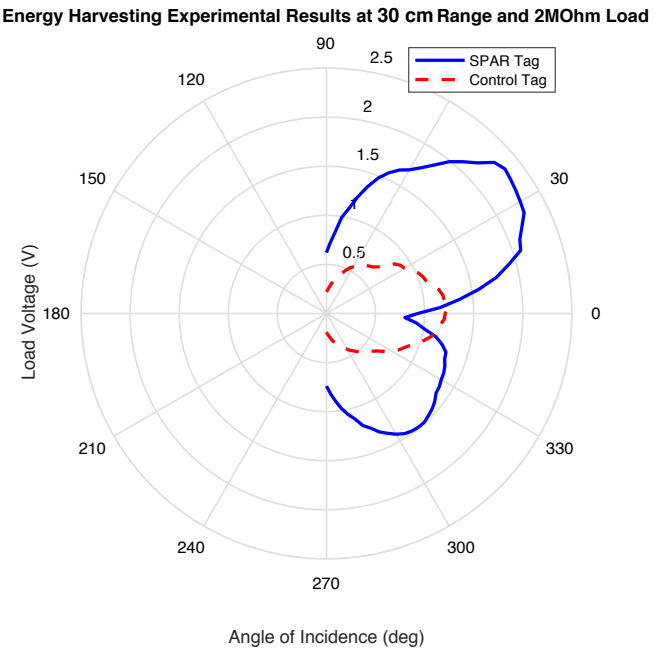

Figure 61: Experimental energy harvesting results showing the SPAR tag with two main lobes (one smaller than the other due to unintended asymmetry in the design) compared to the control patch antenna

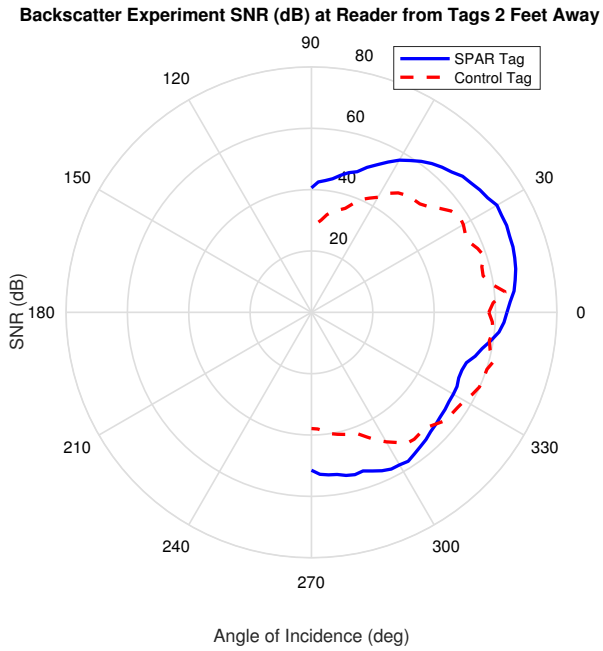

Figure 62: Backscatter experimental SNR results for the SPAR tag and control tag showing two main lobes that outperform the control tag

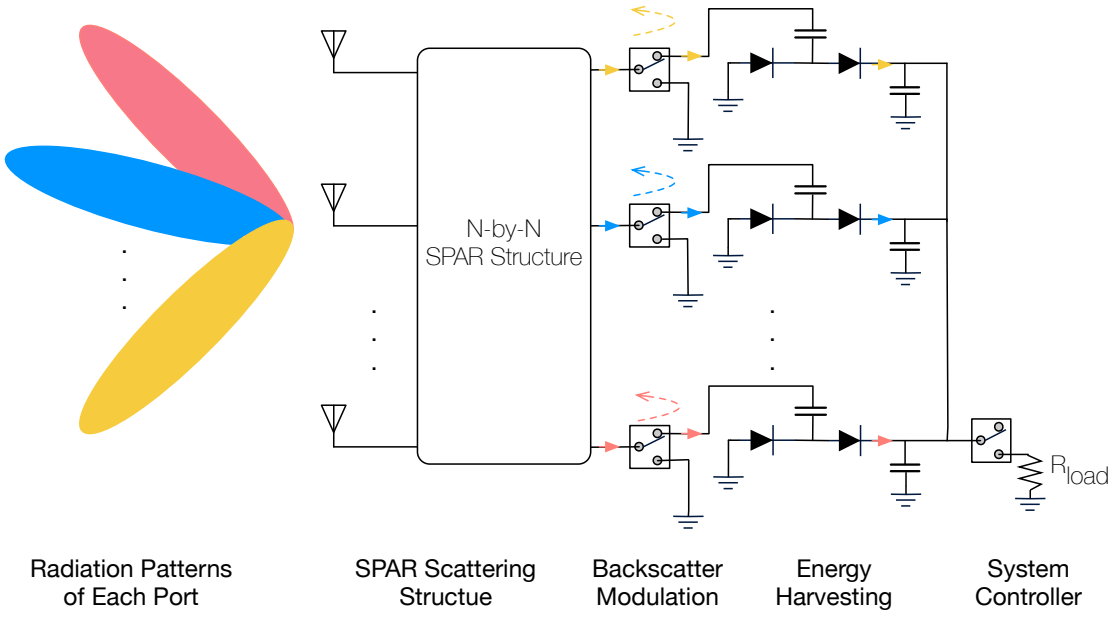

Figure 63: N-by-N SPAR far-field RFID tag using N switches with charge pump or short controlled by a single line from a microcontroller or state machine

CHAPTER V

DEVELOPING CUSTOMIZED SPAR TAGS

The objectives of this chapter are:

- To introduce a co-simulation software package capable of searching for new structures that can be optimized for size, bandwidth, etc.
- To demonstrate a new structure that meets the requirements of a 2-by-2 SPAR tag.
- To generalize the impact the optimizer could have on N-by-N SPAR tags as well as other microwave structures such as circulators, power splitters, etc.

It has been shown that canonical switched beam structures such as the 90° hybrid can produce the desired SPAR tag characteristics for passive RFID systems, but the next question is how can these designs can be improved? The main disadvantage of canonical beam forming designs is that it requires additional space on the tag. There are some strategies to minimize the physical size of canonical microwave structures for a given scattering matrix:

1. Minimize the effective wavelength by increasing the dielectric constant
2. Increase frequency of operation
3. Meander the transmission lines to keep the same effective length

But, customized (non-canonical) phasing structures could maintain the benefits of SPAR structures while minimizing the increased size impact on the tag. Or even a custom structure that itself is a radiating reconfigurable antenna aperture (instead

of using an linear array of antennas) that maintains staggered pattern and retro-directive properties. This chapter discusses software developed to discover a custom phasing structure.

5.1 Software Simulation Architecture

A custom lens or reconfigurable antenna should be a random metal structure that is fed from multiple ports and maintains all the properties for a SPAR tag. To find such a structure, an optimizer is developed in conjunction with an electromagnetic solver. The overall structure of the technique is shown in a block diagram is Figure 64

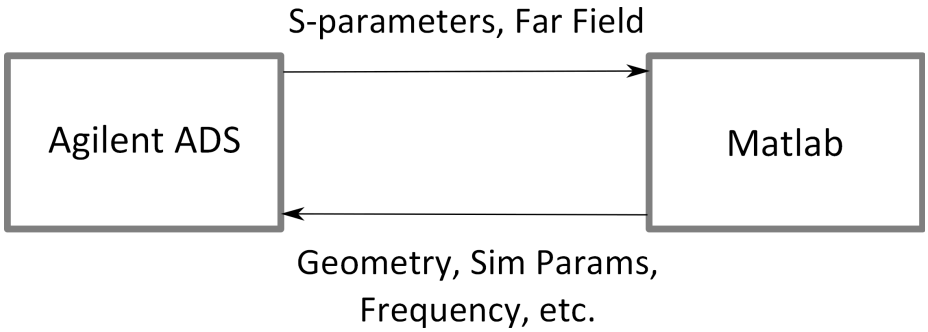

Figure 64: Block diagram using Matlab and Agilent ADS and the exchange of information

Matlab has scripts that generate text files that include the geometry, substrate information, vias, simulation parameters, frequency, port information, and folder information. These text files can be passed to Agilent ADS and it will run a Method of Moments (MoM) to solve the structures currents. With the currents, the S-parameters and far field pattern are generated and passed back to Matlab for processing.

With the structure and simulation results, Matlab can perform an optimization to reduce any cost function based on the results from ADS. In lieu of ADS, a custom computational EM solver could be implemented but has not been done. In addition, the Matlab scripts could be converted to Python for a completely open source software to create customized RF lenses and re-configurable antennas.

5.1.1 Software Requirements

As previously mentioned, the software requires two pieces of software: Matlab and Agilent ADS. This version of the software uses ADS2011.01 and Matlab 2015a Student Version. The code can run on Windows or Linux with small modifications.

The most intensive part of the software is the EM solver in Agilent ADS which, on Georgia Tech's license, limits us to 16 threads of computation. Therefore, only 16 cores on a machine can be operating on the problem at any one time. Agilent does offer a graphics processing unit (GPU) version that could be used for large scale optimization or a custom MoM/FTDT software could be implemented.

All Matlab code developed for this optimizer can be found here:

`https://github.com/bmarshall651/Microwave_Structure_Search`

5.1.2 Running Agilent ADS From Command Line

Running Agilent ADS Momentum solver from command line is simple once it has been setup correctly. To setup the software follow the steps outlined here (adapted from Agilent's help):

1. Set the following environment variables (for 64 bit Windows):

   ```
   set HPEESOF_DIR=<path_to_ADS_installation_directory>
   set ADS_LICENSE_FILE=<path_to_ADS_license_file_or_server>
   set PATH=%HPEESOF_DIR%\bin\win32_64;%HPEESOF_DIR%\bin;%PATH%
   ```

2. Create input files for simulation all in the same folder:

   proj.prt - Port Information

   proj.pin - Pin Information

   proj_a - Geometry Information

   proj.ltd - Substrate Information

proj.opt - Project Options

proj.sti - Frequency Stimulus Plan

proj.cfg - Configuration Folder Structure

proj.vpl (optional) - Far Field View Plan

Note: If unfamiliar with file structures, they can be exported from a current Momentum simulation by going to the Layout → EM Setup → Bottom Right Corner Drop Down → Simulation Input Files → Simulate. It will pop up with the location of the files. Find them and open them as text files.

3. Change your directory to the one that contains all input files.

4. Run Momentum from command line.

```
MomEngine -O -FF proj proj
```

In addition to running Momentum fully through as shown above, different options can be used for finer control of the simulator. If the objMode command 'RF', Momentum solves the problem uses a quasi-static solution, but if objMode is set to 'MW', a full wave solution is found.'-O' command can be used to run a simulation from pre-processing to which ever level specified.This is why '-O -FF' is used to run Momentum fully from pre-processing through far field analysis. Also, for newer versions of Agilent ADS the function to call the Momentum solver may be 'adsMomWrapper' instead of 'MomEngine'.

When configuring a system to run ADS from command line, it is best to use files already generated by the graphical user interface (GUI) to ensure proper operation. After verification, custom input files can be written and the solver can be used with confidence.

Table 6: Various options that can be called in conjunction with MomEngine adapted from Agilent's assistance

Simulation Steps	Command
Substrate file pre-processing	-T
Substrate database generation	-DB
Layout Pre-processing and mesh generation	-M
S-parameter model generation	-3D
Far field calculation	-FF
Other Options	**Command**
Run all steps to specified one	-O
Overwrite simulation mode	-objMode=

5.1.3 Calling Agilent ADS Momentum from Matlab

In order to connect ADS Momentum and Matlab, Matlab must order Momentum to solve geometries upon request. After setting up command line access for ADS, this is completed by simply changing the directory to the input files location and calling the Momentum engine.

For example:

```
system(['cd ' <folderPath>]);
system(['MomEngine -O -3D --objMode=MW proj proj']);
```

The commands set the folder path of the proj files to the current directory and run the Momentum engine from start to S-parameter simulation in full wave solver mode.

5.1.4 Software Limitations

For the student license, the solver was limited to only 16 threads during a simulation. The thread limitation inhibits the program from taking full advantage of cluster computing. If a custom solver is developed or the enhanced version of Agilent ADS is used, larger and more complex geometries can be solved and optimized.

5.2 Software Controls and Inputs

Geometries are inputted as a matrix into Matlab composed of many pixelated metal squares across the top of a PCB and a ground plane underneath. The metal structure, PCB stack up, frequencies, port selection, and unit cell size are all passed to the Agilent ADS engine to solve the structure for S-parameters.

Metal Geometry

The metal geometry to be simulated is a single, pixelated layer. The metal layer is represented by a binary matrix of ones and zeros with a given unit width for each cell. For example, with unit cell size of 1 mm and the following matrix:

$$A_{example} = \begin{bmatrix} 0 & 1 & 1 & 0 \\ 1 & 1 & 0 & 0 \\ 0 & 1 & 1 & 1 \\ 1 & 1 & 0 & 0 \end{bmatrix} \tag{53}$$

Each one represents having metal in the cell and each zero represents having air in the space as shown in Figure 65. Red cells shown are ports used as the references for the S-parameter matrix.

Stack-Up

The stack-up can be defined as any number of layers with various dielectric constants and conductivity. For these simulations, two-layer PCB with a relative permittivity of 3.66 and 1 oz copper on both sides. The bottom layer was treated as a solid ground plane and the top layer is etched with the metal pattern depending on the metal geometry matrix. If a simulation requires 4-layers with various dielectric constants and differently thickness of copper, for example, this can be set in the .ltd file as shown in the Appendix.

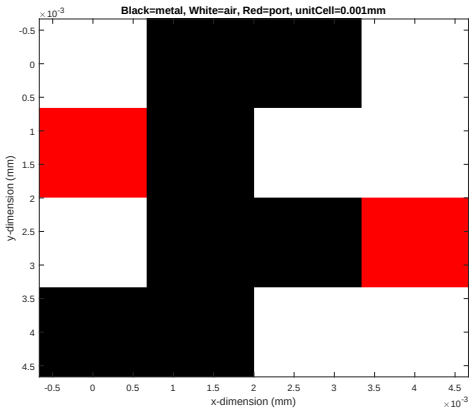

Figure 65: Example of the metal structure in the Matlab-ADS customized SPAR lens search algorithm showing black regions as metal and the red cells as the ports for the S-parameters

Frequency Selection

The frequency selection can be done at a singular frequency or a range of frequencies. The simulation frequencies are separated from the optimization frequencies, so the user can implement a simulation from 5 to 6 GHz in 0.1 GHz steps but only optimize for the 5.8 GHz simulation point.

Port Selection

The port selection of the geometries require two parameters: a location (x, y coordinate), conductor width of the port, and number of empty cells adjacent to the port on the edge. Ports are limited to being on the edges of the lens for simplicity but could be implemented to be fed from vias. The ports should be set up such that their impedance is a 50 Ohm transmission line so they can be fed from SMA cables when

Table 7: Microstrip parameters used for the substrate

Parameter	Variable	Value
Relative Permittivity	ER	3.66
Tangent Delta Loss	TAND	0
Substrate Thickness	H	1.7018 mm
Conductivity	COND	$5.7 * 10^7$
Width of Smallest Unit Cell	unitWidth	0.37 mm
X-dimensions Number of Cells	xdimNumOfCells	30
Y-dimensions Number of Cells	ydimNumOfCells	100

fabricated.

The ports are numbered and fed to Agilent ADS for the simulation to solve for the S-parameters. For example, in the example shown in Figure 65, there are two ports shown. Port 1 is on the left with a width of 1 unit cell and 1 adjacent cell blank on each side.

Symmetry

Symmetry is implemented in the code about the x-axis or/and the y-axis. Using symmetry, drastically reduces the possible solution sets for each cost function. For the M-by-N cells of the geometry, the solution set has 2^{MN} possible geometries, but by applying symmetry in both x and y axes, the solution set is reduced to $2^{(\frac{MN}{4}}$

Solver

The simulator uses Agilent ADS to solve the PCB structure with Method of Moments (MoM).

5.3 Control Simulation of a Microstrip

To show the solver in action, a simple microstrip is simulated with Agilent ADS MoM solver from the Matlab code developed for this exploration. The microstrip used the following parameters for the stack up, metal thickness, conductivity, unit cell width as shown in Table 7.

The geometry being solved is shown in Figure 66 with a single line of metal of 0.37 mm width. Each red dot on each side represents the ports used on each side for Port 1 and Port 2 of the calculation.

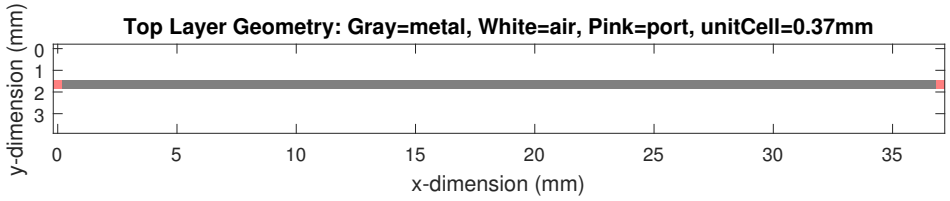

Figure 66: Example layout in Matlab simulator of a microstrip designed with the microstrip design equations resulting in a 0.37 mm wide trace from Port 1 to Port 2

After passing the matrix and parameters through Matlab, Matlab generates the proper files for Agilent ADS MoM simulator and the microstrip is simulated. The S-parameters results are written into the .cti file by ADS and Matlab interprets the results. Figure 67 shows the S-parameter results.

The magnitude shows that nearly all the power is transferred across the microstrip trace as expected. S11 remains less than -10 dB with a periodic pattern that is a function of the length of the trace as expected with transmission line theory. As for the phase of the signal, Figure 68 shows the results.

The phase also behaves as expected by theory across the 10 GHz band showing a dependence on the length of the microstrip line. The S21 phase is periodic at half the frequency of the S11 signal and the S21 phase changes linearly with frequency. As expected, for a given transmission line length, the phase should change linearly. From this basic simulation of a microstrip, it is shown that the simulator is working

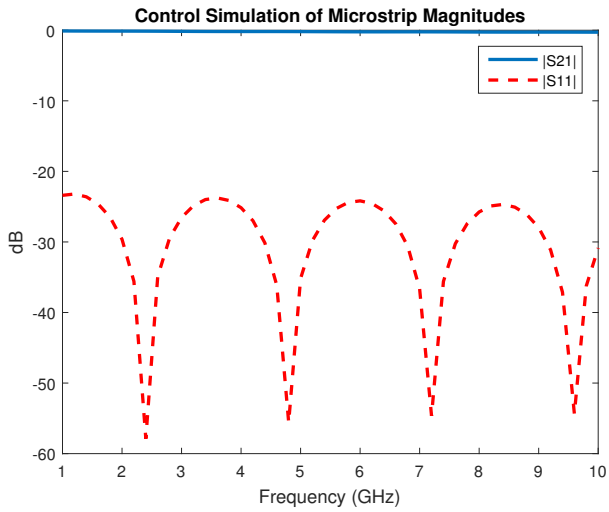

Figure 67: Magnitude of S-parameters from the control microstrip 0.37 mm wide simulated with the Matlab-ADS co-simulator

as expected. The next step is to develop the optimizer.

5.4 Optimization Algorithms

The goal of this optimization is to develop customized metal structures that have ortho-normal scattering matrix. This problem is different than other optimization problems due to the fact that it has in massive number of input variables but each variable can only be a 0 or 1 (non-metal or metal). This makes the optimization very challenging. There are many different optimization strategies that can be used such a genetic, random search, sequential, etc., but the basis for all of these is a cost function.

5.4.1 Cost Function

The cost function is the important aspect of any optimization technique. Since both magnitude and phase are important, the cost function must be complex. The final goal of the S-matrix is given as S_{ideal} which is a complex N-by-N matrix that is weighted based on a matrix W. The cost scattering matrix, S_{cost} is given in (54) where S is the simulated S-parameter matrix. The difference between S and the ideal

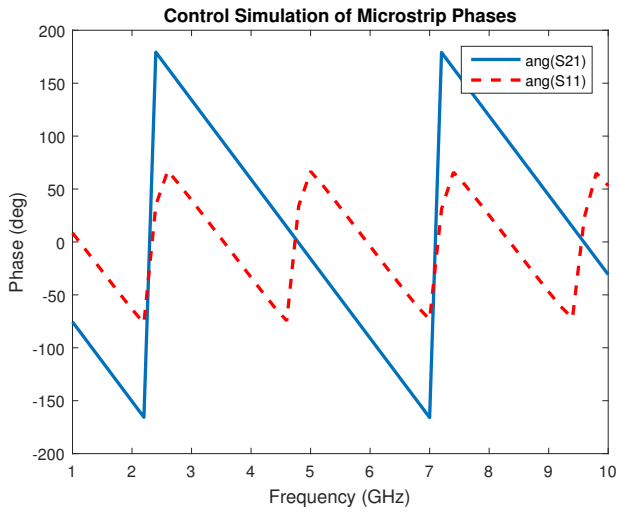

Figure 68: Phase of S-parameters from the control microstrip 0.37 mm wide simulated with the Matlab-ADS co-simulator

scattering matrix is taken to find the vector between each entry of the matrix. The difference is multiplied by a binary weighting matrix to choose which entries actually matter for the final scalar cost.

$$S_{cost} = W(S - S_{ideal}) \tag{54}$$

To calculate the final scalar cost value, the norm of the cost scattering matrix is taken as shown in (55). The norm is calculated by taking the square root of the product of the complex conjugate of the cost S-matrix and the cost S-matrix.

$$|S_{cost}| = \sqrt{S_{cost} S^*_{cost}} \tag{55}$$

Since each entry of S must be within the normal circle on the complex plane, the worst possible $|S_{cost}|$ is $2 * (N^2)$ and the lowest possible is zero. This system works well for a single frequency. But if multiple frequency points need to be used, the S-parameter matrix becomes a 3-dimensional matrix with the third dimension being frequency. To include this into the cost norm, it is simply summed up elementally and then divided by the number of frequency matrices used to get an average cost

over all frequency points.

5.4.2 Genetic Algorithm Search

Initially, a genetic algorithm optimization was used to try to find the optimal scattering matrix, but it did not work well.

Implementation

The implementation was using an initial random guess of a metal structure with a certain percentage of metal squares over the area. A population of these structures were created and called Gen 0. Each structure was evaluated individually by the ADS MoM solver for the S-params and the cost is calculated. If any structures are under the cost target, the optimization is complete, otherwise, a certain percentage of the population is killed off and the rest are used to produce the following generation as shown in Figure 69.

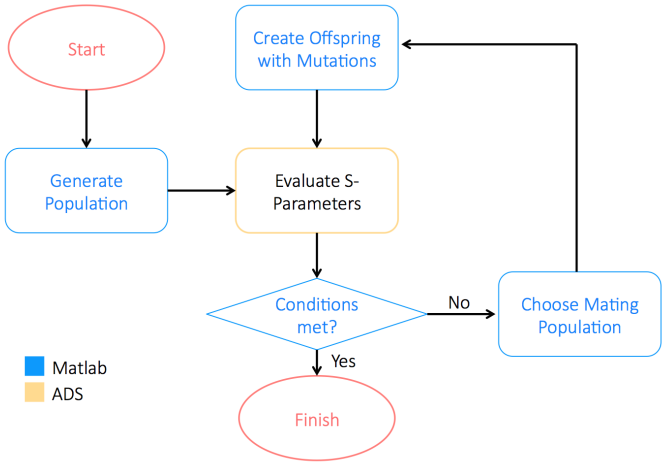

Figure 69: Flow chart of genetic algorithm optimization of a switched beam lens for desired S-parameters

Each successive population is created from the selected best members of the previous generation with added mutations and the generations repeat. Figure 70 demonstrates this process more concretely by showing each member of a generation and its metal structure.

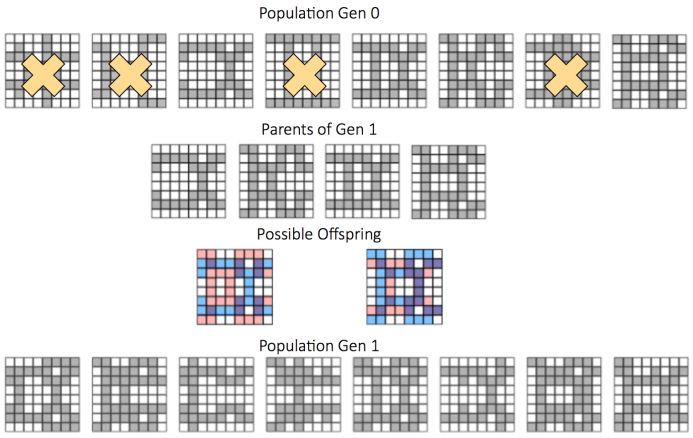

Figure 70: Example of how a genetic algorithm works for one generation

The first generation of structures is randomly generated with different amounts of metal on each. In this example, each member has metal for the input and output ports, but, this is not guaranteed by design. This problem is discussed more later.

The best members of Gen 0 are kept in this case its the top 50 percent and used to reproduce by overlaying two parents on top of each other. If both share the same either metal or non-metal on a cell, that value is kept for the offspring, but if they do not share the same value, then it is 50/50 that metal will be there in the offspring as shown by the purple cells in Figure 70. In addition to this cell-by-cell contribution from each parent, there is a mutation factor to add random flips of each cell based on a probability. This also caused a problem with no connection between ports.

Conductivity Issues

The genetic algorithm search suffered from issues of continuity between all ports. As previously alluded to, some of the generated structures ended up with disconnections in the metal structure. This results in very large costs for some offspring of two genetically "good" parents and a very discontinuous design-cost space. In order to solve this issue, the optimizer was adjusted to be a sequential search by starting with a full metal plane and remove each cell 1-by-1 and compare if the cost is lower.

5.4.3 Spatial Sequential Search

The spatial sequential search is much simpler than the genetic algorithm approach and avoids issues with conductivity.

Implementation

Each cell is numbered and sequentially increments from 1 switching whether or not the cell has metal and checks if the cost has decreased. If the cost has decreased, the structure is updated to reflect the change and it is incremented to the next cell with the cost threshold decreased. An example is presented in Figure 71.

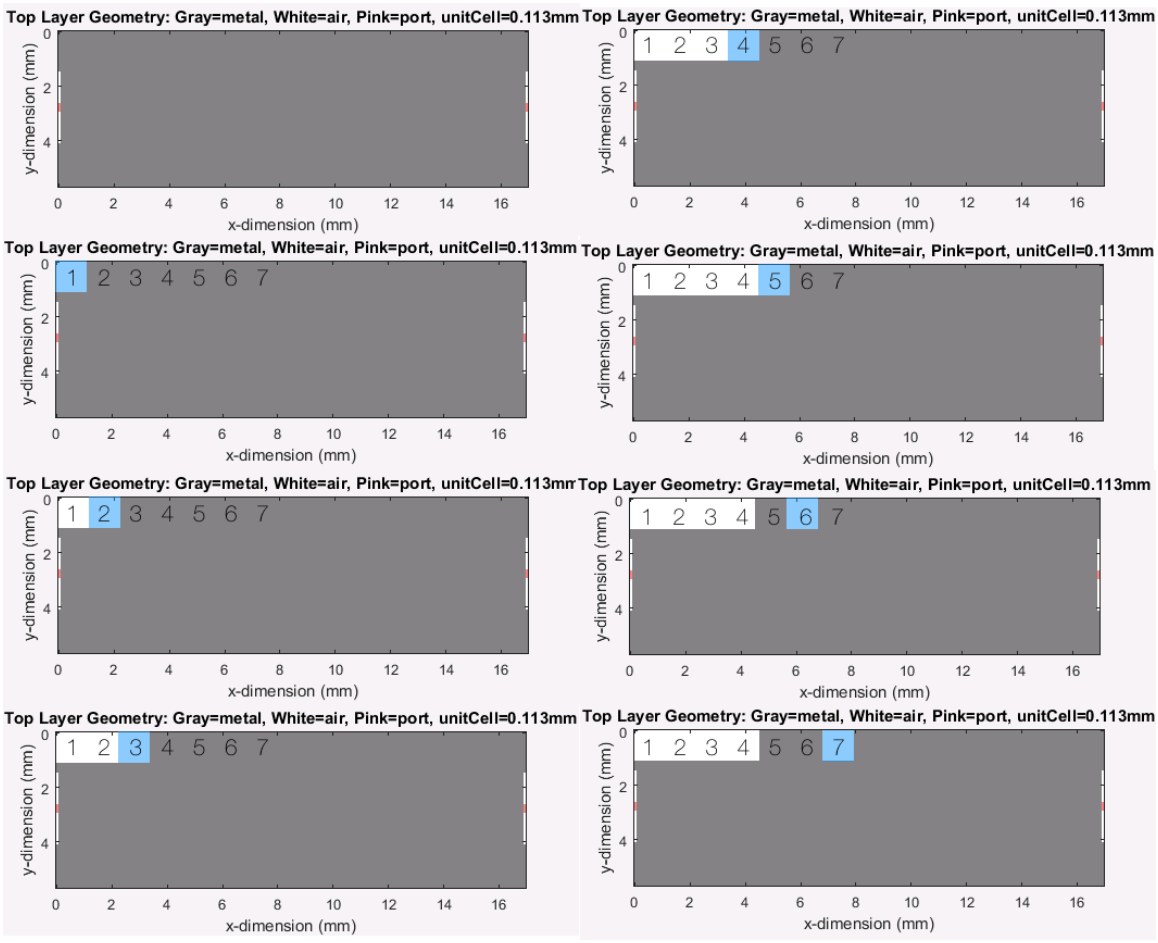

Figure 71: Example of how spatial sequential search is implemented to maintain conductivity at all times

Initially, the entire geometric space is filled with metal as shown in in the top left

corner. A cost is found by simulating the structure and it is saved as the best cost found. Then the metal is removed from Cell 1 and a new cost is calculated. In this case, removing Cell 1 metal improved the cost of the system, so it remains removed for the following iterations. This continues until Cell 5 where removing the metal increased the cost, so the metal stays in that location. The figure only repeats up to Cell 7, but in reality this continues throughout the entire structure. It is possible that it will repeat through all the cells again and this is called a "generation" or "cycle" for sequential optimization. Performing this cell-by-cell can very intensive to processing because of how many generations may be required to converge to a solution, so coarser cells were implemented in software to improve convergence time.

Coarse Cells

Coarser cells are used in sequential optimization in the earlier generations and shrink as convergence approaches. These coarser cells are made up of q-by-q unit cells across the entire structure. For example, in an optimization that requires 10 generations, the first three generations may use a coarser cell optimization of 10-by-10 unit cells. The next three generations may use 5-by-5 unit cells in the optimization followed by 2-by-2 unit cells for the following three generations. And the final generation uses the unit cell itself for each simulation.

Symmetry

As previously discussed, symmetry is included in the simulator. If symmetry is turned on, the sequential search only changes cells in the top half or the left half of the structure. The mirror image is used on the otherside to ensure x- or y-symmetry depending on the case. If both symmetries are required, the upper left corner cells are changed and mirrored to all three of the other quadrants.

5.5 Microstrip Optimization Example

A logical first goal is to create the simplest microwave structure with the optimizer before attempting more complicated designs.

5.5.1 Setup

The microstrip optimization is set up with a goal to find a lossless transmission line between two 50 Ohm ports with 160° phase shift between them as given in (56).

$$S_{ideal} = \begin{bmatrix} 0 & \exp(j160^\circ \frac{\pi}{180}) \\ \exp(j160^\circ \frac{\pi}{180}) & 0 \end{bmatrix} \tag{56}$$

The cost matrix is calculated as in (54) with equal weight on all four terms of the scattering matrix as described by (57).

$$W = \begin{bmatrix} 1 & 1 \\ 1 & 1 \end{bmatrix} \tag{57}$$

Physically the area is limited to 16.95 mm by 5.65 mm and uses the same substrate stack up as the previous microstrip design example. It is a two-layer board with all ground on the bottom plane. Other required parameters include substrate properties such as permittivity, tangent delta and conductivity of copper as shown in Table 8.

The physical area is broken up into 7500 square cells that are 0.133 mm by 0.133 mm that are called unit cells. Symmetry is not used in this optimization and the sequential optimizer is used. Each simulation runs from 5.6 to 6 GHz in 0.2 GHz steps and allows for metal to etched away or added for each unit cell. The maximum generations allows is 10 with a coarse cell list used to start with very coarse changes to the grid and slowly decrease it from 10 unit cells by 10 unit cells to 1 unit cell to 1 unit cell as demonstrated by the matrix.

Table 8: Parameters for the optimizer to find a microstrip with S21 = 1 with 160° phase shift

Parameter	Variable	Value
Relative Permittivity	ER	3.66
Tangent Delta Loss	TAND	0
Substrate Thickness	H	0.00017018 mm
Conductivity	COND	$5.7 * 10^7$
Width of Cell	unitWidth	0.113 mm
X-dimensions Number of Cells	xdimNumOfCells	150
Y-dimensions Number of Cells	ydimNumOfCells	50
X-dimension Size		16.95 mm
Y-dimension Size		5.65 mm
Symmetry About Y-axis	yAxisSym	Yes
Symmetry About X-axis	xAxisSym	No
Start Frequency	startFreq	5.6 GHz
Stop Frequency	stopFreq	6.0 GHz
Frequency Steps	stepFreq	0.2 GHz
Optimization Technique	optimizer	Sequential
Etching Only?	etchingOnly	False
Max Cycles	totalCycles	10
Homogenous Blocks?	homogenous	False
Randomize Blocks for Inversion?	randomizeMinors	1st Sim False 2nd Sim True
Coarse List	coarseness	[10 10 10 5 5 5 2 2 2 1]
Automatically Fill Coarse List?	autoCoarseList	False
Start Cost Frequency	startCostFreq	5.8 GHz
Stop Cost Frequency	stopCostFreq	5.8 GHz
Port Width	portWidth	3 cells
Result - Final Time Expired	timeHistory	0 days 23.1 hours

5.5.2 Results

The results found a sub-par solution for the 160° transmission line microstrip as shown in Figure 72. Obviously, the strange pattern could not have been developed by a human via a canonical microstrip design.

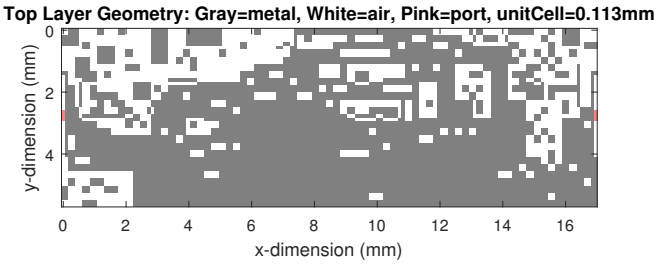

Figure 72: Final layout of the 160° phase delay microstrip

The final scattering matrix is shown in dB (58).

$$S = \begin{bmatrix} -16.3\exp(j164.0^\circ\frac{\pi}{180}) & -0.31\exp(j106.5^\circ\frac{\pi}{180}) \\ -0.31\exp(j106.5^\circ\frac{\pi}{180}) & -16.4\exp(j172.7^\circ\frac{\pi}{180}) \end{bmatrix} \tag{58}$$

The magnitude approached the goal value very effectively, but the phase angle could not be improved based on this algorithm. There are two unwanted effects that demonstrate themselves in this simulation of a microstrip:

1. Due to sequentially incrementating through the physical structure to remove metal, the resulting "trace" ends up on the bottom region of the structure. This can be fixed by adding randomization of the order.

2. Due to only changing the physical structure when the cost decreases, the cost monotonically decreases but can also get stuck in local minima (versus a global

minimum).

The latter effect is demonstrated in Figure 73 showing the cost decrease monotonically towards the optimal structure. For this simulation, only a lower cost updates the metal structure which results in a monotonic cost function.

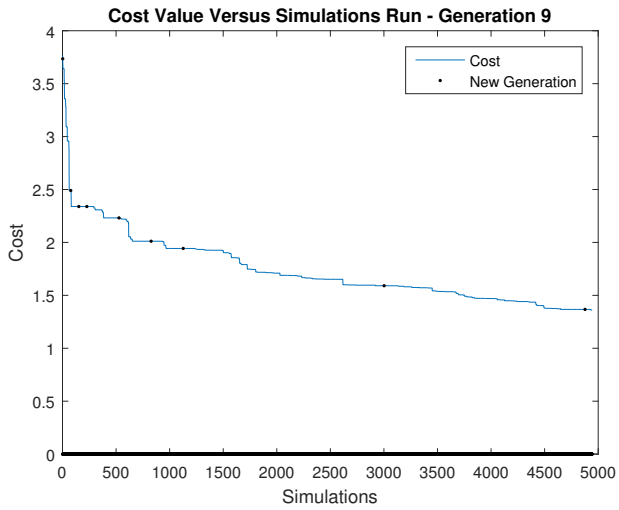

Figure 73: 160° phase delay lossless microstrip cost value after each simulation

The former effect is shown in Figure 72 with a large metal trace across the bottom for the length of the area. The order of flipping the cells should be randomized to prevent this effect from happening.

As for the coarseness profile used, Figure 74 demonstrates how larger squares are initially used to to flip and slowly moves down to smaller and smaller squares until 1-by-1.

The motivation behind using coarseness profiles is to accelerate convergence by getting the structure close to the optimal shape before changing individual cells to tweak the design.

5.5.3 Cost Space Investigation

To gain more intuition about how the optimizer works, the 2-by-2 scattering matrix can be fully visualized for a lossless microstrip. This is because the cost only has to

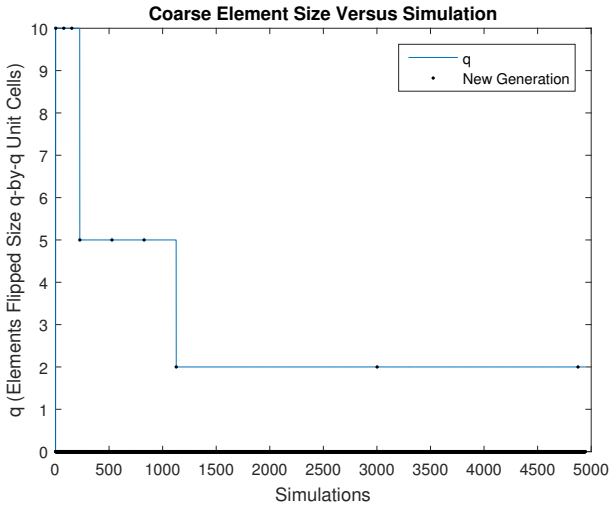

Figure 74: The coarsenss profile over simulations is shown here starting at 10-by-10 squares and ending at 1-by-1 cells flipping whether or not it has metal

depend on two variables magnitude and phase of the S21 parameter since the ideal matrix is reciprocal and lossless.

In Figure 73, the cost function (colored surface) is plotted versus $|S21|$ and $ang(S21)$ with red crosses overlaid. Each cross represents the cost value of each simulation as the microstrip progressed closer to the final goal of a lossless transmission line with a phase delay of 160°.

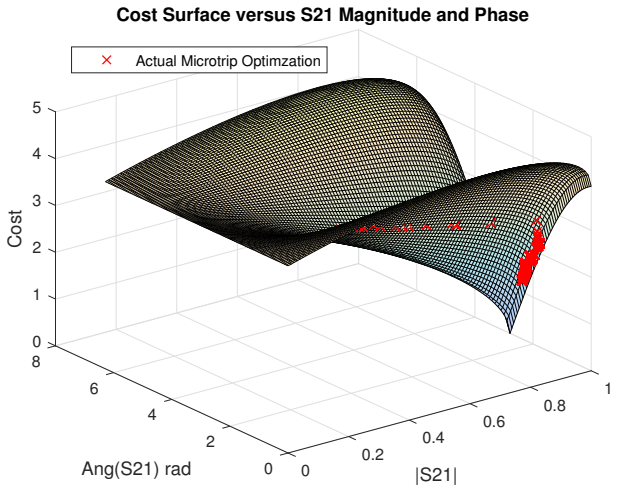

Figure 75: Three dimensional cost space to find a lossless transmission line with a 160° phase delay in terms of magnitude and phase

The cost function goes to zero where the phase delay is exactly 160° as expected and the amplitude of S21 is unity. In addition, the cost space is smooth in terms of these two variables and the slopes approaching the minimum are approximately equal as shown in Figures 76 and 77.

Another aspect that can be extracted from this visualization is the path that the optimizer takes to approach the minimum. Initially, it improves the magnitude of S21 until it is around 0.95 and then the phase is improved but more incrementally than the magnitude. The cost function behaves fairly well with slopes on the same order of magnitude for the both the magnitude and the phase. If one had a dramatically higher slope to the minimum, the cost function would be overly sensitive to either phase or magnitude, but in this case, it behaves well.

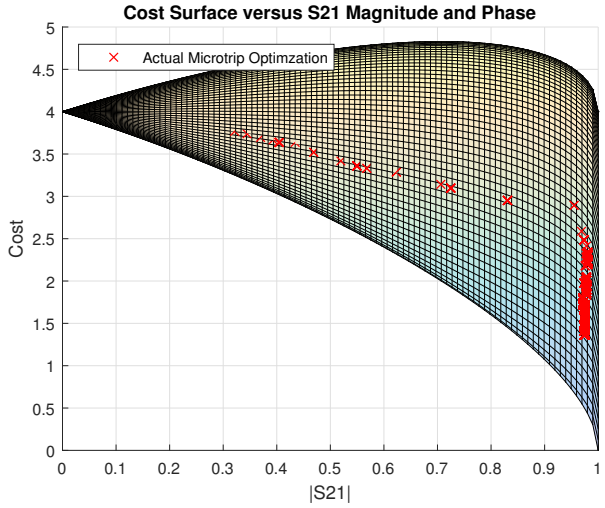

Figure 76: Three dimensional cost space to find a lossless transmission line with a 160° phase delay in terms of magnitude only

Although the cost space versus magnitude and phase is smooth and only has one minimum, it is vastly more simple than the cost function mapping the physical matrix of metal and non-metal unit cells to the cost. This space has many extrema and cannot be mapped mathematically but would require extensive empirical simulations. Not to mention how difficult it would be to visualize!

Figures 76 and 77 show the same graph projected to the magnitude axis and phase axis respectively.

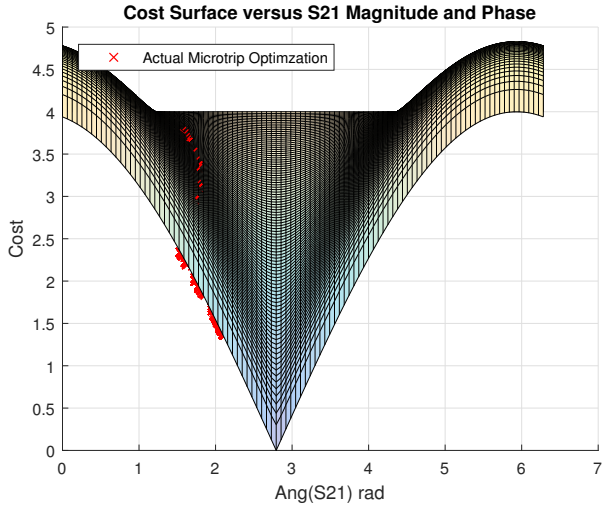

Figure 77: Three dimensional cost space to find a lossless transmission line with a 160° phase delay in terms of phase only

Notice how the magnitude seems to converge first before the phase converges to the absolute minimum. Despite the slopes being similar, this simulation converged the magnitude between the phase began moving to the minimum, but the phase never gets to 160° while the magnitude finds unity quickly.

5.5.4 Addition of Randomization and Symmetry

The control microstrip has been simulated using the sequential optimization, but there were some problems with it that must be corrected for an effective optimizer. This simulation adds two features: randomization of the minors to be flipped and symmetry of the physical structure.

The final structure is shown in Figure 78 showing the symmetry about the y-axis as well as the lack of the large bottom metal region, but metal regions in what appears to be three y-dimensions across the structure. The randomized minors eliminates the consistency of the "trace" going on the bottom but randomizes where it occurs in the y-dimension.

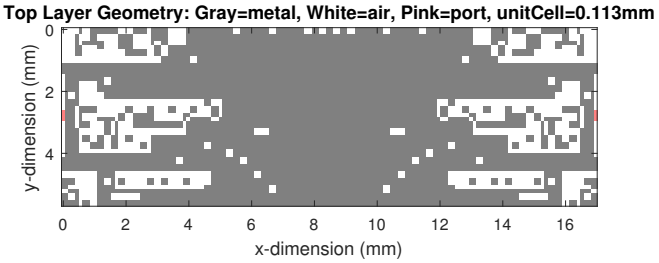

Figure 78: Microstrip structure with randomized minors and symmetry about the y-axis

As for the final S-parameter (dB, degrees), the randomization and symmetry also improved the final value as shown in (59).

$$S = \begin{bmatrix} -31.4\exp(j113.4^\circ\frac{\pi}{180}) & -0.27\exp(j141.2^\circ\frac{\pi}{180}) \\ -0.27\exp(j141.2^\circ\frac{\pi}{180}) & -31.2\exp(j113.9^\circ\frac{\pi}{180}) \end{bmatrix} \tag{59}$$

The magnitude values did not change much, but the phase delay improved dramatically from 106° to 141.2° while 160° remained the goal.

5.6 2-by-2 SPAR Structure Optimization Example

Instead of a basic microstrip with a phase delay, the optimizer can also attack the problem of finding 2-by-2 SPAR structures by chasing the cost matrix to (60) with weighting matrix (61)

$$S_{cost} = \begin{bmatrix} 0 & 0 & \frac{-j}{\sqrt{2}} & \frac{-1}{\sqrt{2}} \\ 0 & 0 & \frac{-1}{\sqrt{2}} & \frac{-j}{\sqrt{2}} \\ \frac{-j}{\sqrt{2}} & \frac{-1}{\sqrt{2}} & 0 & 0 \\ \frac{-1}{\sqrt{2}} & \frac{-j}{\sqrt{2}} & 0 & 0 \end{bmatrix} \tag{60}$$

$$W = \begin{bmatrix} 1 & 1 & 1 & 1 \\ 1 & 1 & 1 & 1 \\ 0 & 0 & 0 & 0 \\ 0 & 0 & 0 & 0 \end{bmatrix} \tag{61}$$

5.6.1 Setup

To set up the optimization problem, the solver requires physical area, port locations and widths, stack-up, frequency, and a goal scattering matrix. To compare it to the canonical 2-by-2 SPAR designed earlier, the physical area is kept about the same at 17-by-11.5 mm with an identical stack-up. The ports are set to be 50Ω evenly spread out on the east and west boundaries of the area. Each port is one-quarter of the height from the north and south ends of the grid.

The resolution of each cell is 0.113-by-0.113 mm and is a 150-by-100 cell matrix that begins with all copper flood except on either side of each port. Symmetry is used about both the x-axis and the y-axis since the goal scattering matrix is symmetric. The frequency is swept from 5.6 GHz to 6.0 GHz is 0.2 GHz increments, but for the cost calculation only 5.8 GHz is used. The optimization allowed for metal cells to be added or removed. These settings are outlined in Table 9.

5.6.2 Results

The final structure top layer (with a 2nd layer as all ground) discovered from the optimizer shown in Figure 79. The custom structure was discovered after the optimizer ran for 17 days starting with coarse 10-by-10 cell blocks inverting whether they were metal or non-metal. The inverting block slowly increments block-by-block throughout the structure and compares if the cost is lower than not inverting the cell. The lower cost version is kept and the block is incremented.

The cost function of the structure as each block is inverted is shown in Figure 80.

Table 9: Parameters for the optimizer example to find a 2-by-2 SPAR scattering feed structure

Parameter	Variable	Value
Relative Permittivity	ER	3.66
Tangent Delta Loss	TAND	0
Substrate Thickness	H	0.00017018 mm
Conductivity	COND	$5.7 * 10^7$
Width of Cell	unitWidth	0.113 mm
X-dimensions Number of Cells	xdimNumOfCells	150
Y-dimensions Number of Cells	ydimNumOfCells	100
X-dimension Size		16.95 mm
Y-dimension Size		11.3 mm
Symmetry About Y-axis	yAxisSym	Yes
Symmetry About X-axis	xAxisSym	Yes
Start Frequency	startFreq	5.6 GHz
Stop Frequency	stopFreq	6.0 GHz
Frequency Steps	stepFreq	0.2 GHz
Optimization Technique	optimizer	Sequential
Etching Only?	etchingOnly	False
Max Cycles	totalCycles	100
Homogenous Blocks?	homogenous	False
Randomize Blocks for Inversion?	randomizeMinors	True
Coarse List	coarseness	[10 10 10 10 10 5 5 5 2 1]
Automatically Fill Coarse List?	autoCoarseList	False
Start Cost Frequency	startCostFreq	5.8 GHz
Stop Cost Frequency	stopCostFreq	5.8 GHz
Port Width	portWidth	3 cells
Result - Final Time Expired	timeHistory	17 days 22.74 hours
Result - Final Cost	cost	0.6244

Initially, the cost is very high and slowly decreases as the structure is incrementally improved with each block is inverted. If the all blocks are inverted without finding a lower cost solution, this is considered a local minimum where the optimizer is stuck, so a random block is inverted. This results in upward spikes in the cost function which can vary from small changes to the cost value to large changes. For example, the peak near the 6000th simulation is pushes the cost almost back to where it started, but the cost function quickly returns back to the same low cost as before and escapes the local minimum. This is effectively a "mutation" in other optimization strategies. The lowest cost for the custom structure is 0.62 with the following scattering matrix (62).

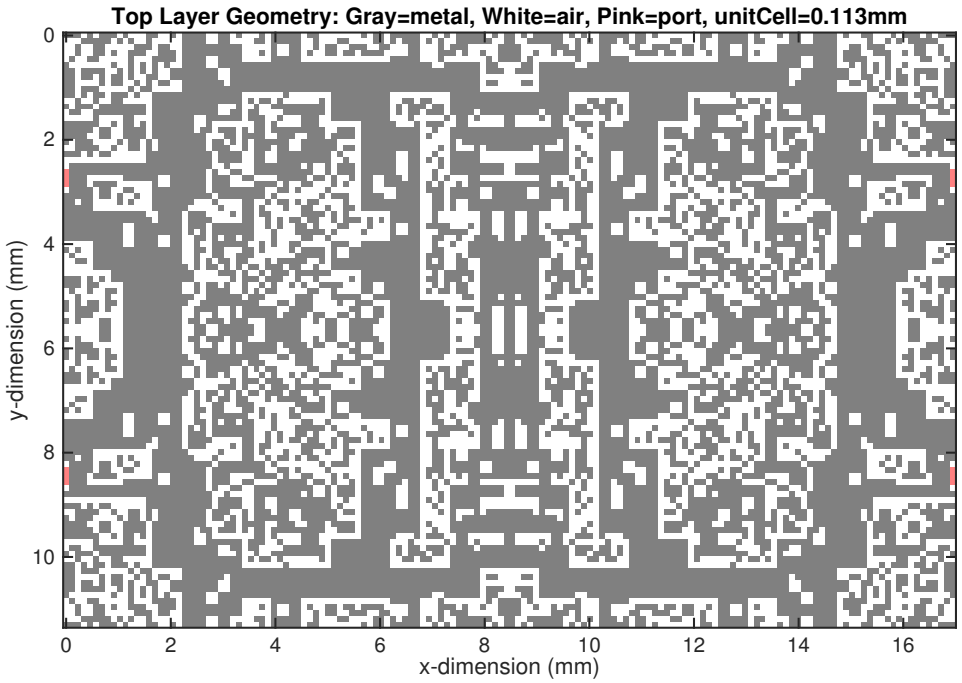

Figure 79: Custom Structure: Final geometry found with four ports shown in pink and the gray pattern showing metal with 0.113 mm cell size

Analyzing the cost plot more closely, one can see the more variability in the

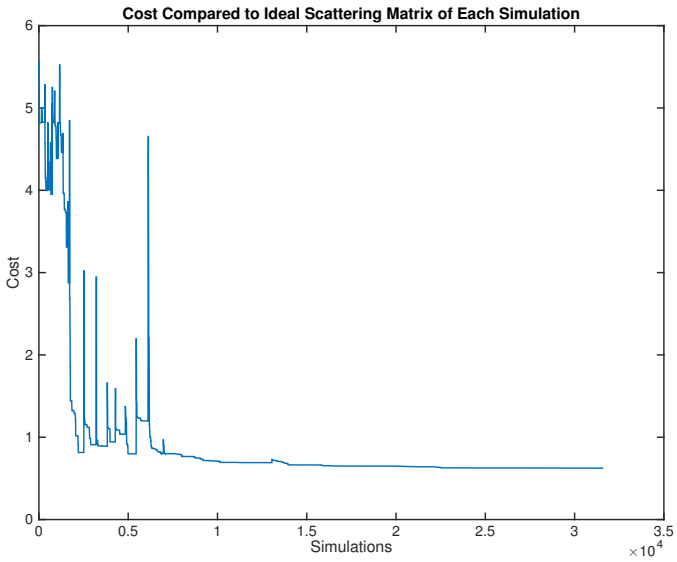

Figure 80: Custom Structure: Simulated and calculated cost of each geometry until the final optimized structure

earlier simulations of the optimizer. This effect is causes by using variable coarseness of blocks to get the solution earlier and then move to smaller block sizes as the simulation results approach the desired results. The coarseness decreases according to the coarseness matrix given to the optimizer which evenly divides up the number of complete cycles between each value given in the matrix. For example, the matrix given was [10 10 10 10 10 5 5 5 2 1], so it spends the first 50 cycles on 10-by-10 blocks. The next 30 cycles on 5-by-5 blocks, then 10 cycles on 2-by-2 cycles, and finally last 10 cycles on 1-by-1 cycles. This technique seems to improve the convergence time to see if a specific problem set up is plausible. For example, trying to find the same scattering matrix given in this example at 1 GHz did not start to converge at all after the 10-by-10 blocks completed. After leaving it running for days, it became clear that run could not come up with a solution and may be impossible to meet the criteria.

$$S_{CS} = \begin{bmatrix} -31.6\angle 80.2^\circ & -26.4\angle 103.3^\circ & -2.9\angle -95.3^\circ & -5.4\angle 178.6^\circ \\ -26.4\angle -103.3^\circ & -41.1\angle 77.7^\circ & -5.4\angle 178.1^\circ & -2.9\angle -97.0^\circ \\ -2.9\angle -95.3^\circ & -5.4\angle 178.1^\circ & -21.9\angle 137.8^\circ & -17.4\angle -85.1^\circ \\ -5.4\angle 178.6^\circ & -2.9\angle -97.0^\circ & -17.4\angle -85.1^\circ & -21.1\angle 133.0^\circ \end{bmatrix} \quad (62)$$

The custom structure provides acceptable isolation from the excitation port and the isolation port (around -30 dB). In addition, the input to output ports (S13 and S14 for example) are simulated with coupling of -2.9 dB and -5.4 dB. Unfortunately, the coupling to the each port is not equal resulting in non-unitary scattering matrices which in turn makes the radiation patterns non-orthogonal. This can be improved by changing the cost calculation to include a weighting for equality between the two output ports of the structure instead of just getting both as close to the ideal 2-by-2 Butler matrix.

In addition to magnitude, the phasing to the coupled ports are well matched to the 90° hybrid with each almost exactly at the -90° and 180° targets. The custom structure has coupled port phases at -95.3° and 178.6°. Both are very close to the required phases for orthogonality. The matrix is also fairly symmetric. The S44 versus S11 shows a large difference in magnitudes (10 dB) but both are very small absolute values which may be due to numerical error in solving the structure.

5.6.3 Analysis

The preliminary results show promise that using a spatial sequential search optimizer to find new structures that have unitary scattering matrices is possible. The physical space can be reduced and searched again to continue to find smaller and smaller structure that maintain the same properties as a canonical design such as a microstrip 90° hybrid.

Unfortunately, the process is time-consuming which can continue to be improved by adjusting the cost function of the engine. The search space is vast with many

Table 10: Comparison of 2-by-2 SPAR phasing structures 90° and custom structure of the same area 17-by-11.5 mm^2

S-param	**Ideal**	90° **Hybrid Measured**	**Custom Structure Simulated**
$\|S11\|$	$-\infty$ dB	-21.1 dB	-31.6 dB
$\|S12\|$	$-\infty$ dB	-15.5 dB	-26.4 dB
$\|S13\|$	-3 dB	-5.1 dB	-2.9 dB
$\|S14\|$	-3 dB	-3.8 dB	-5.4 dB

local extreme but by using a sequential search method continuity of the metal can be ensured which was a fatal flaw in the genetic algorithm.

Another interesting part of this optimizer is how it does not require any initial canonical design to start with. It simply needs an area, stack up, and impedance controlled ports to begin to find a specific scattering matrix.

Since the same area was used as the 90° hybrid SPAR tag for the feeding structure, the performance of the scattering matrices can be compared in Table 10.

The custom structure simulates to approximately the same S1x parameters as the 90° Hybrid structure. The custom structure and the measured 90° show asymmetry that is unwanted for the ideal 2-by-2 SPAR scattering matrix but exists in the measured hybrid as well. This results in non-orthogonal radiation patterns and less than ideal SPAR structure. Overall, the comparison shows that the optimizer was successful in finding a custom structure that has similar properties to a 90° hybrid with the same stack up and physical size.

5.6.4 Frequency Response

Although the structure is optimized at 5.8 GHz for SPAR properties, the frequency response of the structure can be analyzed from 1 to 10 GHz as shown in Figure 81. The frequency sweep shows that the device only operates as intended at 5.8 GHz but has a limited bandwidth around the point of operation on the magnitude graph. Unfortunately, when analyzing the phase response, as the frequency moves out of

the bandwidth, the phase drifts away from having the proper phasing for a unitary scattering matrix.

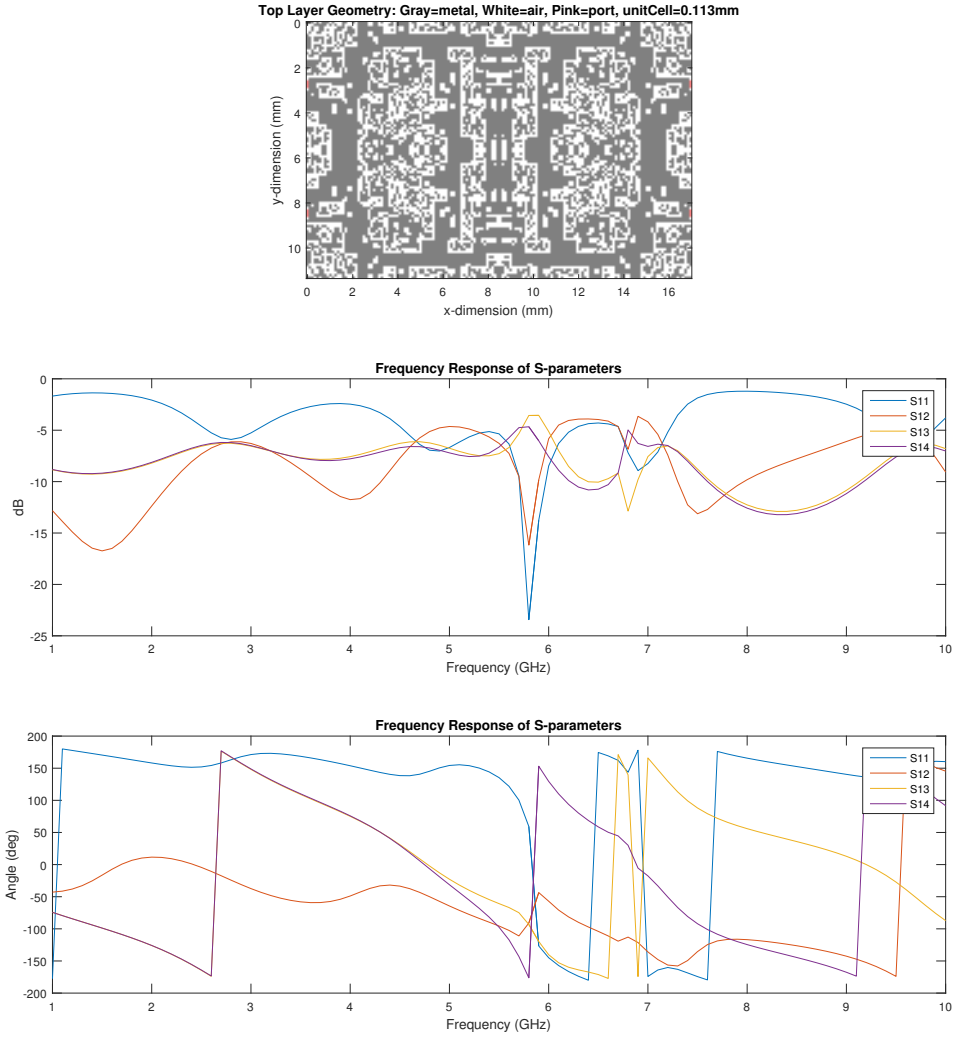

Figure 81: Frequency response of the custom structure found for 2-by-2 SPAR properties

5.7 Generalizing the Optimizer

The optimizer is generic enough that it is not limited to only 2-by-2 unitary scattering matrices for SPAR tags. The scope includes larger N-by-N SPAR tag designs and

other microwave devices.

5.7.1 Larger N-by-N SPAR Tags

The custom lens result demonstrates that a 2-by-2 SPAR structure can be found, but this optimization technique can also be applied to larger N-by-N Butler matrices. Figure 63 demonstrates the general schematic of an N-by-N SPAR tag but does not define how to implement SPAR scattering structure. A canonical design using hybrids and cross-overs or a Rotman lens could work, but there could also be a smaller structure or a wider bandwidth structure. For example, there may be space requirements and location of the ports that are required to fit the scattering structure. The optimizer is capable of searching this space for the best scattering matrix.

5.7.2 Other Microwave Devices

This piece of software is also not limited to finding orthogonal scattering structures, but it can design various microwave structures such as circulators, directional couplers, etc. with constrained space.

In addition, the optimizer can search for structures at low frequencies in small areas. For example, if an engineer needs a design at 1 GHz in the same area that fits a 5.8 GHz circulator, the optimizer can search for a circulator that fits but may have slightly reduced performance. In some applications, this may be an acceptable trade-off.

Another generalization of the optimizer is multi-band structures. For example, if an engineer needs a directional coupler that works at 1 GHz, 2.4 GHz, and 5.8 GHz, the optimizer is capable of including these different frequencies in the cost function. Although it may be very slow to simulate wider frequency ranges, it is possible with the optimizer.

CHAPTER VI

CONCLUSION

6.1 Summary

In conclusion, this dissertation has proposed a staggered pattern and retro-directive (SPAR) RFID tag that uses unitary scattering matrices to feed linear antenna arrays to passively improve RFID tags. SPAR tags are shown to improve the power-up and backscatter range of RFID tags from a reader by increasing the physical size of the antenna and feed structure of the tag. The additional RF structures enable the tag to passively switch between multiple radiation patterns to aim the main beam toward the reader.

The concept is introduced by using the Stein limit to show that the ideal SPAR tag must have spatially orthogonal radiation patterns. To generate orthogonal patterns, linear arrays must be fed by unitary scattering matrices such as the Butler matrix. These scattering matrices can be formed physically by many different structures such as Rotman lenses, microstrip feed networks, etc. By combining the antenna array and unitary feed network with a loading modulation switch and RF-to-DC energy harvester (or a multi-antenna port RFID chip), a SPAR RFID tag is created.

Although SPAR tags can be N-by-N, the focus of these efforts are on a 2-by-2 SPAR tag which requires two antennas and a microstrip feed network of four ports that form a unitary scattering matrix. The SPAR tag was implemented with a 90° hybrid feeding two patch antennas at 5.8 GHz. It was simulated in CST for radiation patterns and in ADS to compare to a static two-element array and a two individual antennas. The results show that the SPAR tag is able to have the benefits of a two-element array in terms of peak gain, but reduces the negative impact of reduced

beamwidth by having two separate beams. Of course, these benefits are at the expense of duplicate circuitry and physical area for the feed network.

After simulations to show the benefits of SPAR tags, the 90° hybrid with two patch antennas was fabricated and measured on a VNA to show isolation between the two feeding ports. The structure was then taken to an anechoic chamber to measure the retro-directivity of the device with SMA connectors on each feeding port. Each port was loaded with combinations of short, open and 50 Ohms to get each ports individual pattern. Finally, they are both opened or shorted to show the radiation pattern with dual main beams.

Next, the design was taken to measurement in an actual 5.8 GHz RFID system by designing a semi-active RFID tag and an energy harvester with the 2-by-2 90° hybrid structure which was compared to a single antenna tag. The SPAR tag showed similar performance to the simulations compared a to single antenna with two main lobes versus one that show the largest peak approximately twice as large as the peak of the single antenna for both energy harvested and reflected back to the reader. The implementation is also extrapolated to how to implement a SPAR tag as an N-by-N working passive tag.

Finally, the largest negative of using this technology in RFID tags is increasing physical space of the tag, which is addressed in the final chapter. A customized SPAR tag structure is investigated by using a Matlab-ADS co-simulation of planar feed structures. The optimizer is able to find a structure with the same area as the 90° hybrid with an identical stack up and similar performance.

6.2 Future Work

This research has shown that SPAR tags are useful in RFID systems, but it has also opened up many doors to future research that could not be covered in this dissertation.

6.2.1 N-by-N Canonical SPAR Tags

All implementations of the SPAR tag was of the 2-by-2 variety in this dissertation, but the structure can be implemented on an N-by-N basis. Unfortunately, the physical area required to create, not only the antenna array, but the feed structure grows very quickly. The large physical area makes it impractical to implement but would provide superior performance due to higher peak gain and beamwidth.

6.2.2 Reader Pattern Strobing

Reader pattern strobing is a technique that has been documented in literature in the past, but including that technique with SPAR tags can further improve range of passive and semi-active RFID tags. Pattern strobing requires multiple antennas on the reader side and phases them to search for the RFID tag much like a spotlight looking for an actor on a stage. By aiming the array to look for the tag, the reader has a higher gain than a single antenna and can accentuate SPAR benefits.

6.2.3 Custom FEA

The customized SPAR feed structures optimizer takes days to run to a decent result partly due using Agilent ADS to solve for the S-parameters. If a custom FEA solver is implemented, the solving time could be reduced allowing the optimizer to converge quicker.

6.2.4 Miniaturizing Other Microwave Structures

The search optimizer can also be used to apply to other microwave devices such as a circulator, directional coupler, etc. For example, in a situation with a limited area that cannot support a traditional canonical design, the optimizer can be run with ports in certain required locations.

6.2.5 Re-Configurable Antennas

In addition to using the search algorithm to find specific scattering matrices, the algorithm can also be applied to far field. ADS is capable of calculating the far field radiation pattern from the current distribution on the copper which could be used to design a re-configurable antenna. This is extremely interesting because it lumps the feed structure and antennas into a single design dramatically reducing the size of the physical area. When combining a re-configurable antenna with an RFID IC with multiple ports, it could hook up to a single structure with SPAR tag qualities minimizing the SPAR tag's physical area.

APPENDIX A

SCHEMATICS AND LAYOUT OF THE RFID TAGS

A.1 Energy Harvesting Experiments RFID Tags

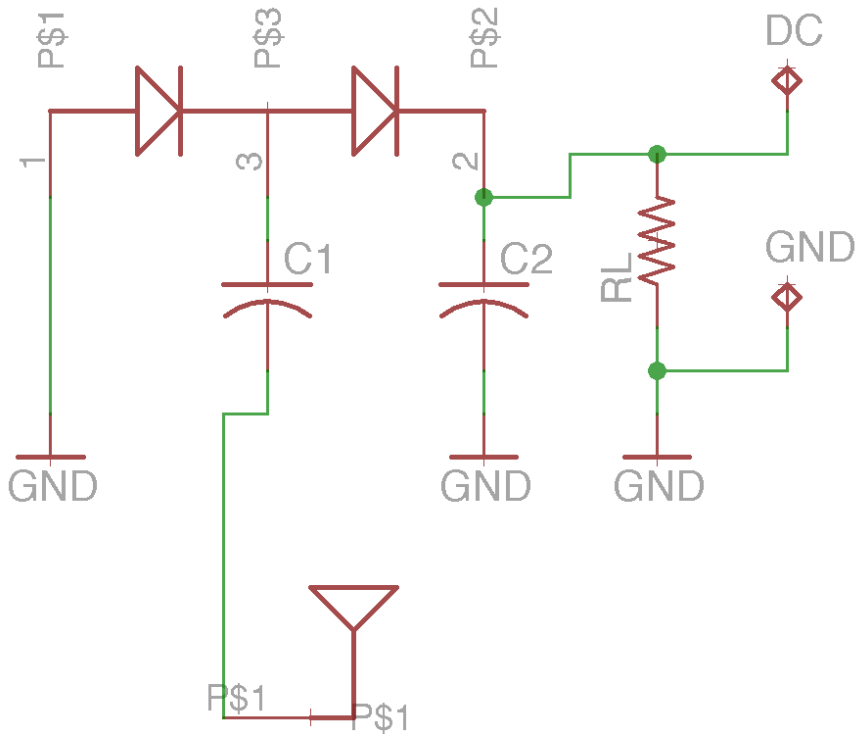

Figure 82: Schematic of Energy Harvesting Control RFID Tag

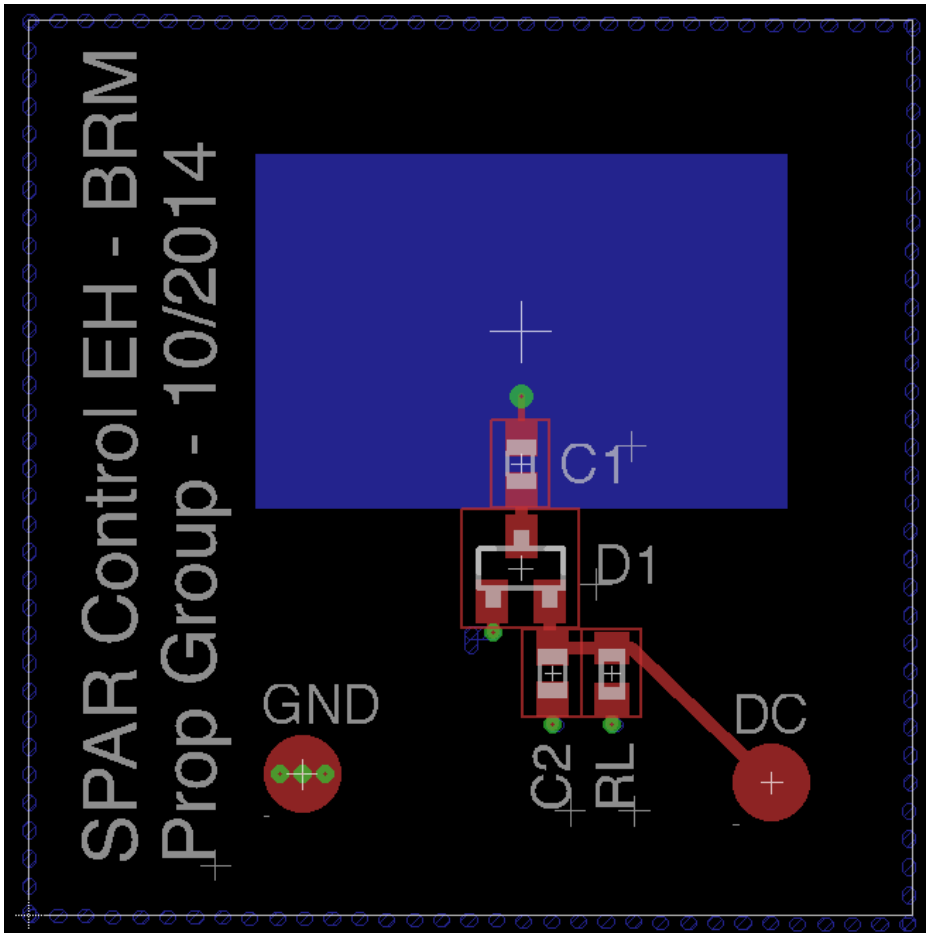

Figure 83: Layout of Energy Harvesting Control RFID Tag

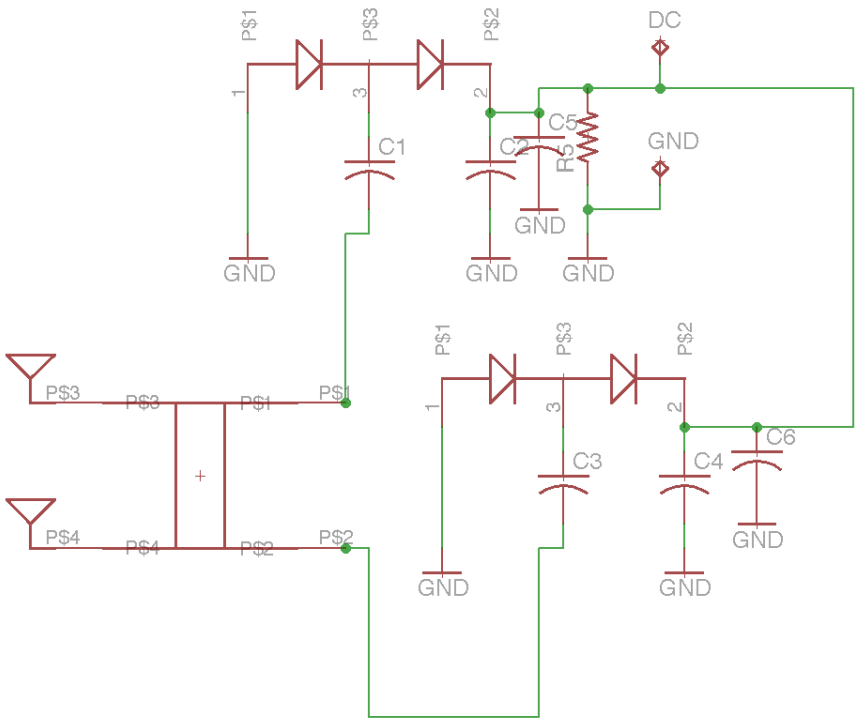

Figure 84: Schematic of Energy Harvesting SPAR RFID Tag

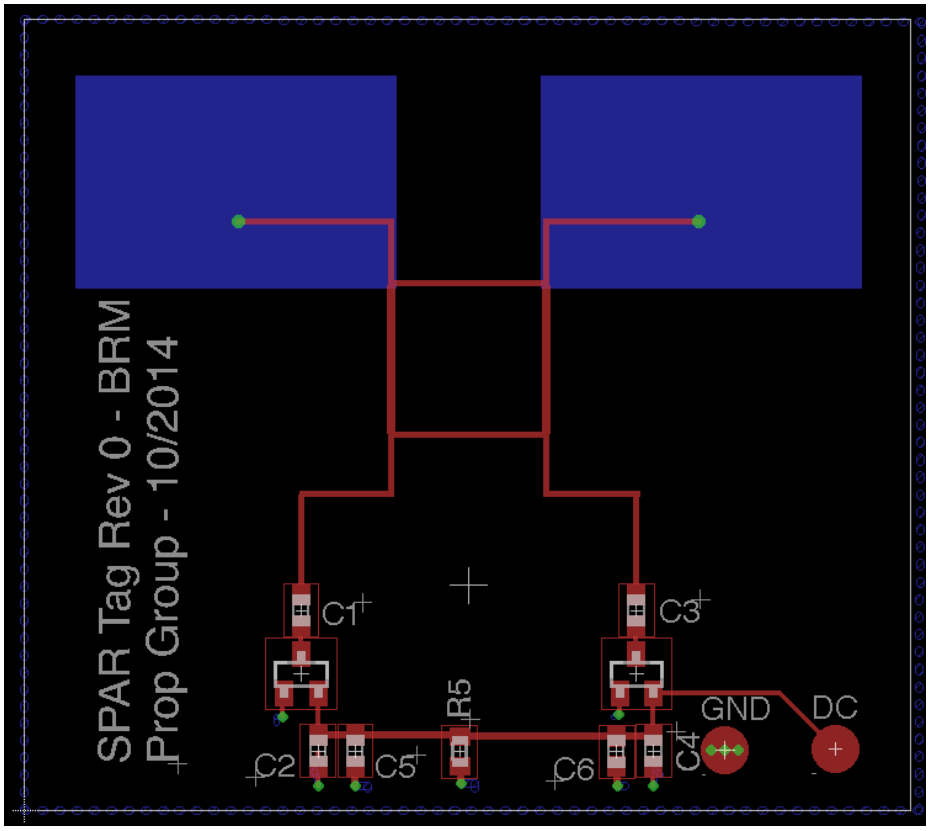

Figure 85: Layout of Energy Harvesting SPAR RFID Tag

A.2 Backscatter Experiments RFID Tags

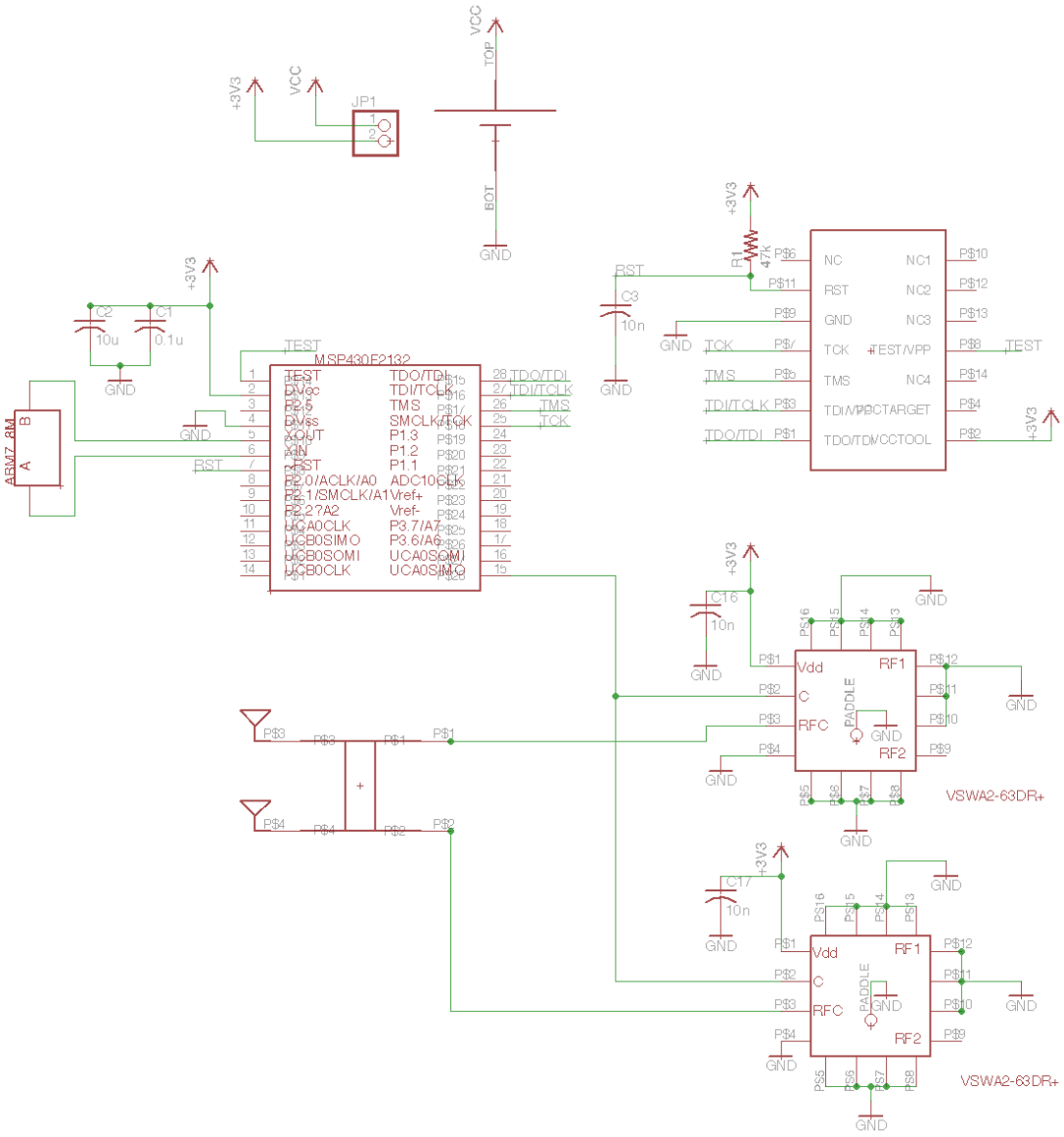

Figure 86: Schematic of Backscatter SPAR RFID Tag

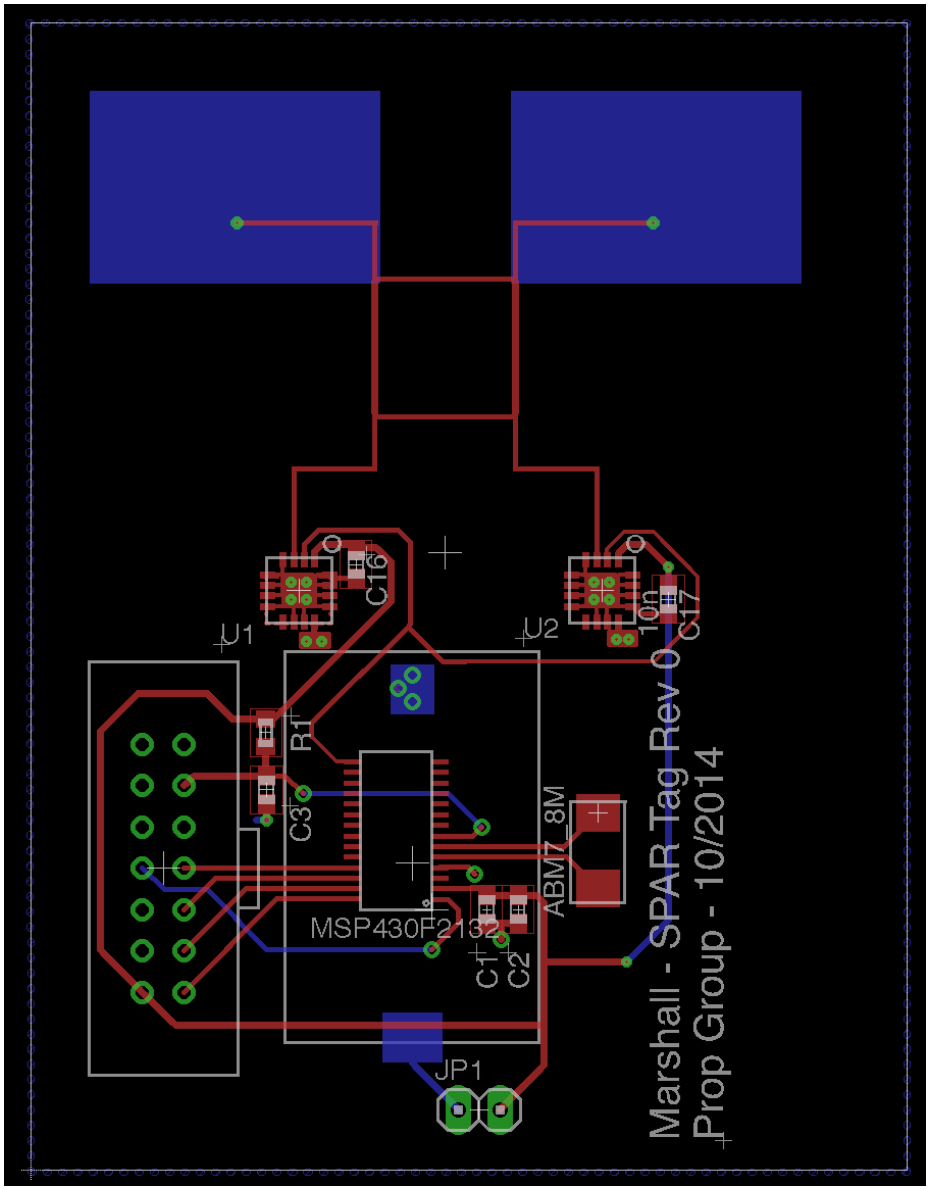

Figure 87: Layout of Backscatter SPAR RFID Tag

A.3 Original 90° *Hybrid Designs*

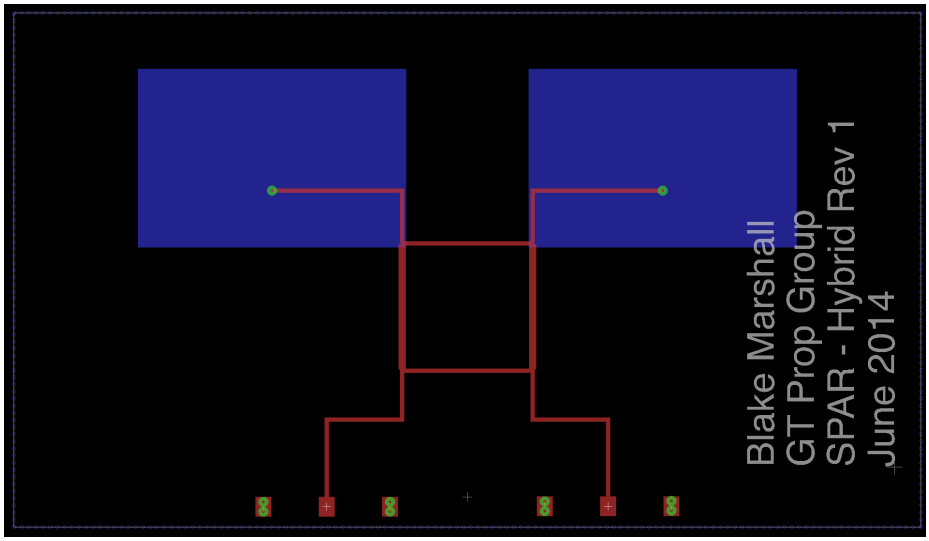

Figure 88: Layout of 90° Hybrid with Patch Antennas

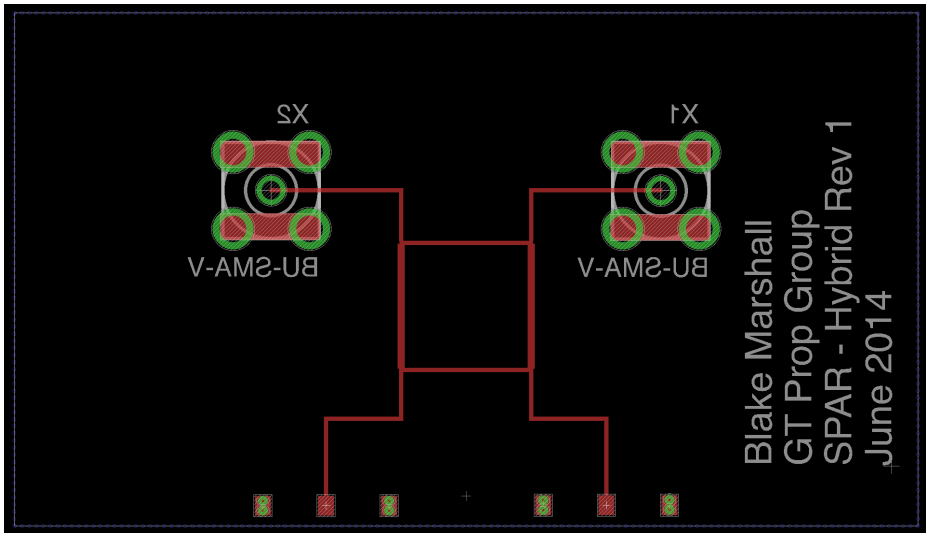

Figure 89: Layout of 90° Hybrid

APPENDIX B

EXAMPLE INPUT FILES TO AGILENT ADS MOMENTUM SIMULATOR

B.1 proj.prt

```
<?xml version="1.0" encoding="UTF-8"?>
<port_setup version="1.1">
  <calibration_group_list>
    <calibration_group id="1">
      <type>TML</type>
      <auto_split>true</auto_split>
    </calibration_group>
  </calibration_group_list>
  <port_list>
    <port id="1">
      <name>P1</name>
      <plus_pin>P1</plus_pin>
      <impedance>
        <real>50</real>
        <imag>0</imag>
      </impedance>
      <calibration_group_ref ref="1" />
    </port>
    <port id="2">
      <name>P2</name>
```

```
      <plus_pin>P2</plus_pin>
      <impedance>
        <real>50</real>
        <imag>0</imag>
      </impedance>
      <calibration_group_ref ref="1" />
    </port>
    <port id="3">
      <name>P3</name>
      <plus_pin>P3</plus_pin>
      <impedance>
        <real>50</real>
        <imag>0</imag>
      </impedance>
      <calibration_group_ref ref="1" />
    </port>
    <port id="4">
      <name>P4</name>
      <plus_pin>P4</plus_pin>
      <impedance>
        <real>50</real>
        <imag>0</imag>
      </impedance>
      <calibration_group_ref ref="1" />
    </port>
  </port_list>
</port_setup>
```

B.2 proj.pin

```
<?xml version="1.0" encoding="UTF-8"?>
<pin_list version="1.0">
  <!-- note: all coordinates are in meter -->
  <pin>
    <name>P1</name>
    <net>P1</net>
    <layout>
      <shape>
        <layer>1</layer>
        <purpose>-1</purpose>
        <point>
          <x>0</x>
          <y>0.0085315</y>
        </point>
      </shape>
    </layout>
  </pin>
  <pin>
    <name>P2</name>
    <net>P2</net>
    <layout>
      <shape>
        <layer>1</layer>
        <purpose>-1</purpose>
        <point>
          <x>0</x>
```

```
        <y>0.0028815</y>
      </point>
    </shape>
  </layout>
</pin>
<pin>
  <name>P3</name>
  <net>P3</net>
  <layout>
    <shape>
      <layer>1</layer>
      <purpose>-1</purpose>
      <point>
        <x>0.01695</x>
        <y>0.0085315</y>
      </point>
    </shape>
  </layout>
</pin>
<pin>
  <name>P4</name>
  <net>P4</net>
  <layout>
    <shape>
      <layer>1</layer>
      <purpose>-1</purpose>
      <point>
```

```
          <x>0.01695</x>
          <y>0.0028815</y>
        </point>
      </shape>
    </layout>
  </pin>
</pin_list>
```

B.3 proj.a

```
UNITS MM,10000;
EDIT proj;
ADD P1 :W0.000000 0,11.187 0.113,11.187 0.113,11.3 0,11.3;
ADD P1 :W0.000000 0.113,11.187 0.226,11.187 0.226,11.3 0.113,11.3;
ADD P1 :W0.000000 0.226,11.187 0.339,11.187 0.339,11.3 0.226,11.3;
ADD P1 :W0.000000 0.339,11.187 0.452,11.187 0.452,11.3 0.339,11.3;
ADD P1 :W0.000000 0.452,11.187 0.565,11.187 0.565,11.3 0.452,11.3;
ADD P1 :W0.000000 0.565,11.187 0.678,11.187 0.678,11.3 0.565,11.3;
ADD P1 :W0.000000 0.678,11.187 0.791,11.187 0.791,11.3 0.678,11.3;
ADD P1 :W0.000000 0.791,11.187 0.904,11.187 0.904,11.3 0.791,11.3;
ADD P1 :W0.000000 0.904,11.187 1.017,11.187 1.017,11.3 0.904,11.3;
ADD P1 :W0.000000 1.017,11.187 1.13,11.187 1.13,11.3 1.017,11.3;
ADD P1 :W0.000000 1.13,11.187 1.243,11.187 1.243,11.3 1.13,11.3;
ADD P1 :W0.000000 1.243,11.187 1.356,11.187 1.356,11.3 1.243,11.3;
ADD P1 :W0.000000 1.356,11.187 1.469,11.187 1.469,11.3 1.356,11.3;
ADD P1 :W0.000000 1.469,11.187 1.582,11.187 1.582,11.3 1.469,11.3;
ADD P1 :W0.000000 1.582,11.187 1.695,11.187 1.695,11.3 1.582,11.3;
ADD P1 :W0.000000 1.695,11.187 1.808,11.187 1.808,11.3 1.695,11.3;
```

```
ADD P1 :W0.000000 1.808,11.187 1.921,11.187 1.921,11.3 1.808,11.3;
ADD P1 :W0.000000 1.921,11.187 2.034,11.187 2.034,11.3 1.921,11.3;
ADD P1 :W0.000000 2.034,11.187 2.147,11.187 2.147,11.3 2.034,11.3;
ADD P1 :W0.000000 2.147,11.187 2.26,11.187 2.26,11.3 2.147,11.3;
ADD P1 :W0.000000 2.26,11.187 2.373,11.187 2.373,11.3 2.26,11.3;
ADD P1 :W0.000000 2.373,11.187 2.486,11.187 2.486,11.3 2.373,11.3;
ADD P1 :W0.000000 2.486,11.187 2.599,11.187 2.599,11.3 2.486,11.3;
ADD P1 :W0.000000 2.599,11.187 2.712,11.187 2.712,11.3 2.599,11.3;
ADD P1 :W0.000000 2.712,11.187 2.825,11.187 2.825,11.3 2.712,11.3;
ADD P1 :W0.000000 2.825,11.187 2.938,11.187 2.938,11.3 2.825,11.3;
ADD P1 :W0.000000 2.938,11.187 3.051,11.187 3.051,11.3 2.938,11.3;
ADD P1 :W0.000000 3.051,11.187 3.164,11.187 3.164,11.3 3.051,11.3;
ADD P1 :W0.000000 3.164,11.187 3.277,11.187 3.277,11.3 3.164,11.3;
ADD P1 :W0.000000 3.277,11.187 3.39,11.187 3.39,11.3 3.277,11.3;
ADD P1 :W0.000000 4.52,11.187 4.633,11.187 4.633,11.3 4.52,11.3;
ADD P1 :W0.000000 4.633,11.187 4.746,11.187 4.746,11.3 4.633,11.3;
ADD P1 :W0.000000 4.746,11.187 4.859,11.187 4.859,11.3 4.746,11.3;
ADD P1 :W0.000000 4.859,11.187 4.972,11.187 4.972,11.3 4.859,11.3;
ADD P1 :W0.000000 4.972,11.187 5.085,11.187 5.085,11.3 4.972,11.3;
ADD P1 :W0.000000 5.085,11.187 5.198,11.187 5.198,11.3 5.085,11.3;
ADD P1 :W0.000000 5.198,11.187 5.311,11.187 5.311,11.3 5.198,11.3;
ADD P1 :W0.000000 5.311,11.187 5.424,11.187 5.424,11.3 5.311,11.3;
ADD P1 :W0.000000 5.424,11.187 5.537,11.187 5.537,11.3 5.424,11.3;
ADD P1 :W0.000000 5.537,11.187 5.65,11.187 5.65,11.3 5.537,11.3;
ADD P1 :W0.000000 5.65,11.187 5.763,11.187 5.763,11.3 5.65,11.3;

This has been truncated to save the environment.
```

B.4 proj.ltd

```
TECHFORMAT=V2


UNITS
  DISTANCE=METRE
  CONDUCTIVITY=SIEMENS/M
  RESISTIVITY=OHM.CM
  RESISTANCE=OHM/SQ
  PERMITTIVITY=RELATIVETOVACUUM
  PERMEABILITY=RELATIVETOVACUUM
  FREQUENCY=HZ
END_UNITS


BEGIN_MATERIAL
  MATERIAL Cu CONDUCTIVITY=57000000  IMAG_CONDUCTIVITY=0
  MATERIAL FR4 PERMITTIVITY=3.66 LOSSTANGENT=0 PERMEABILITY=1 DJORDJEVIC
  LOWFREQ=1000 VALUEFREQ=5800000000 HIGHFREQ=1e+12
END_MATERIAL


BEGIN_OPERATION
  OPERATION OperationSHEET SHEET
  OPERATION OperationThickness_cond INTRUDE=3.347e-05 UP
  OPERATION OperationDRILL DRILL
END_OPERATION


BEGIN_MASK
  MASK 1 Name=cond PRECEDENCE=1 COLOR="ee6a50" MATERIAL=Cu
```

```
  OPERATION=OperationThickness_cond  MASK_PROPERTIES = { "MomModelType=operation2s
END_MASK

BEGIN_STACK
  TOP OPEN MATERIAL=AIR
  INTERFACE Name=__Interface2      MASK={cond}
  LAYER     Name=__SubstrateLayer1 HEIGHT=0.00017018 MATERIAL=FR4
  BOTTOM COVERED THICKNESS=1.735e-05 MATERIAL=Cu
END_STACK
```

B.5 proj.opt

```
simulationMode 1;
mesh_reduction ON;
no_cells_per_wavelength 20;
edgemesh_borderwidth 0 METRE;
mesh_convergence_plot OFF;
save_fields_for nofrequencies;
drcLogging ON;
drcLayer 255;
overlapextraction ON;
gppMergeAllShapes ON;
gppSimplifyAbsTol 0.01 LAMBDA;
gppSimplifyRelTol 0.082;
gppMinFeatureSize -0.5;
topoWireViasPadringRadius 3 VIARADII;
topoWireViasAntipadringRadius 5 VIARADII;
```

```
topoWireViasThermalRadius 5 VIARADII;
topoWireViasKeepViaOutline OFF;
topoWireViasKeepThroughPads OFF;
modelTypeStrip 3;
modelTypeVia 3;
SAVECURRENTSINFILE 1;
DS_DIR "dsFolder";
DS_NAME "dsName";
REUSEPREVIOUSRESULTS OFF;
INCLUDEPORTSOLVER ON;
matrixSolver 0;
```

B.6 proj.sti

```
START 5.6 STOP 6 STEP 0.2
;
```

B.7 proj.cfg

```
user     = .
site     = {$HOME}
supplied     = {$HPEESOF_DIR}
```

APPENDIX C

MATLAB OPTIMIZATION SCRIPTS

All Matlab code developed for this optimizer can be found here:

https://github.com/bmarshall651/Microwave_Structure_Search

C.1 adjustLensForPorts.m

```
function [ matrix ] = adjustLensForPorts( matrix, portMinors, portMetalOrAir )
%adjustLensForPort ensures that there is metal at each port location with
%non-metal on either side to prevent errors in MOM simulation with
%electrical connections to other ports
%
%Author: Blake R. Marshall - bmarshall651@gmail.com
%Date: July 6, 2014
%The Propagation Group at Georgia Institute of Technology
%
%@param matrix is the original matrix
%@param portLocations is the location of all the ports listed as: [x1 y1; x2
%y2; x3 y3;]
%@param portMetalOrAir template of the port metal or air via a 1-D spatial
%array with 1 for metal and 0 for air
%
%
%@return matrix is the same matrix passed in with cleaned up ports
```

```
metalMinorsTemp=portMinors.*portMetalOrAir;
metalMinors=metalMinorsTemp(metalMinorsTemp~=0);
airMinorsTemp=portMinors.*~portMetalOrAir;
airMinors=airMinorsTemp(airMinorsTemp~=0);



p=1;
for p=1:size(metalMinors,2)
    matrix(metalMinors(p))=1;
end

p=1;
for p=1:size(airMinors,2)
    matrix(airMinors(p))=0;
end

% p=1;
% while(p<=size(portLocations,1))
%     matrix(portLocations(p,1),portLocations(p,2))=1;
%
%     if portLocations(p,2)==1
%         matrix(portLocations(p,1)-1,portLocations(p,2))=0;
%         matrix(portLocations(p,1)+1,portLocations(p,2))=0;
%     elseif portLocations(p,1)==1
%         matrix(portLocations(p,1),portLocations(p,2)-1)=0;
```

```
%         matrix(portLocations(p,1),portLocations(p,2)+1)=0;
%     elseif portLocations(p,2)==size(matrix,2)
%         matrix(portLocations(p,1)-1,portLocations(p,2))=0;
%         matrix(portLocations(p,1)+1,portLocations(p,2))=0;
%     elseif portLocations(p,1)==size(matrix,1)
%         matrix(portLocations(p,1),portLocations(p,2)-1)=0;
%         matrix(portLocations(p,1),portLocations(p,2)+1)=0;
%     else
%         disp('Please only select port locations that are on an edge of the geome
%         break;
%
%     end
%
%
%
%     p=p+1;
%
% end
%
% end
```

C.2 buildLensFiles.m

```
function [ ] = buildLensFiles(
matrix, unitWidth, ports, startFreq, stopFreq, stepFreq, folderName, WorL)
%buildLensFiles creates required files for the simulation in Agilent ADS
```

```
% such as proj_a, .prt, .pin, .opt, .sti, and .cfg
%
%Author: Blake R. Marshall - bmarshall651@gmail.com
%Date: July 30, 2014
%The Propagation Group at Georgia Institute of Technology
%
%@param matrix is the binary matrix of the physical structure 1s are metal
%@param unitWidth is the physical width of each cell in the matrix in mm
%@param ports list of cell locations with ports [p1_row p1_col; p2_row
%p2_col;] would have 2 ports
%@param startFreq simulation start frequency
%@param stopFreq simulation stop frequency
%@param stepFreq simulation frequency steps
%@param folderName is the place where the files are stored
%@param WorL is DOS or UNIX... DOS is 1 and UNIX is 0
%
%


disp('Building all files required for simulation...')
if(WorL==1)%Windows - DOS
    slash='\';
elseif(WorL==0)%Mac/Linux - UNIX
    slash='/';
else
    disp('Choose either Windows or Linux');
    return;
end
```

```
generateGeom_Proj_aFile(matrix, unitWidth, [folderName, slash, 'proj_a']);
generatePorts_prtFile(ports,[folderName, slash, 'proj.prt']);
generatePorts_pinFile(matrix,ports,unitWidth,[folderName, slash, 'proj.pin']);
generateProperties_optFile('dsFolder','dsName', [folderName, slash, 'proj.opt'],Wo
generateSim_stiFile(startFreq,stopFreq,stepFreq, [folderName, slash, 'proj.sti']);
generateDirectory_cfgFile([folderName, slash, 'proj.cfg'],WorL);

disp('All files complete... Ready for Simulation!')
end
```

C.3 calculateSparamCost.m

```
function [ cost ] = calculateSparamCost(Sactual, Sideal, freq, weighting, useMagIn
%calculateSparamCost calculates the weighted error of distance between each
%S-parameter
%
%Author: Blake R. Marshall - bmarshall651@gmail.com
%Date: July 6, 2014
%The Propagation Group at Georgia Institute of Technology
%
%@param Sactual is the actual S-parameters
%@param Sideal is the ideal S-parameters to be obtained
%@param weighting is how heavily weighted each real and imaginary S
%parameter is weighted: [1 1; 1 1; 1 1; 1 1;] would be equal weighting on
%all S-parameters of a 2 port network
```

```
%
%@return costValue is the calculated cost


disp('Calculating the cost of the S-params')


[messa, a]=min(abs(freq-startCostFreq));
[messb, b]=min(abs(freq-stopCostFreq));
W=repmat(weighting,[1,1,b-a+1]);


%magDiff=abs(W.*abs(Sactual(:,:,a:b))-abs(Sideal(:,:,a:b)));
%finds the difference between S-parameters
%phaseDiff=abs(W.*angle(Sactual(:,:,a:b))-angle(Sideal(:,:,a:b)));


% magDiff=abs(W.*abs(Sactual(:,:,a:b))-abs(Sideal(:,:,a:b)));
%finds the difference between S-parameters
% phaseDiff=abs(W.*angle(Sactual(:,:,a:b))-angle(Sideal(:,:,a:b)));


% phaseDiff1=abs(angle(Sactual(1,3,a:b))-angle(Sactual(1,4,a:b))- ...
%     (angle(Sideal(1,3,a:b))-angle(Sideal(1,4,a:b))));
% phaseDiff2=abs(angle(Sactual(2,3,a:b))-angle(Sactual(2,4,a:b))- ...
%     (angle(Sideal(2,3,a:b))-angle(Sideal(2,4,a:b))));
% phaseDiff3=abs(angle(Sactual(1,3,a:b))-angle(Sactual(2,3,a:b))- ...
%     (angle(Sideal(1,3,a:b))-angle(Sideal(2,3,a:b))));
% phaseDiff4=abs(angle(Sactual(1,4,a:b))-angle(Sactual(2,4,a:b))- ...
%     (angle(Sideal(1,4,a:b))-angle(Sideal(2,4,a:b))));
% phaseDiff=phaseDiff1+phaseDiff2+phaseDiff3+phaseDiff4;
```

```
% if(useMagInCost==1 && usePhaseInCost==0)
%     avgNormCostValue=100*sum(sum(sum(magDiff)))/(b-a+1) ...
%         /(size(Sideal,2)^2);
%      avgNormMagCostValue=0;
%     avgNormPhaseCostValue=0;
% elseif(useMagInCost==0&&usePhaseInCost==1)
%     avgNormCostValue=100*sum(sum(sum(phaseDiff)))/(b-a+1) ...
%         /(size(Sideal,2)^2);
%     avgNormMagCostValue=0;
%     avgNormPhaseCostValue=0;
%elseif(useMagInCost==1&&usePhaseInCost==1)
    Scost=W.*(Sactual(:,:,a:b)-Sideal(:,:,a:b));
   magnitized=sqrt(Scost.*conj(Scost));
  cost=sum(sum(sum(magnitized(:,:,:))))/(b-a+1);


%     avgNormMagCostValue=1.2*sum(sum(sum(magDiff)))/(b-a+1) ...
%         /(size(Sideal,2)^2);
%    avgNormPhaseCostValue=1*sum(sum(sum(phaseDiff)))/(b-a+1) ...
%        /(size(Sideal,2)^2);
% %    avgNormPhaseCostValue=100*sum(phaseDiff)/(b-a+1) ...
% %         /pi;
%     avgNormCostValue=(avgNormMagCostValue+avgNormPhaseCostValue)/2;
% else
%     disp('Error - Must use either magnitude or phase for cost function');
%      avgNormMagCostValue=0;
%     avgNormPhaseCostValue=0;
% end
```

```
end
```

C.4 compareCosts.m

```
function [ porMatrix, Sparams, cost, genChange ] = compareCosts
( porMatrix,
Sparams, ...
    cost, myNextGuess, tempSparams, tempCost,  curHistInd, randRate, ...
    genChange, totalMinors)
%compareCosts decides whether or not to use the new matrix evaluated or
%keep the previous matrix
%
%Author: Blake R. Marshall - bmarshall651@gmail.com
%Date: Feburary 26, 2017
%The Propagation Group at Georgia Institute of Technology
%
%@param porMatrix
%@param Sparams
%@param cost
%@param myNextGuess
%@param tempSparams
%@param tempCost
%@param curHistInd
%@param randRate
%@param genChange
```

```
%@param totalMinors
%
%@return porMatrix is the calculated cost
%@return Sparams is the calculated cost
%@return cost is the calculated cost
%@return genChange is the calculated cost

if tempCost < cost(curHistInd-1) %|| rand()<randRate
    porMatrix(:,:,curHistInd)=myNextGuess;
    Sparams(:,:,:,curHistInd)=tempSparams;
    cost(curHistInd)=tempCost;
    genChange=1;
%Added to try to jumpstart local extrema
elseif 2*totalMinors<size(cost,2)
    if sum(abs(cost(size(cost,2))-cost(1,size(cost,2)-2*totalMinors: ...
            size(cost,2))))<0.001 && tempCost < max(cost)
        porMatrix(:,:,curHistInd)=myNextGuess;
        Sparams(:,:,:,curHistInd)=tempSparams;
        cost(curHistInd)=tempCost;
    else
        porMatrix(:,:,curHistInd)= porMatrix(:,:,curHistInd-1);
        Sparams(:,:,:,curHistInd)=Sparams(:,:,:,curHistInd-1);
        cost(curHistInd)=cost(curHistInd-1);
    end
else
    porMatrix(:,:,curHistInd)= porMatrix(:,:,curHistInd-1);
    Sparams(:,:,:,curHistInd)=Sparams(:,:,:,curHistInd-1);
```

```
    cost(curHistInd)=cost(curHistInd-1);
end

end
```

C.5 drawLens.m

```
function [ matr ] = drawLens( inputMatrix, unitWidth, portLocations, portWidth )
%drawLens converts the binary matrix to a bitmap of black for metal, white
%for non-metal, and red for ports (with metal)
%
%Author: Blake R. Marshall - bmarshall651@gmail.com
%Date: July 6, 2014
%The Propagation Group at Georgia Institute of Technology
%
%@param inputMatrix MxN binary matrix for metal and non metal
%@param unitWidth is the geometric length and width of each cell in
%@param portLocations is the location of all the ports listed as: [x1 y1; x2
%y2; x3 y3;]
%@param portWidth is the width of the ports in number of cells
%
%@return matr is the bitmap of the matrix

disp('Drawing the metal and air geom...')
```

```
matr=~repmat(inputMatrix,[1,1,3]);


temp1=1;
test(1,1,:)=[1 0 0];
while temp1 <= size(portLocations,1)
    matr(portLocations(temp1,1)-floor(portWidth/2):portLocations(temp1,1)
    +floor(portWidth/2),portLocations(temp1,2),:)=repmat(test,portWidth,1,1);
    temp1=temp1+1;
end


colorize=-0.5*(matr-ones(size(matr,1),size(matr,2),size(matr,3)));
matr=matr+colorize;


figure(1)
image([0 unitWidth*size(inputMatrix,2)], [0 unitWidth*size(inputMatrix,1)
    ], matr)
pbaspect([size(inputMatrix,2) size(inputMatrix,1) 1])
title(['Top Layer Geometry: Gray=metal, White=air,
 Pink=port, unitCell=',num2str(unitWidth),'mm']);
%grid on;
%grid on;
xlabel('x-dimension (mm)');
ylabel('y-dimension (mm)');
```

```
end
```

C.6 generateDirectorycfgFile.m

```
function [ ] = generateDirectory_cfgFile(outputProj_cfg, WorL)
%generateSubstrate_cfgFile creates cfg file for momentum simulation in
%Agilent ADS
%Author: Blake Marshall
%June 28, 2014

fOut = fopen(outputProj_cfg, 'wt');
if(WorL==1)%Windows - DOS
    slash='\';
elseif(WorL==0)%Mac/Linux - UNIX
    slash='/';
else
    disp('Choose either Windows or Linux');
    return;
end


fprintf(fOut, 'user     = . \n');
fprintf(fOut,'site     = {$HOME} \n');
fprintf(fOut,['supplied     = {$HPEESOF_DIR}',slash, ...
```

```
    'momentum', slash, 'lib \n']);

fclose(fOut);

disp('Directory .cfg File Complete')
end
```

C.7 generateFarFieldParamsvplFile.m

```
function [ outputVplFile ] = generateFarFieldParams_vplFile(
 frequency, portLocations, portExcitationNumber, PortImpedances, outputVplFile)
%generateFarFieldParams_vpl file for Agilent ADS Momentum simulation
%Agilent ADS
%Author: Blake Marshall
%June 28, 2014
%frequency: frequency for far field post-processing... must be within and
%calculated in s-parameter simulation
%portLocations: locations of all the ports
%portExcitationNumber: which port is being excited by 1V phase=0
%PortImpedances: complex value for the impedances of all the ports
%outputVplFile: output file for Agilent ADS to simulate FarField
fOut = fopen(outputVplFile, 'wt');

fprintf(fOut, 'CLIP -50; \n');
fprintf(fOut, '\n');
fprintf(fOut, 'COPOLARANGLE 0 DEG; \n');
fprintf(fOut, '\n');
```

```
fprintf(fOut, 'VISUALIZATIONTYPE 1; \n');
fprintf(fOut, '\n');
fprintf(fOut, 'PARAMETER FREQUENCY, \n');
fprintf(fOut, 'UNITS GHz, \n');
fprintf(fOut, ['PT ',num2str(frequency),'; \n']);
fprintf(fOut, '\n');
fprintf(fOut, 'PARAMETER PHI, \n');
fprintf(fOut, 'UNITS DEG, \n');
fprintf(fOut, 'PT 0; \n');
fprintf(fOut, '\n');
fprintf(fOut, 'VAR THETA, \n');
fprintf(fOut, 'UNITS DEG, \n');
fprintf(fOut, 'START -180 STOP 180; \n');
fprintf(fOut, '\n');

numOfPorts=size(portLocations,1);
x=1;

while(x<=numOfPorts)
    fprintf(fOut, ['PORT ', num2str(x),', \n']);
    fprintf(fOut, 'UNITS VOLT, \n');
    fprintf(fOut, 'UNITS DEG, \n');
    if(portExcitationNumber==x)
        fprintf(fOut, 'AMPLITUDE 1 PHASE 0, \n');
    else
        fprintf(fOut, 'AMPLITUDE 0 PHASE 0, \n');
    end
```

```
    fprintf(fOut, 'UNITS OHM, \n');
    fprintf(fOut, 'UNITS RAD, \n');
    fprintf(fOut, ['AMPLITUDE ',num2str(sqrt(real(PortImpedances)^2 ...
        +imag(PortImpedances)^2)),' PHASE ',
        num2str(atan(imag(PortImpedances)...
        /real(PortImpedances))),'; \n']);
    fprintf(fOut, '\n');
    x=x+1;
end



fclose(fOut);
end
```

C.8 generateGeomProjaFile.m

```
function [ outputProj_aFile ] = generateGeom_Proj_aFile(
matrix, unitWidth, outputProj_aFile)
%generateGeom_Proj_aFile creates proj_a file for Agilent
ADS Momentum simulation
%Agilent ADS
%Author: Blake Marshall
%June 28, 2014
%matrix: binary matrix of where copper is (1) and where it is not (0)
%unitWidth: width of each square of copper or non-copper
```

```
%outputProj_aFile: output file
fOut = fopen(outputProj_aFile, 'wt');

fprintf(fOut, 'UNITS MM,10000; \n');
fprintf(fOut, 'EDIT proj; \n');

[rows,cols]=size(matrix);
x=1;
y=1;
while(x<=rows)
    while(y<=cols)
        if(matrix(x,y)==1)
            fprintf(fOut, ['ADD P1 :W0.000000 ',
             num2str((y-1)*unitWidth) ...
            , ',' , num2str((rows-(x))*unitWidth) , ' ',
             num2str((y)*unitWidth) ...
            , ',' , num2str((rows-(x))*unitWidth) , ' ',
             num2str((y)*unitWidth) ...
            , ',' , num2str((rows-(x-1))*unitWidth) , ' ',
             num2str((y-1)*unitWidth) ...
            , ',' , num2str((rows-(x-1))*unitWidth) , ';' ,
            ' \n']);
        end
        y=y+1;
    end
    y=1;
    x=x+1;
```

```
end

fprintf(fOut, 'SAVE; \n');

fclose(fOut);

disp('Geometry proj_a File Complete')
end
```

C.9 generatePortspinFile.m

```
function [ output_args ] = generatePorts_pinFile(matrix, locs,
 unitWidth, outputProj_pinFile )
%generatePorts_pinFile creates the .pin file for Momentum simulation
%Agilent ADS
%Author: Blake Marshall
%June 28, 2014
%locs is Nx2 array of location of the ports in METERS
fOut = fopen(outputProj_pinFile, 'wt');

fprintf(fOut, '<?xml version="1.0" encoding="UTF-8"?>\n');
fprintf(fOut, '<pin_list version="1.0">\n');
fprintf(fOut, '  <!-- note: all coordinates are in meter -->\n');

[rows,cols]=size(locs);
x=1;
```

```
while(x<=rows)
   fprintf(fOut, '  <pin>\n');
   fprintf(fOut, ['    <name>P',num2str(x),'</name>\n']);
   fprintf(fOut, ['    <net>P',num2str(x),'</net>\n']);
   fprintf(fOut, '    <layout>\n');
   fprintf(fOut, '      <shape>\n');
   fprintf(fOut, '        <layer>1</layer>\n');
   fprintf(fOut, '        <purpose>-1</purpose>\n');
   fprintf(fOut, '        <point>\n');
   %Checks for which edge then fills in file with coordinate of port

   if locs(x,2)==1
          fprintf(fOut, ['          <x>',num2str(0),'</x>\n']);
          fprintf(fOut, ['          <y>',num2str((size(matrix,1)-
          locs(x,1)+0.5)*unitWidth/1000),'</y>\n']);
   elseif locs(x,1)==1
          fprintf(fOut, ['          <x>',num2str((locs(x,2)-0.5)
          *unitWidth/1000),'</x>\n']);
          fprintf(fOut, ['          <y>',num2str((size(matrix,1))
          *unitWidth/1000),'</y>\n']);
    elseif locs(x,2)==size(matrix,2)
          fprintf(fOut, ['          <x>',num2str((locs(x,2))
          *unitWidth/1000),'</x>\n']);
          fprintf(fOut, ['          <y>',num2str((size(matrix,1)-
          locs(x,1)+0.5)*unitWidth/1000),'</y>\n']);
   elseif locs(x,1)==size(matrix,1)
```

```
            fprintf(fOut, ['          <x>',num2str((locs(x,2)-0.5)*
            unitWidth/1000),'</x>\n']);
            fprintf(fOut, ['          <y>',num2str(0),'</y>\n']);
    else
        disp('Please only select port locations that are on an edge of the geometry
        break;

    end
    fprintf(fOut, '        </point>\n');
    fprintf(fOut, '      </shape>\n');
    fprintf(fOut, '    </layout>\n');
    fprintf(fOut, '  </pin>\n');
     x=x+1;
end

 fprintf(fOut, '</pin_list>\n');



fclose(fOut);

disp('Pin .pin File Complete')
end
```

C.10 generatePortsprtFile.m

```
function [ output_args ] = generatePorts_prtFile( locs ,
outputProj_prtFile)
%generatePorts_prtFile creates the .prt file for Momentum simulation
%Agilent ADS
%Author: Blake Marshall
%June 28, 2014
%locs is Nx2 array of location of the ports in METERS
fOut = fopen(outputProj_prtFile, 'wt');

fprintf(fOut, '<?xml version="1.0" encoding="UTF-8"?>\n');
fprintf(fOut, '<port_setup version="1.1">\n');
fprintf(fOut, '  <calibration_group_list>\n');
fprintf(fOut, '    <calibration_group id="1">\n');
fprintf(fOut, '      <type>TML</type>\n');
fprintf(fOut, '      <auto_split>true</auto_split>\n');
fprintf(fOut, '    </calibration_group>\n');
fprintf(fOut, '  </calibration_group_list>\n');
fprintf(fOut, '  <port_list>\n');

[rows,cols]=size(locs);
x=1;

while(x<=rows)
   fprintf(fOut, ['    <port id="',num2str(x),'">\n']);
   fprintf(fOut, ['      <name>P',num2str(x),'</name>\n']);
   fprintf(fOut, ['      <plus_pin>P',num2str(x),'</plus_pin>\n']);
```

```
   fprintf(fOut, '      <impedance>\n');
   fprintf(fOut, '        <real>50</real>\n');
   fprintf(fOut, '        <imag>0</imag>\n');
   fprintf(fOut, '      </impedance>\n');
   fprintf(fOut, ['      <calibration_group_ref ref="1" />\n']);
   fprintf(fOut, '    </port>\n');
    x=x+1;
end

 fprintf(fOut, '  </port_list>\n');
 fprintf(fOut, '</port_setup>\n');



fclose(fOut);

disp('Port .prt File Complete')
end
```

C.11 generatePropertiesoptFile.m

```
function [ output_args ] = generateProperties_optFile(
dsDir, dsName, outputProj_opt, WorL)
%generateSubstrate_optFile creates opt file for
momentum simulation in
%Agilent ADS
%Author: Blake Marshall
```

```
%June 28, 2014

fOut = fopen(outputProj_opt, 'wt');

if(WorL==1)%Windows - DOS
    slash='md';
elseif(WorL==0)%Mac/Linux - UNIX
    slash='mkdir';
else
    disp('Choose either Windows or Linux');
    return;
end

system([slash ,' ', dsDir]);
fprintf(fOut, ['DS_DIR ',dsDir,'; \n']);
fprintf(fOut,'NO_CELLS_PER_WAVELENGTH 20; \n');
fprintf(fOut,'EDGEMESH_BORDERWIDTH OFF; \n');
fprintf(fOut,'MESH_REDUCTION ON; \n');
fprintf(fOut,'OVERLAPEXTRACTION ON; \n');
fprintf(fOut,'MATRIXSOLVER 0; \n');
fprintf(fOut,'INCLUDEPORTSOLVER ON; \n');
fprintf(fOut,'MODELTYPESTRIP 3; \n');
fprintf(fOut,'MODELTYPEVIA 3; \n');
fprintf(fOut,'topoWireViasEnabled ON; \n');
fprintf(fOut,'topoWireViasKeepViaOutline OFF; \n');
fprintf(fOut,'topoWireViasKeepThroughPads OFF; \n');
```

```
fprintf(fOut,'topoWireViasKeepEndPads ON; \n');
fprintf(fOut,'topoWireViasPadringRadius 3 VIARADII; \n');
fprintf(fOut,'topoWireViasAntipadringRadius 5 VIARADII; \n');
fprintf(fOut,'topoWireViasThermalRadius 5 VIARADII; \n');
fprintf(fOut,'GPPMINFEATURESIZE -0.5; \n');
fprintf(fOut,'GPPMERGEALLSHAPES ON; \n');
fprintf(fOut,'GPPSIMPLIFYABSTOL 0.01 LAMBDA; \n');
fprintf(fOut,'GPPSIMPLIFYRELTOL 0.082; \n');
fprintf(fOut,'DRCLOGGING ON; \n');
fprintf(fOut,'DRCLAYER 255; \n');
fprintf(fOut,['DS_NAME ',dsName,'; \n']);
fprintf(fOut,'reusePreviousResults OFF; \n');
fprintf(fOut,'saveCurrentsInFile ON; \n');
fprintf(fOut,'SimulationMode 1;maxThreads 0; \n');
fprintf(fOut,'maxThreads 0; \n');

fclose(fOut);

disp('Simulation Settings .opt File Complete')
end
```

C.12 generateRandomMatrix.m

```
function [ randomMatrix ] = generateRandomMatrix(M,N, portMinors,
portMetalOrAir, percMetal, symAboutY, symAboutX)
%generateRandomMatrix creates a random binary MxN matrix and ensures that
```

```
%there is  1 at each port location.
%
%Author: Blake R. Marshall - bmarshall651@gmail.com
%Date: July 6, 2014
%The Propagation Group at Georgia Institute of Technology
%
%@param M is the number of rows
%@param N is the number of columns
%@param portLocations is the location of all the ports listed as: [x1 y1; x2
%y2; x3 y3;]
%
%@return randomMatrix is the resulting binary MxN matrix

%Creates random matrix of values then rounds them to 1 or 0

disp('Creating the metal and airs structure...');

if(symAboutY~=1 && symAboutX~=1)
    a=rand(M,N)<percMetal;
elseif (symAboutY~=1 && symAboutX==1)
    ta=rand(M/2,N)<percMetal;
    a(1:M/2,1:N)=ta;
    a(M/2+1:M,1:N)=flipud(ta);
elseif  (symAboutY==1 && symAboutX~=1)
    ta=rand(M,N/2)<percMetal;
    a(1:M,1:N/2)=ta;
    a(1:M,N/2+1:N)=fliplr(ta);
```

```
elseif (symAboutY==1 && symAboutX==1)
    ta=rand(M/2,N/2)<percMetal;
    a(1:M/2,1:N/2)=ta;
    a(M/2+1:M,1:N/2)=flipud(ta);
    a(1:M/2,N/2+1:N)=fliplr(ta);
    a(M/2+1:M,N/2+1:N)=rot90(ta,2);
else
    a=rand(M,N)<percMetal;
end

randomMatrix=adjustLensForPorts(a,portMinors,portMetalOrAir);

end
```

C.13 generateSimstiFile.m

```
function [ output_args ] = generateSim_stiFile( startFreqGiga,
stopFreqGiga, stepSize, outputProj_sti )
%generateSubstrate_stiFile creates sti file for momentum simulation in
%Agilent ADS
%Author: Blake Marshall
%June 28, 2014

fOut = fopen(outputProj_sti, 'wt');

%fprintf(fOut, ['START          ',num2str(startFreqGiga),' STOP         ', ...
```

```
%    num2str(stopFreqGiga),' STEP         ',num2str(numOfSteps),', \n']);
%fprintf(fOut,'AFS S_50 MAXSAMPLES 50 SAMPLING ALL NORMAL \n');
if(startFreqGiga==stopFreqGiga)
    fprintf(fOut,'PT        5.8, \n');
    fprintf(fOut,';');
elseif startFreqGiga < stopFreqGiga
    fprintf(fOut,['START ', num2str(startFreqGiga),' STOP ', ...
        num2str(stopFreqGiga), ' STEP ', num2str(stepSize), '\n']);
    fprintf(fOut,';');
else startFreqGiga > stopFreqGiga
    disp('Start and Stop Freq Inverted');
end

fclose(fOut);

disp('Simulation Freq .sti File Complete')
end
```

C.14 generateSubstrateltdFile.m

```
function [ fOut ] = generateSubstrate_ltdFile( er, tand,
 fmeasure, h, cond, outputProj_ltd)
%generateSubstrate_ltdFile creates ltd file for momentum simulation in
%Agilent ADS
%Author: Blake Marshall
%June 28, 2014
%er: relative permittviity of substrate
```

```
%tand: tangent delta of substrate
%fmeasure: frequency of er and tand
%h: height of substrate
%cond: conductivity of copper
%outputProj_ltd: file to write ltd to

disp('Building substrate and simulation parameters....');

fOut = fopen(outputProj_ltd, 'wt');

fprintf(fOut, 'TECHFORMAT=V2 \n');
fprintf(fOut, '\n');

fprintf(fOut, 'UNITS \n');
fprintf(fOut, '  DISTANCE=METRE \n');
fprintf(fOut, '  CONDUCTIVITY=SIEMENS/M \n');
fprintf(fOut, '  RESISTIVITY=OHM.CM \n');
fprintf(fOut, '  RESISTANCE=OHM/SQ \n');
fprintf(fOut, '  PERMITTIVITY=RELATIVETOVACUUM \n');
fprintf(fOut, '  PERMEABILITY=RELATIVETOVACUUM \n');
fprintf(fOut, '  FREQUENCY=HZ \n');
fprintf(fOut, 'END_UNITS \n');
fprintf(fOut, '\n');

fprintf(fOut, 'BEGIN_MATERIAL \n');
fprintf(fOut, ['  MATERIAL Cu CONDUCTIVITY=',num2str(cond),
'  IMAG_CONDUCTIVITY=0 \n']);
```

```
fprintf(fOut, ['  MATERIAL FR4 PERMITTIVITY=', num2str(er),
 ' LOSSTANGENT=',num2str(tand), ...
    ' PERMEABILITY=1 DJORDJEVIC LOWFREQ=1000 VALUEFREQ=',
    num2str(fmeasure),
     ' HIGHFREQ=1e+12 \n']);
fprintf(fOut, 'END_MATERIAL \n');
fprintf(fOut, '\n');

fprintf(fOut, 'BEGIN_OPERATION \n');
fprintf(fOut, '  OPERATION OperationSHEET SHEET \n');
fprintf(fOut, '  OPERATION OperationThickness_cond INTRUDE=3.347e-05 UP \n');
fprintf(fOut, '  OPERATION OperationDRILL DRILL \n');
fprintf(fOut, 'END_OPERATION \n');
fprintf(fOut, '\n');



fprintf(fOut, 'BEGIN_MASK \n');
fprintf(fOut, '  MASK 1 Name=cond PRECEDENCE=1 COLOR="ee6a50"
MATERIAL=Cu OPERATION=OperationThickness_cond  MASK_PROPERTIES =
{ "MomModelType=operation2sheet" } \n');
fprintf(fOut, 'END_MASK \n');
fprintf(fOut, '\n');

fprintf(fOut, 'BEGIN_STACK \n');
fprintf(fOut, '  TOP OPEN MATERIAL=AIR \n');
fprintf(fOut, '  INTERFACE Name=__Interface2      MASK={cond} \n');
fprintf(fOut, ['  LAYER     Name=__SubstrateLayer1 HEIGHT=',
```

```
num2str(h), ' MATERIAL=FR4 \n']);
fprintf(fOut, '  BOTTOM COVERED THICKNESS=1.735e-05 MATERIAL=Cu \n');
fprintf(fOut, 'END_STACK \n');



fclose(fOut);
end
```

C.15 getCoarseGridMinors.m

```
function [ myList, coarse] = getCoarseGridMinors( M, N, gridSize, XSym, YSym, ...
    randomize, genChange, autoCoarseList, x, totalCycles, prevCoarseness, ...
    homogenous)
%UNTITLED3 Summary of this function goes here
%   Detailed explanation goes here
if autoCoarseList == 0 && homogenous ==0
    coarse=gridSize(ceil(size(gridSize,2)*(x/totalCycles)));
    if mod(M,coarse)+mod(M,coarse)~=0
        myList=transpose(1:M*N);
        disp('!!!ERROR!!! -> The gridSize is not a multiple of
        the x-dim or the y-dim... we should probably fix this');
        %elseif gridSize==1
        %    myList=transpose(1:M*N);
    end
elseif autoCoarseList == 1 && genChange == 0 && prevCoarseness==0 ...
        && homogenous==0
    coarse=gcd(M,N);
```

```
    if coarse>=M || coarse>=N
        coarse=gcd(M/coarse,N/coarse);
    end
elseif autoCoarseList == 1 && genChange == 0 && prevCoarseness>1 ...
        && homogenous==0
    coarse=gcd(M/prevCoarseness, N/prevCoarseness);
elseif autoCoarseList == 1 && genChange == 1 && homogenous==0
    coarse=prevCoarseness;
else
    coarse=1;
end



if XSym ==1 && YSym==0
    xlim=N/2;
    ylim=M;
elseif XSym==0 && YSym==1
    xlim=N;
    ylim=M/2;
elseif XSym==1 && YSym==1
    xlim=N/2;
    ylim=M/2;
else
    xlim=N;
    ylim=M;
end
```

```
x=1;
y=1;
count=1;
while x < xlim && x+coarse-1<=xlim
    while y < ylim && y+coarse-1<=ylim
        temp=1;
        za=1;
        zb=1;
        % Adds all Minors used in square on each column
        while zb <= coarse
            while za <= coarse
                if zb==1 && za ==1
                    myList(count,temp)=x+(y-1)*N;
                else
                    myList(count,temp)=myList(count,1)+(za-1)+(zb-1)*N;
                end
                temp=temp+1;
                %Grab the minor
                curMinor=myList(count,1)+(za-1)+(zb-1)*N;
                %Find x and y values


                %yGuess=floor(curMinor/N)+1;
                yGuess=ceil(curMinor/N);
                xGuess=curMinor-((yGuess-1)*N);
                %Find symetry values
```

```
        if XSym ==1
            xSym=N-xGuess+1;
            myList(count,temp)=xSym+(yGuess-1)*N;
            temp=temp+1;
        end
        if YSym ==1

            %Debug
            ySym=M-yGuess+1;
            myList(count,temp)=xGuess+(ySym-1)*N;
            temp=temp+1;




        end
        if XSym==1 && YSym ==1
            myList(count,temp)=xSym+(ySym-1)*N;
            temp=temp+1;
        end


        za=za+1;
    end
    za=1;
    zb=zb+1;
end
%End of all minors used in square
y=y+coarse;
```

```
        count=count+1;
    end
    y=1;
    x=x+coarse;
end

if randomize ==1
    ok=1;
    while ok <=size(myList,1)
        randomizeIt=transpose(randperm(size(myList,1),size(myList,1)));
        myListTemp(ok,:)=myList(randomizeIt(ok),:);
        ok=ok+1;
    end

    myList=myListTemp;
    clear myListTemp
end
```

C.16 getPortMinors.m

```
function [portMinors, metalOrAirPort]= getPortMinors(portLocations, ...
    portWidth, xdimNumofCells, emptyBoundaries)

disp('Finding port minors for given ports...')
%emptyBoundaries=4;
metalOrAirPort=[];
```

```
for portN=1:size(portLocations,1);
    for portM=1:portWidth+emptyBoundaries;
        if mod(portWidth,2) == 0
            disp('Use odd number of cells for port width');
            portWidth=portWidth+1;
        else
            %(portWidth+emptyBoundaries)*(portN-1)+(portM-1)+1
            portMinors((portWidth+emptyBoundaries)*(portN-1)+(portM-1)+1)...
                = portLocations(portN,1)+...
                (portLocations(portN,2)-1)*xdimNumofCells +...
                portM-ceil((portWidth+emptyBoundaries)/2);

        end

    end
    metalOrAirPort=horzcat([metalOrAirPort, ...
        zeros(1,(emptyBoundaries)/2), ones(1, portWidth), ...
        zeros(1,emptyBoundaries/2)]);
    %     portMinorsRetro(3*(portN-1)+1:3*(portN))=[portLocations(portN,1)+...
    %(portLocations(portN,2)-1)*xdimNumofCells-1; ...
    %         portLocations(portN,1)+(portLocations(portN,2)-1)*xdimNumofCells; ..
    %         portLocations(portN,1)+(portLocations(portN,2)-1)*xdimNumofCells+1;]
end

end
```

C.17 interpretCTItoSparam.m

```
function [ S ] = interpretCTItoSparam( ctifile )
%UNTITLED11 Summary of this function goes here
%   Detailed explanation goes here

fOut=-1;
openAttempts=0;

while(fOut==-1)
    fOut = fopen(ctifile, 'r');
    openAttempts=openAttempts+1;
    if(openAttempts>3)
        disp('FAILED TO OPEN CTI FILE - DOES IT EXIST? Trying again...');
        S=-1;
        return;
    end
end

x=1;
count=1;
numOfSparams=1;
while(1)
    tline=fgetl(fOut);
    if(findstr('NBR_OF_PORTS',tline)==10)
        numOfPorts=str2double(tline(23));
```

```
        numOfSparams=numOfPorts*numOfPorts;
        break;
    end
end

ind=1;
while(1)
    tline=fgetl(fOut);
    if(findstr('VAR_LIST_BEGIN',tline)==1)
        while(1)
            tline2=fgetl(fOut);

            if(findstr('VAR_LIST_END',tline2)==1)
                break;
            end
            freqS(1,1,ind)=str2double(tline2);
            ind=ind+1;
        end
        break;
    end
end

sSpot=1;
while(sSpot <= numOfSparams)
    tline=fgetl(fOut);
    if(findstr('BEGIN',tline)==1)
        ind=1;
```

```
        while (ind<=size(freqS,3))
            tline2=fgetl(fOut);
            SStr=strsplit(tline2,',');
            S(mod(sSpot-1,numOfPorts)+1,ceil(sSpot/numOfPorts),ind)=
            str2double(SStr(1))+sqrt(-1)*str2double(SStr(2));
            ind=ind+1;
        end
        sSpot=sSpot+1;
    end
end
save('temp.mat');
fclose(fOut);

disp('S-parameter Data Extraction Complete')
end
```

C.18 runMOM.m

```
function [ ] = runMOM(folderPath)
%runMOM calls on Agilent ADS Momentum S-parameters from netlists in the
%folderPath directory
%
%Author: Blake R. Marshall - bmarshall651@gmail.com
%Date: July 6, 2014
%The Propagation Group at Georgia Institute of Technology
%
%@param folderPath directory to run in -- seems to only work in current
%directory (pwd)
```

```
st=tic;
system(['cd ' folderPath]);
% system(['MomEngine -T --objMode=MW proj proj']);
% system(['MomEngine -DB --objMode=MW proj proj']);
% system(['MomEngine -M --objMode=MW proj proj']);
%system(['MomEngine -O -3D --objMode=MW proj proj:']);
system(['MomEngine -O -3D --objMode=MW proj proj']);

tMin=toc(st)/60;
disp(['Simulation of Structure Time: ', num2str(tMin),' minutes'])
end
```

C.19 mainSequentialOptimization.m

```
%Main file for Sequential Optimizer to find 2-by-2 SPAR Tags
%Author: Blake Marshall
%February 2, 2017

clear all;
clc;
close all;

%%
%%Constants
ER=3.66; %relative permittviity
TAND=0;%0.0127; %tangent delta losses
FREQ=5.8E9; %frequency of er and tand measurements
```

```
H=0.00017018; %6.7 mil %height of substrate in meters
%H=0.0015748; %62 mil
COND=5.7E7; %conductivity of metal in S/m

YAXISSYM=1;
XAXISSYM=1;
USEMAGINCOST=1;
USEPHASEINCOST=1;
DOS=1;
j=sqrt(-1);

%%
%%Parameters
WorL=DOS;

%%
%Geometry Paramters

xdimNumofCells=100;
ydimNumofCells=150;
unitWidth=0.113; %in mm
%Hint: Make your unit width a 50Ohm trace width/n where n is an
odd integer

yAxisSym=YAXISSYM;
xAxisSym=XAXISSYM;
```

```
percMetal=1;


%%
%Ports Parameters
portLocations=[ceil(xdimNumofCells/4) 1; ...s
    ceil(3*xdimNumofCells/4) 1; ...
    ceil(xdimNumofCells/4) ydimNumofCells; ...
    ceil(3*xdimNumofCells/4) ydimNumofCells;]; %in matrix indicies
% portLocations=[ceil(xdimNumofCells/2) 1; ...
%     ceil(xdimNumofCells/2) ydimNumofCells;];
portWidth=3; %Make it odd
portEmptyBorderCells=2; %Make it even
%portWidth=1; %Make it odd
%portEmptyBorderCells=2; %Make it even


%%
%%Solver Parameters
%Solver
startFreq=5.6;
stopFreq=6.0;
stepFreq=0.2;


optimizer='sequential';
homogenous=0;
%coarseList=1;
coarseList=[10 10 10 10 10 5 5 5 2 1];
%coarseList=2;50
```

```
autoCoarseList=0; %coarseList starts at shorter side/8 then gets smaller
% it gets smaller if there are no changes from previous generation
randomizeMinors=1; %randomizes the minors in the list
mutRate=0;
etchingOnly=0;

%% Cost Parameters
%Cost
totalCycles=100;

startCostFreq=5.8;
stopCostFreq=5.8;

% Sideal=repmat([0 1*exp(j*160*pi/180); ...
%     1*exp(j*160*pi/180) 0;],...
%     [1 1 floor((stopFreq-startFreq)/stepFreq)+1]);

% weighting=[0 1; ...
%     0 0;];

useMagCost=USEMAGINCOST;
usePhaseCost=USEPHASEINCOST;

Sideal=repmat([0 0 -j/sqrt(2) -1/sqrt(2); ...
    0 0 -1/sqrt(2) -j/sqrt(2); ...
    -j/sqrt(2) -1/sqrt(2) 0 0; ...
    -1/sqrt(2) -j/sqrt(2) 0 0;],...
```

```
    [1 1 floor((stopFreq-startFreq)/stepFreq)+1]);
weighting=[1 1 1 1; ...
    1 1 1 1; ...
    0 0 0 0; ...
    0 0 0 0;];

%%
%%Set up final paramters
%Set up a few other paramters
freqRange=startFreq:stepFreq:stopFreq;

%Sets up slash for DOS or UNIX
if(WorL==1)
    slash='\';
    sys='DOS';
else
    slash='/';
    sys='UNIX';
end



%% Begin Optimizer

spewTitleStuff(sys, totalCycles, Sideal, weighting );

%Generate the substrate file .ltd
generateSubstrate_ltdFile(ER, TAND, FREQ, H, COND, ...
```

```
    [pwd, slash, 'proj.ltd']);

[portMinors, portMetalOrAir]=getPortMinors(portLocations, portWidth, ...
    xdimNumofCells, portEmptyBorderCells);
myBestGuess=generateRandomMatrix(xdimNumofCells,ydimNumofCells, ...
    portMinors, portMetalOrAir, percMetal, ...
    yAxisSym,xAxisSym); %100 metal
%Microstrip ONly
% myBestGuess=zeros(xdimNumofCells,ydimNumofCells);
% myBestGuess(ceil(xdimNumofCells/2)-1:ceil(xdimNumofCells/2)+1 ...
%     ,:)=ones(3,ydimNumofCells);

drawLens(myBestGuess,unitWidth,portLocations, ...
    portWidth); %Draws figure of what the lens looks like
buildLensFiles(myBestGuess,unitWidth,portLocations, startFreq, ...
    stopFreq, stepFreq, pwd, WorL); %builds netlist files for MOM

(pwd); %calls MOM to run netlist files
Sparams(:,:,:,1)=interpretCTItoSparam('proj.cti'); %interprets cti
to S-par

%Record Initial Data
porMatrix(:,:,1)=myBestGuess;
cost(1)=calculateSparamCost(Sparams, Sideal, freqRange, weighting, ...
    useMagCost, usePhaseCost, startCostFreq, stopCostFreq)

%%Begin the interations
```

```
x=1;
curHistInd=1;
indicies(curHistInd)=1;
coarseness=0;
genChange=1;
tic;

%load temp.mat;

while(x<=totalCycles)

    %Finds all minors for symmetry and coarser gene groups
    [myMinorList, coarseness] = getCoarseGridMinors(ydimNumofCells,xdimNumofCells,
        coarseList, xAxisSym, yAxisSym, randomizeMinors, genChange, ...
        autoCoarseList, x,totalCycles, coarseness, homogenous);

    %Starts the pass through
    minorCount=1;
    genChange=0;
    totalMinors=size(myMinorList,1);
    while(minorCount<=totalMinors)
        tStart=tic;
        curHistInd=curHistInd+1;
        if sum(ismember(myMinorList(minorCount,:), portMinors))==0
        %Check that a port is not included in minors
            myNextGuess=porMatrix(:,:,curHistInd-1);
            % if sum(sum(myNextGuess(myMinorList(minorCount,:))))>=1
```

```
    %Check if atleast one cell is metal
    myNextGuess(myMinorList(minorCount,:))
    =~myNextGuess(myMinorList(minorCount,:)); %Flip metal to non-metal
    drawLens(myNextGuess,unitWidth, portLocations, portWidth);
    buildLensFiles(myNextGuess,unitWidth,portLocations, startFreq, ...
        stopFreq, stepFreq, pwd, WorL); %builds netlist files for MOM
    runMOM(pwd); %calls MOM to run netlist files
    tempSparams=interpretCTItoSparam('proj.cti');
    %interprets file to Matlab
    while tempSparams == -1
        runMOM(pwd);
        tempSparams=interpretCTItoSparam('proj.cti');
        %interprets file to Matlab
        disp(['!!!!!!!!!!!!!Stuck on Minor:',
        num2str(minorCount), '!!!!!!!!!!'])
    end
    [tempCost]=calculateSparamCost(tempSparams, Sideal, freqRange,
    weighting, ...
        useMagCost, usePhaseCost, startCostFreq, stopCostFreq);
else
    tempCost=100000;
    myNextGuess=porMatrix(:,:,curHistInd-1);
    tempSparams=Sparams(:,:,:,curHistInd-1);
end

[porMatrix, Sparams, cost, genChange] = compareCosts(porMatrix, Sparams, .
    cost, myNextGuess, tempSparams, tempCost,  curHistInd, mutRate,
```

```
        genChange, totalMinors);

    elementSizeHistory(curHistInd)=coarseList(floor(size(coarseList,2)*
    ((x-1)/totalCycles))+1);
    timeHistory(curHistInd)=toc(tStart);
    indicies(curHistInd,1)=curHistInd; %curHistInd
    indicies(curHistInd,2)=x; %generation
    if curHistInd > 1
        newGenerationIndex(curHistInd)=(x-indicies(curHistInd-1,2));
        newGenerationIndex(curHistInd)=newGenerationIndex(curHistInd)
        .*cost(curHistInd);
    end

    if mod(curHistInd,100)==1
        save temp.mat;
    end

    figure(2)
    plot(indicies(:,1), cost, indicies(:,1), transpose(newGenerationIndex),
    'k.') ...
%           indicies, magCost, 'r', ...
%       indicies, phaseCost, 'g')
    title(['Generation ',num2str(x)]);
    %' Smag=', num2str(10*log10(abs(Sparams(1,:,2,curHistInd)))), ...
    %    ' Sphase=', num2str((180/pi)*(angle(Sparams(1,:,2,curHistInd))))]);
    %legend('cost','magCost','phaseCost');
```

```
        xlabel('Simulations')
        ylabel('Cost');
        legend('Cost', 'New Generation');


        figure(3)
        plot(elementSizeHistory)
        title('element size history')
        xlabel('Generation')
        ylabel('Element Flipped Size q-by-q');
        drawnow

%         figure(4)
%            title(['gen=',num2str(x), ' Smag=',
num2str(10*log10(abs(Sparams(1,:,2,curHistInd)))), ...
%             ' Sphase=', num2str((180/pi)*(angle(Sparams(1,:,2,
curHistInd))))]);

%         figure(6)
% M11=linspace(0,1,100);
% P11=linspace(0,pi,100);
% [M21,P21]=meshgrid(M11,P11);
%         s=surf(M21,P21,costPlot)
%         alpha(s,0.3)
%         hold on;
%         scatter3(abs(Sparams(1,2,2,:)), angle(Sparams(1,2,2,:)), cost(:), 'rx')
%         hold off;
```

```
%         xlabel('Magnitude S21');
%         ylabel('Phase S21');
%         title('Surface using Sdiff=S-Sideal sqrt(Sdiff*conj(Sdiff))');
%         drawnow

%         bestMag=abs(Sparams(:,:,:,curHistInd));
%         bestPhase=angle(Sparams(:,:,:,curHistInd));
        minorCount=minorCount+1;

        disp(['Generation: ', num2str(x)])
        disp(['Simulation: ', num2str(curHistInd)])
        disp(['Best Cost: ', num2str(cost(curHistInd))])
        disp('Best S-parameter Magnitude: ')
        20*log10(abs(Sparams(:,:,floor((stopFreq-startFreq)/stepFreq)+1,
        curHistInd)))
        disp('Best S-parameter Phase: ')
        (180/pi)*angle(Sparams(:,:,floor((stopFreq-startFreq)/stepFreq)+1,
        curHistInd))
    end



    x=x+1;
end
```

```
% figure(3)
% plot(freqRange,squeeze(abs(bestSparams(1,1,:))),freqRange,
squeeze(abs(Sparams(2,1,:))));
%buildLensFiles(lensMatrix1, unit, portLocations,5,7,0.1, pwd);
%generateFarFieldParams_vplFile(5.8, portLocations, 1, 50, [pwd, '\',
'proj.vpl']);

% figure(1)
% drawLens(lensMatrix1,unit, portLocations);
%runMOM(pwd);
%S=interpretSingleFreqCTI('proj.cti');
% generateFarFieldParams_vplFile(5.8, portLocations, 1, 50, [pwd, '\',
'proj.vpl']);
% runFarField(pwd);
% [ Efield_theta, Efield_phi, EthetaMax, EphiMax, THETA, PHI]=
% interpretFFFtoFarField('proj.fff','proj.ant');
% figure(2)
% plot3DPattern(sqrt(abs(Efield_phi).^2+abs(Efield_theta).^2),THETA,PHI)



%  figure(2)
%  plot(linspace(5,7,21),reshape(20*log10(abs(S(1,1,:))),1,21))
%  hold on;
%  plot(linspace(5,7,21),reshape(20*log10(abs(S(2,1,:))),1,21),'r-')
%  hold off;
%  legend('S11', 'S21');
%  xlabel('Frequency (GHz)');
```

```
%  ylabel('dB');
% title('S-parameters of Microstrip using Matlab-ADS Co-simulation');
% generateFarFieldParams_vplFile(5.8, portLocations, 2, 50, [pwd, '\',
'proj.vpl']);
% runFarField(pwd);
% [ Efield_theta2, Efield_phi2, EthetaMax2, EphiMax2, THETA2, PHI2]=
% interpretFFFtoFarField('proj.fff','proj.ant');
% figure(3)
% plot3DPattern(sqrt(abs(Efield_phi2).^2+abs(Efield_theta2).^2),THETA2,PHI2)
```

REFERENCES

[1] "Monza 5 tag chip datasheet ipj-w1600 - rev 1.1," *Impinj Inc.*, 2012.

[2] Ahn, M., Kim, D., and Kenney, J., "Throughput improvement in interference limited multipath environments using a smart antenna for ieee 802.11b wlan," pp. 411–414, Sept 2004.

[3] Alam, M., "Microstrip antenna array with four port butler matrix for switched beam base station application," in *Computers and Information Technology, 2009. ICCIT '09. 12th International Conference on*, pp. 531–536, Dec 2009.

[4] Allen, J., "A theoretical limitation on the formation of lossless multiple beams in linear arrays," *Antennas and Propagation, IRE Transactions on*, vol. 9, pp. 350–352, July 1961.

[5] Andersen, J. and Rasmussen, H., "Decoupling and descattering networks for antennas," *Antennas and Propagation, IEEE Transactions on*, vol. 24, pp. 841–846, Nov 1976.

[6] Balanis, C. A., *Antenna Theory*. John Wiley and Sons Inc., 1997.

[7] Boaventura, A. and Carvalho, N., "Maximizing dc power in energy harvesting circuits using multisine excitation," in *Microwave Symposium Digest (MTT), 2011 IEEE MTT-S International*, pp. 1–4, 2011.

[8] Bona, M., Manholm, L., Starski, J., and Svensson, B., "Low-loss compact butler matrix for a microstrip antenna," *Microwave Theory and Techniques, IEEE Transactions on*, vol. 50, no. 9, pp. 2069–2075, 2002.

[9] Bowden, L., "The story of iff (identification friend or foe)," *Physical Science, Measurement and Instrumentation, Management and Education - Reviews, IEE Proceedings A*, vol. 132, no. 6, pp. 435–437, 1985.

[10] Brown, W. C., "The history of power transmission by radio waves," *Microwave Theory and Techniques, IEEE Transactions on*, vol. 32, no. 9, pp. 1230–1242, 1984.

[11] Buchanan, N. and Fusco, V., "Bit error rate performance enhancement of a retrodirective array over a conventional fixed beam array in a dynamic multipath environment," *Microwave Theory and Techniques, IEEE Transactions on*, vol. 58, no. 4, pp. 757–763, 2010.

[12] Butler, J. and Howe, R., "Beamforming matrix simplifies design of electronically scanned antennas," *Elec. Design*, vol. 9, pp. 170–173, 1961.

[13] Cardullo, M., "Transponder apparatus and system," January 1973.

[14] Christie, S., Cahill, R., Buchanan, N., Fusco, V., Mitchell, N., Munro, Y., and Maxwell-Cox, G., "Rotman lens-based retrodirective array," *Antennas and Propagation, IEEE Transactions on*, vol. 60, no. 3, pp. 1343–1351, 2012.

[15] Chung, S. J. and Chang, K., "A retrodirective microstrip antenna array," *Antennas and Propagation, IEEE Transactions on*, vol. 46, no. 12, pp. 1802–1809, 1998.

[16] Dobkin, D. M., *The RF in RFID*. Newnes Elsevier, 2008.

[17] Durgin, G. D., Koo, G. A., and Lu, Y. A., "Wireless without batteries: Extraordinarily low-powered microwave communications," *Georgia Institute of Technology*, 2010.

[18] Fenn, A., Temme, D. H., Delaney, W. P., and Courtney, W., "The development of phased-array radar technology," *Lincoln Laboratory Journal*, vol. 12, no. 2, pp. 321–340, 2000.

[19] Fennani, B., Hamam, H., and Dahmane, A. O., "Rfid overview," in *Microelectronics (ICM), 2011 International Conference on*, pp. 1–5, 2011.

[20] Fusco, V. and Buchanan, N., "Developments in retrodirective array technology," *Microwaves, Antennas Propagation, IET*, vol. 7, no. 2, pp. 131–140, 2013.

[21] Fusco, V. and Toh, B. Y., "Retrodirective array augmentation for electronic rcs modification," *Microwave Theory and Techniques, IEEE Transactions on*, vol. 50, no. 7, pp. 1772–1778, 2002.

[22] Government, U. S., "Fcc 15.247 operation within bands 902-928 mhz, 2400-2483.5 mhz, and 5725-5850 mhz," *Federal Communications Commission*.

[23] Griffin, J. and Durgin, G., "Complete link budgets for backscatter-radio and rfid systems," *Antennas and Propagation Magazine, IEEE*, vol. 51, no. 2, pp. 11–25, 2009.

[24] Hall, P. and Vetterlein, S. J., "Review of radio frequency beamforming techniques for scanned and multiple beam antennas," *Microwaves, Antennas and Propagation, IEE Proceedings H*, vol. 137, no. 5, pp. 293–303, 1990.

[25] Hansen, R. C., *Phased Array Antennas*. John WIley and Sons Inc., 1998.

[26] Harrington, R. F., "Theory of loaded scatterers," *Electrical Engineers, Proceedings of the Institution of*, vol. 111, no. 4, pp. 617–623, 1964.

[27] Harris, D. B., "Radio transmission systems with modulatable passive responder," March 1960.

[28] Kahn, W. and Kurss, H., "The uniqueness of the lossless feed network for a multibeam array," *Antennas and Propagation, IRE Transactions on*, vol. 10, pp. 100–101, January 1962.

[29] Koelle, A. R., Depp, S. W., and Freyman, R., "Short-range radio-telemetry for electronic identification, using modulated rf backscatter," *Proceedings of the IEEE*, vol. 63, no. 8, pp. 1260–1261, 1975.

[30] Koo, G. A., "Signal constillations of retrodirective array phase modulator," *Georgia Institute of Technology Library Master's Thesis*, 2011.

[31] Landt, J., "The history of rfid," *Potentials, IEEE*, vol. 24, no. 4, pp. 8–11, 2005.

[32] Lay, D. C., *Linear Algebra and Its Applications*. Wiley.

[33] Lee, R.-H., Chang, C.-C., and Chang, S.-F., "A switched-beam fmcw radar for wireless indoor positioning system," pp. 65–68, Oct 2011.

[34] Lee, W., Kim, J., and Yoon, Y. J., "One dimensional phase conjugating/retrodirective mirror in millimeter-wave band," in *Antennas and Propagation Society International Symposium (APSURSI), 2010 IEEE*, pp. 1–4, 2010.

[35] Ma, T.-G., Wang, C.-W., Hua, R.-C., and Yang, C.-F., "Phased array antenna for uhf rfid applications using artificial transmission lines," in *Antenna Technology: Small Antennas and Novel Metamaterials, 2008. iWAT 2008. International Workshop on*, pp. 454–457, 2008.

[36] Mansoor, A., Grady, W., Thallam, R., Doyle, M., Krein, S. D., and Samotyj, M., "Effect of supply voltage harmonics on the input current of single-phase diode bridge rectifier loads," *Power Delivery, IEEE Transactions on*, vol. 10, pp. 1416–1422, Jul 1995.

[37] Marshall, B. R., Morys, M. M., and Durgin, G. D., "Parametric analysis and design guidelines of rf-to-dc dickson charge pumps for rfid energy harvesting," *RFID*, 2015.

[38] Marshall, B. and Durgin, G., "Staggered pattern charge collection: Antenna technique to improve rf energy harvesting," in *RFID (RFID), 2013 IEEE International Conference on*, pp. 30–35, 2013.

[39] Marshall, B. and Durgin, G., "Staggered pattern charge collector design and optimization," in *Radio and Wireless Symposium (RWS), 2013 IEEE*, pp. 67–69, 2013.

[40] Marshall, B., Valenta, C., and Durgin, G., "Dc power pattern analysis of n-by-n staggered pattern charge collector and n2 rectenna array," in *Wireless Power Transfer (WPT), 2013 IEEE*, pp. 115–118, 2013.

[41] McSpadden, J., Fan, L., and Chang, K., "A high conversion efficiency 5.8 ghz rectenna," in *Microwave Symposium Digest, 1997., IEEE MTT-S International*, vol. 2, pp. 547–550 vol.2, 1997.

[42] Mi, M., Mickle, M., Capelli, C., and Swift, H., "Rf energy harvesting with multiple antennas in the same space," *Antennas and Propagation Magazine, IEEE*, vol. 47, no. 5, pp. 100–106, 2005.

[43] Miyamoto, R. Y., Shiroma, W. A., Shiroma, G. S., Murakami, B. T., Ohta, A., and Tamamoto, M., "Microwave self-phasing antenna arrays for secure data transmission and satellite network cross links," Aug 2006.

[44] Miyamoto, R. and Itoh, T., "Retrodirective arrays for wireless communications," *Microwave Magazine, IEEE*, vol. 3, no. 1, pp. 71–79, 2002.

[45] OshPark, "Fr408 high performance laminate and prepreg," *Isola*, 2014.

[46] Park, Y.-H., Youn, D.-G., Kim, K.-H., and chul Rhee, Y., "A study on the analysis of rectenna efficiency for wireless power transmission," in *TENCON 99. Proceedings of the IEEE Region 10 Conference*, vol. 2, pp. 1423–1426 vol.2, Dec 1999.

[47] Pon, C., "Retrodirective array using the heterodyne technique," *Antennas and Propagation, IEEE Transactions on*, vol. 12, no. 2, pp. 176–180, 1964.

[48] Pozar, D. M., *Microwave Engineering*. Wiley.

[49] Pratt, T., Bostian, C. W., and Allnutt, J. E., *Satellite Communications*. John Wiley and Sons Inc., 2003.

[50] Rao, K. V. S., "An overview of backscattered radio frequency identification system (rfid)," *Microwave Conference, 1999 Asia Pacific*, vol. 3, pp. 746–749 vol.3, 1999.

[51] Richards, M. A., *Fundamentals of Radar Signal Processing*. McGraw-Hill Professional.

[52] Roberti, M., "History of rfid technology," *RFID Journal*, Jan 2005.

[53] Rogers, "Rt/duroid 5870 /5880 high frequency laminates," *Rogers Corporation*, pp. Publication 92–101, 2014.

[54] Rotman, W. and Turner, R., "Wide-angle microwave lens for line source applications," *Antennas and Propagation, IEEE Transactions on*, vol. 11, no. 6, pp. 623–632, 1963.

[55] Sakamoto, T., Ushijima, Y., Nishiyama, E., Aikawa, M., and Toyoda, I., "5.8-ghz series/parallel connected rectenna array using expandable differential rectenna units," *Antennas and Propagation, IEEE Transactions on*, vol. 61, no. 9, pp. 4872–4875, 2013.

[56] Sharp, E. and Diab, M., "Van atta reflector array," *Antennas and Propagation, IRE Transactions on*, vol. 8, no. 4, pp. 436–438, 1960.

[57] Shinohara, N., "Recent wireless power transmission via microwave and millimeter-wave in japan," in *Microwave Conference (EuMC), 2012 42nd European*, pp. 1347–1350, 2012.

[58] Stein, S., "On cross coupling in multiple-beam antennas," *Antennas and Propagation, IRE Transactions on*, vol. 10, pp. 548–557, September 1962.

[59] Stockman, H., "Communication by means of reflected power," *Proceedings of the IRE*, vol. 36, no. 10, pp. 1196–1204, 1948.

[60] Trotter, M. and Durgin, G., "Survey of range improvement of commercial rfid tags with power optimized waveforms," in *RFID, 2010 IEEE International Conference on*, pp. 195–202, 2010.

[61] Trotter, M., Valenta, C., Koo, G., Marshall, B., and Durgin, G., "Multi-antenna techniques for enabling passive rfid tags and sensors at microwave frequencies," in *RFID (RFID), 2012 IEEE International Conference on*, pp. 1–7, 2012.

[62] Tseng, W.-J., Chung, S.-J., and Chang, K., "A planar van atta array reflector with retrodirectivity in both e-plane and h-plane," *Antennas and Propagation, IEEE Transactions on*, vol. 48, no. 2, pp. 173–175, 2000.

[63] Valenta, C. and Durgin, G., "Rectenna performance under power-optimized waveform excitation," in *RFID (RFID), 2013 IEEE International Conference on*, pp. 237–244, 2013.

[64] Van Atta, L. C., "Electromagnetic reflector," Oct 1959.

[65] Vogelman, J. H., "Passive data transmission technique utilizing radar echoes," July 1968.

[66] Walton, C., "Electronic identification and recognition system," August 1973.

[67] Wang, C.-W., Ma, T.-G., and Yang, C.-F., "A new planar artificial transmission line and its applications to a miniaturized butler matrix," *Microwave Theory and Techniques, IEEE Transactions on*, vol. 55, no. 12, pp. 2792–2801, 2007.

[68] Zamora, A., Iwami, R., Chun, T., and Shiroma, W., "An overview of recent advances in retrodirective antenna arrays," in *Wireless Information Technology and Systems (ICWITS), 2010 IEEE International Conference on*, pp. 1–4, 2010.

[69] Zhang, Y., Christie, S., Fusco, V., Cahill, R., and Zhang, J., "Retrodirective rotman lens constraining factors," in *Antennas and Propagation (EUCAP), 2012 6th European Conference on*, pp. 2981–2984, 2012.

[70] Zhang, Y., Ding, Y., and Fusco, V., "Sidelobe modulation scrambling transmitter using fourier rotman lens," *Antennas and Propagation, IEEE Transactions on*, vol. 61, no. 7, pp. 3900–3904, 2013.

[71] Zidek, P. D., Sellers Jr, J. W., Thiele, G. A., Mayle Jr, E. E., and Riechers, R. G., "Radio frequency tag system," Aug 2000.

[72] Zou, J.-Y., Wu, C.-H., and Ma, T.-G., "Heterogeneous integrated beam-switching/ retrodirective array using synthesized transmission lines," *Microwave Theory and Techniques, IEEE Transactions on*, vol. 61, no. 8, pp. 3128–3139, 2013.